Stony Brook University

Emission-Excitation Fluorescent Optoelectronic Sensors

A Dissertation Presented

by

Anatoliy Borodin

to

The Graduate School

in Partial Fulfillment of the

Requirements

for the Degree of

Doctor of Philosophy

in

Electrical Engineering

Stony Brook University

May 2015

Stony Brook University

The Graduate School

Anatoliy Borodin

We, the dissertation committee for the above candidate for the

Doctor of Philosophy degree, hereby recommend

acceptance of this dissertation.

Dr. Michael Gouzman – Dissertation Advisor
Adjunct Professor, Electrical and Computer Engineering

Dr. Milutin Stanaćević - Chairperson of Defense
Associate Professor, Electrical and Computer Engineering

Dr. Leon Shterengas
Associate Professor, Electrical and Computer Engineering

Dr. David Westerfeld
Assistant Professor, Electrical and Computer Engineering

Dr. Michael Tkachuk
Chief Technical Specialist, BAH Holdings, LLC

This dissertation is accepted by the Graduate School

Charles Taber
Dean of the Graduate School

Abstract of the Dissertation

Emission-Excitation Fluorescent Optoelectronic Sensors

by

Anatoliy Borodin

Doctor of Philosophy

in

Electrical Engineering (ESE)

Stony Brook University

2015

Notwithstanding the existing superior qualities of fluorescence sensors and sensor systems, the field of fluorescence sensing technology is open for active exploration and inspires researchers to develop, using more sophisticated detection methods, faster, more compact, less expensive designs that would appeal to a wider circle of customers.

In this dissertation, I report on the development of two excitation-emission fluorescent optoelectronic sensors. First, I present a functional prototype of a low-cost portable non-fiber optic oxygen sensor, based on fluorescence quenching. The prototype design benefits from the robustness of a non-fiber optic design configuration and the simplicity of a double-sided optical configuration. I detected experimentally and studied analytically the advantages of a sandwich-structured sensor element over a sensor element consisting of a single oxygen-sensitive film. Based on the study, I concluded that the dynamic range provided by a sandwich-structured sensor element exceeds that of a single-film sensor element, on condition that the thickness of all sensing films in both sensor elements is equal. As for the sensitivity of a sandwich-structured sensor element, it exceeds that of a single-film sensing element if the sensing films of the former are thinner. To minimize the number of employed electronic components and avoid using sophisticated and expensive instruments, while designing our prototype, I employed an intensity-based measuring technique. I suggested a Stern-Volmer equation modification so that the user could avoid calibrating the designed prototype, to determine oxygen concentration at different temperatures. My analytical model led to the development of a novel optical design configuration for sensors, based on fluorescence quenching, and also demonstrated the configuration superiority in sensitivity over its analogs.

My second design presented in this dissertation is a functional prototype of a novel fluorimeter, where a set of individually controlled laser diodes (LDs) is used as excitation light sources. The fluorimeter's performance is evaluated by authenticating protected objects. To authenticate objects marked with fluorescent materials, I proposed a method, based on the analysis of excitation-emission matrices (EEMs) representing security markers, which helps

avoid authentication errors, improves the speed of information processing due to the introduced digitized EEMs, basis EEMs, and basis markers. I also presented a conceptual design of a multidimensional fluorimeter, based on the designed prototype. Due to the capability of the new fluorimeter to control LDs individually, it can be used to scan not only excitation and emission wavelengths, but also the optical power density and modulation frequency of excitation light. The suggested conceptual design enables the acquisition of 3D spectra, which provide more detailed information about molecules in a single measurement, due to the employment of an excitation light modulation technique and a multi-channel photomultiplier tube. The multidimensional fluorimeter opens up new opportunities for investigating unique fluorescence properties of UC materials by analyzing multidimensional fluorescence spectra.

Dedication Page

To my family

Table of Contents

List of Figures

List of Tables

List of Abbreviations

2D two-dimensional
3D three-dimensional
ADC analog to digital converter
CCD charge-coupled device
EEM excitation-emission matrix
FWHM full width at half maximum
IC internal conversion
ID identifier
IR infrared
ISC intersystem crossing
LED light emitting diode
LD laser diode
NIR near infrared
OS optical sensor
OOS oxygen optical sensor
PMT photomultiplier tube
RH relative humidity
SE sensor element
SM security marker
SNR signal to noise ratio
TC transmission coefficient
VIS visible spectrum
UC upconverting
UCF upconversion fluorescence

Publications

1. A. Borodin, M. Gouzman, V. Kuzminskiy, “Development of a multidimensional fluorimeter and its application for authenticating objects marked with upconverting security markers,” Applied Optics, Submitted 01/30/2015, Under Preproduction Review

2. A. Borodin, M. Gouzman, “Hyper-Fluorimeter”, U.S. Patent Application, Serial No.: 62/082,814, 11/21/2014

3. A. Borodin, W. Cheng, D. Gavrilov, M. Gouzman, V. Smagin, “Optical Control Sensor System” US 20130161483 A1, un. 27, 2013

4. V. Dhulla, G. Gudkov, D. Gavrilov, A. Stepukhovich, A. Tsupryk, O. Kosobokova, A. Borodin, B. Gorbovitski and V. Gorfinkel, “Single Photon Counting Module Based on Large-area APD and Novel Logic Circuit for Quench and Reset Pulse Generation,” IEEE J. Select. Topics Quantum. Electron., Vol. 13, no. 4, pp. 926-933, , July/August 2007

5. G. Gudkov, V. Dhulla, A. Borodin, D. Gavrilov, A. Stepukhovich, A. Tsupryk, B. Gorbovitski, V. Gorfinkel,"32-channel single-photon counting module for ultra-sensitive detection of DNA sequences", conference on Advanced Photon Counting Techniques, Proc. of SPIE vol.6372, 63720C, Boston, Massachusetts, USA Oct 1-4, 2006

Chapter 1

Introduction

Nowadays, nearly every physical phenomenon that determines interactions between photons, molecules and particles has been employed in sensors or sensor systems. In recent years, modern electronics and optics have provided sensors and sensor systems with the most efficient input and output interfaces capable of satisfying the needs of a wide group of customers. One of the most favored phenomena taken as a basis for the development of sensing technology is fluorescence. Designers and researchers are in enthusiastic pursuit of fluorescent sensors, whose sensitivity is projected to the limit of a single molecule [1][1], and which are based on ultra-high sensitive fluorescence techniques. Fluorescence-based sensors excel other sensors in the speed of response, which can be as short as a fluorescence lifetime [2]. These sensors offer a very high spatial resolution which in common microscopy is limited to about 500 nm [3]; they are non-distractive and non-invasive – the sensor element can be located at a certain distance and connected to the sensor element via propagation light; they are immune to radio frequency and electromagnetic interference; and they are versatile – fluorescence-based sensors can operate in solid, liquid, and gaseous media [4-10].

Since even the simplest measuring of fluorescence involves a simultaneous measuring of several parameters, e.g. light intensity and excitation and emmission wavelengths, it requires a multiparameter technique. A set of numerous parameters obtained while measuring fluorescence is a fluorescence spectrum. Because spectra are acquired and measured data are processed, as a rule, in the matrix format, in the literature, the measured parameters are referred to as "dimensions." To obtain a conventional single emission or a single excitation spectrum, two dimensions – fluorescence intensity and excitation (for an excitation spectrum) or emission (for an emission spectrum) wavelengths – are processed in the 2D matrix format, which is why this spectrum is called a "2D spectrum." For an excitation-emission spectrum, three dimensions – both excitation and emission wavelengths and fluorescence intensity – are required to be processed in the 3D excitation-emission matrix (EEM) format, in which case we are dealing with a "3D spectrum." A conventional 2D single-emission or single-excitation spectrum is often insufficient for performing a thorough analysis of complex multicomponent samples, mixtures, and microenvironments of fluorescent molecules. More detailed information can be obtained by scanning both excitation and emission wavelengths and generating an EEM, i.e. obtaining a 3D spectrum [11-16]. Yet, the information provided even by a 3D spectrum can be insufficient to study properties of recently synthesized nanoparticles, e.g. nanoparticles changing their spectra depending on the excitation light power density [17] or modulation frequency [18]. To perform this task, researchers require up-to-date dedicated multidimensional fluorimeters capable of scanning additional dimensions, e.g. excitation light power density and modulation frequency.

Major limitations of most commercial fluorimeters include their slow-speed mechanical wavelength selectors, as well as their high cost. It should be noted that spectrum acquisition is a time-consuming process due to the necessity to perform mechanical scanning across the excitation and emission wavelength ranges. The insufficient scanning speed is unacceptable if the spectral wavelength range needs to be increased and the wavelength increment needs to be decreased. The high cost is another drawback of commercial fluorimeters that makes them unaffordable for many laboratories [19]. Notwithstanding the existing superior qualities of

[1] The endnotes are to be found on pp. 102-110.

certain fluorimeters and other optoelectronic sensors, the field of fluorescence sensing technology is open for active exploration and inspires researchers, using more sophisticated detection methods, to develop faster, more compact, less expensive designs that would appeal to a wider circle of customers. However, it is difficult to find a successful decision by merely compromising between the cost, accuracy, speed, flexibility, and size of a new sensor. Because of the growing competition, only novel, unique, or special designs can be successful on the market. Supported by industrial grants, the Optoelectronic Sensor Laboratory at Stony Brook University has conducted a number of projects developing emission-excitation fluorescent optoelectronic sensors. My dissertation presents the results obtained during research and experiments while working on the development of an optical oxygen sensor and a fluorimeter designed for detecting upconversion fluorescent materials.

1.1 Dissertation Contributions

The contributions of this dissertation to the field of excitation emission optoelectronic fluorescence sensors are multi-aspect. In the frame of this work, we have proposed:

- a prototype of a simple, robust and low-cost OOS based on fluorescence quenching;
- a novel optical design configuration for fluorescence sensors;
- an analytical model of the OOS;
- a prototype of a novel fluorimeter;
- a conceptual design of a multidimensional fluorimeter based on the designed prototype;
- a method, based on EEM analysis, for authenticating objects marked with fluorescent markers.

1.2 Dissertation Outline

This dissertation consists of five chapters. My original experiments are described in Chapters 3 and 4.

Chapter 2 contains a disambiguation of terms pertaining to sensors, used by authors working in different fields. To avoid confusion, I discuss terms and basic notions employed in this dissertation.

In Chapter 3, I give a broad overview of related work on optical oxygen sensors. Topic-specific literature reviews are provided in the relevant chapters throughout this dissertation. I also present the results of my work on the Project "Development of the portable low-cost oxygen sensor based on fluorescence quenching." Within its framework, I developed an Analytical Model of an optical oxygen sensor and designed a functional prototype of an optical oxygen sensor, based on fluorescence quenching, and a novel optical design configuration for sensors, based on fluorescence quenching. Work on an article and a patent is in progress.

In Chapter 4, I describe the results of my work on the Project "Feasibility of an object's authentication using upconverting (UC) security markers." Within its framework, I participated in the design of and tested the prototype of a novel fluorimeter. I proposed an EEM-based

method for authenticating objects marked with fluorescent markers, by introducing basis EEMs and basis markers. An article and a patent are under review.

Chapter 5 concludes the dissertation by summarizing the contributions of this dissertation, suggesting possible further directions of research, and outlining future work.

Chapter 2

Terminology and Background

2.1. Interaction of Light with Matter

The study of the interaction between light and matter can take many forms [1][2], and is referred to as *spectroscopy*, dealing with measurements of excitation and emission light intensity as a function of light wavelengths. If light traveling in one medium strikes the surface of another medium, the photons of the light can "bounce" off of the boundary surface. They can also be forced to deflect from a straight trajectory by the localized in the matter non-uniformities (scattering centers), or they can undergo *absorption* by the matter through which they are passing, i.e. they can lose their energy. The phenomenon responsible for photon deflection is known as *reflection* or *scattering*. The absorption of photons during light propagation through matter leads to the transformation of the energy of photons, raising electrons in atoms to a higher *energy level*, or raising molecules to higher *rotational or vibrational energy levels* called *excited states*. Both scattering and reflection include the process of absorption. The absorbed energy can be converted into heat or radiated back into a medium. Some phenomena caused by the interaction of light and matter are shown in Fig. 2.1.

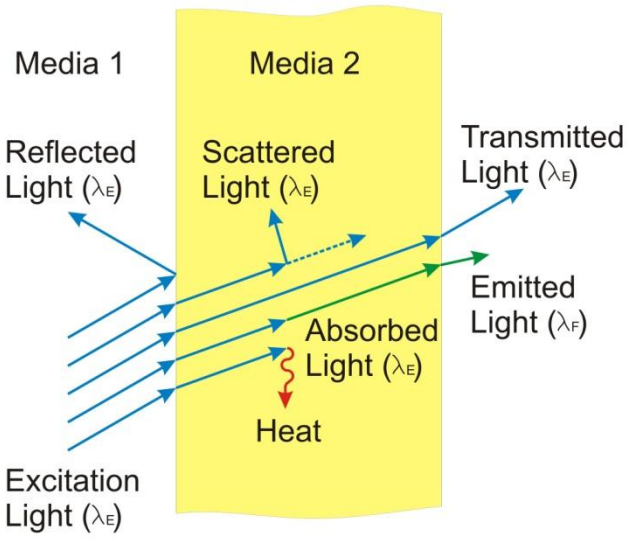

Figure 2.1. Phenomena caused by the interaction of light and matter.

In order to understand the interaction between light and matter, let us consider how a photon interacts with a single atom. Atom properties can be determined by its *electron configuration* or by the distribution of electrons in *atomic orbitals* which may also be referred to as physical regions where electrons have the highest probability of being found. Each atomic orbital is characterized by a unique set of *quantum numbers n*, *l*, and *m*, which represent the electron's energy, its angular momentum, and its magnetic quantum number, which ranges from *–l* to *+l* and indicates how many orbitals, and hence how many electrons, exist in each atom. A set of *allowed states* which share the same quantum number *n* is called the *electron shell*. Orbitals with

[2] The endnotes are to be found on pp. 108-116.

the same quantum numbers n and l are called *subshells*. The number of orbitals in a shell is the square of the principal quantum number, i.e., n^2. Experimental evidence suggests that an orbital can hold no more than two electrons distinguished by the fourth quantum number s called the *spin quantum number*. Thus, the n^{th} shell can accommodate $2n^2$ electrons, e.g. the first shell can accommodate only two electrons, and the number of electrons in a subshell is $2l+1$.
An atom can possess multiple orbitals, each of which has its own specific energy level and properties. The electron configuration corresponding to the lowest electronic energy is called the *ground state*.

Once a single atom is excited by the absorption of a photon, it can return to the ground state and dissipate its energy by emitting the photon of the same wavelength it absorbed, or by emitting heat. Since single atoms can absorb photons whose energy matches the energy of atomic orbitals, the absorption and emission bands of single atoms are rather narrow, and the emitted or absorbed light contributes to the colors of our surroundings inconsiderably. As a rule, most atoms do not exist in nature as single units. Instead, they join other atoms through chemical *bonds* to form a molecule. Since some electrons are shared by atoms of a molecule, the resulting molecular orbitals are not as precisely determined as atomic orbitals in a single atom, due to variations in the bond behavior of atoms within the molecule. This variation leads to the dispersion of energy levels for each excited state and, consequently, to the broadening of absorption bands within a molecule. Complex molecules have multiple excited states and can absorb and emit light at multiple wavelengths.

Unlike a single atom, an excited molecule can return to its ground state by many possible pathways [20], some of which are followed by light emission, while others result in the excited molecule's direct return to the ground state without light emission. In this paper, we will consider processes called *photoexcitation* during which molecules are excited by absorbing photons. The emission of a photon, accompanying the de-excitation of the molecule excited by an incident photon and the return of the molecule to a lower-energy state is called *photoluminescence*, the particular cases of which are *phosphorescence* and *fluorescence*. The period between absorption and emission resulting in fluorescence is typically 10^{-9}-10^{-6} seconds. Photoluminescence emission which takes place after a period longer than 10^{-5} seconds is considered phosphorescence [21]. Fluorescence emission stops practically simultaneously with the turning off of the excitation light source, while phosphorescence can be seen after the exciting illumination has been discontinued and may last for seconds and even minutes after the event. Substances emitting light when illuminated are considered *luminophores* and can be classified into two subcategories: *fluorophores* that exhibit fluorescence and *phosphors* that exhibit phosphorescence.

The Jablonski diagram, which is a convenient way to describe the possible de-excitation pathways, is used in Fig. 2.2 to illustrate the process of photon absorption, fluorescence phosphorescence and the molecule's direct return to its ground state without emission. States with the total spin quantum number 0 are called *singlet* states. Singlet states in Fig. 2.2 are marked as S_0 (the ground state), and S_1, and S_2 (the excited states). States with the total spin quantum number 1 are called *triplet* states, and are marked as T_1 and T_2. Vibrational energy levels are associated with each electronic state depicted by horizontal lines and marked by numbers 0, 1, 2,… and so forth. At room temperature, the majority of molecules are located at the lowest vibrational energy level S_0; therefore, to show the absorption process, the vertical arrows start from level S_0. After absorbing a photon, the molecule is excited to one of the vibrational levels of the electronic states S_1, S_2, …, and so forth. During the time between

absorption and emission, the excited molecule can be involved in interactions with its molecular environment, and its vibrational level partially dissipates, transferring the excited molecule to one of the relaxed single states S_1, S_2, …, and so forth, from which de-excitation processes occur. The *internal conversion* (IC) and *intersystem crossing* (ISC) are non-radiative transitions from a higher to a lower electronic state with the same (in the case of IC) or different (in the case of ISC) total spin quantum number. The excitation energy in both of the processes – IC and ISC – transforms into heat. These two processes are depicted in Fig. 2.2 by wavy arrows. The vertical arrows starting from state S_1depict fluorescence, and the arrows starting from state T_1 depict phosphorescence. If the energy difference between states S_1 and T_1 is small, an excited molecule can return to the ground state through another pathway: a reverse ISC (not shown in Fig 2.2) can occur from energy level T_1 to S_1 and is followed by fluorescence. This fluorescence emission is called *delayed fluorescence* because, before emitting a photon from state S_1, the excited molecule, for some time, stays in state T_1.

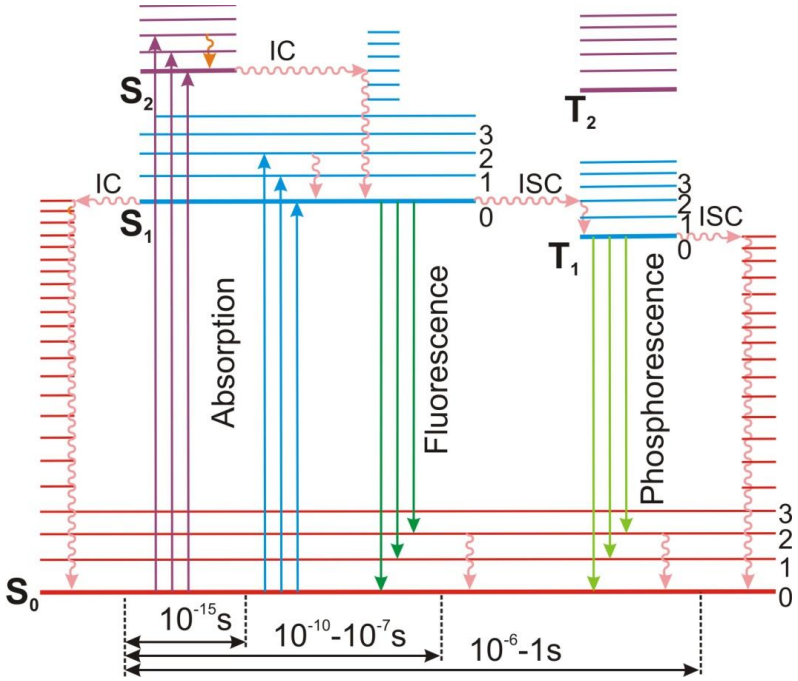

Figure 2.2. The Jablonski diagram [1].

2.2 Emission and Excitation Spectra

If the energy of an incident photon is insufficient to promote the transition from energy state S_0 to S_1 or S_2, then no absorption occurs. If the energy of the incident photon exceeds the amount necessary for a simple transition, the excess energy is converted into vibrational and rotational energy. The absorption of a photon can only occur when a molecule interacts with the incident light of specific wavelengths known as *absorption bands*. The distribution of the probability of various transitions from energy state S_1 to various vibration levels of S_0 denoted by $F(\lambda_F)$ represents an *emission*, or a *fluorescence*, *spectrum*. The steady-state fluorescence intensity I_F at the wavelength λ_F is proportional to $F(\lambda_F)$ and to the number of photons absorbed at the

excitation wavelength λ_E. Fluorescence intensity is thus a function of both excitation λ_E and emission λ_F wavelengths. In practice, an emission spectrum is represented by a variation of fluorescence intensity I_F as a function of emission wavelength λ_F. A variation of fluorescence intensity I_F as a function of excitation wavelength λ_E represents *the excitation spectrum*. In practice, the emission and excitation wavelengths λ_F and λ_E are selected by a monochromator with certain wavelength bands $\Delta\lambda_F$ and $\Delta\lambda_E$.

Due to the loss of vibrational excitation energy during the excitation/emission cycle, fluorescence emission occurs, as a rule, at a lower energy level. The lower energy level results in the emission occurring at longer waves, i.e. we can observe a redshift of the emission spectrum – the shift in the direction of longer waves. The redshift of the band maxima of absorption and emission spectra is called the *Stokes shift*. Typical emission and excitation spectra are presented in Fig. 2.3. Emission and excitation spectra usually exhibit, at least, one *spectral peak* which is defined as the local maximum of the measured magnitude of fluorescence intensity $I_p=max(I_F)$. The local maximum should be determined using the specified magnitude of threshold depending on noise or measurement errors [22]. The wavelength λ_p, at which a local maximum I_p is observed, is defined as the *peak wavelength*. The full width at half the maximum (FWHM) is the most common parameter used to measure a peak width, e.g., the *bandwidth* of fluorescence emission. The wavelength λ_b, corresponding to half of the local maximum $0.5I_p$, can be determined by fitting measured data I_F using an appropriate function.

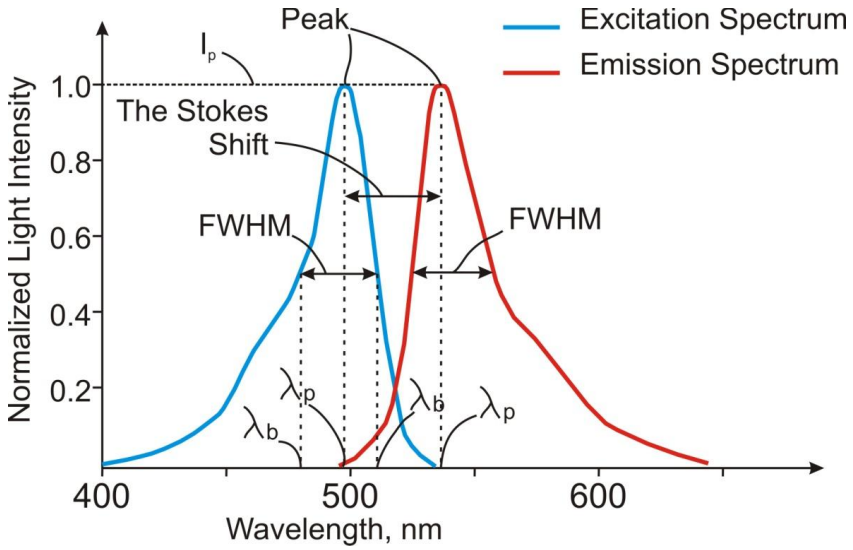

Figure 2.3. Typical emission and excitation spectra.

Considering that the number of absorbed photons is proportional to the intensity I_A of the absorbed light, fluorescence intensity I_F can be written as:

$$I_F(\lambda_E, \lambda_F) = kF(\lambda_F)I_A(\lambda_E) \qquad (2.1)$$

where I_F and I_A are fluorescence intensity and the absorbed intensity, respectively, in arbitrary units; λ_E and λ_F are excitation and emission wavelengths, respectively, in nm; and k is the proportionality factor, depending on the optical configuration of the instrumentation such as the

solid angle through which the instrument collects fluorescence and also on the bandwidth of the monochromator $\Delta\lambda_F$.

The absorbed intensity I_A is defined as the difference between the intensity of the incident light I_0 and the intensity of the transmitted light I_T. The efficiency of light absorption $A(\lambda)$ by an absorbing substance at the wavelength λ is calculated, as a rule, using the *Beer-Lambert* Law:

$$A(\lambda) = \log\left[{I_0(\lambda)}/{I_T(\lambda)}\right] = \varepsilon(\lambda) l c \qquad (2.2)$$

where λ is a wavelength in nm; A is the dimensionless absorption coefficient; I_0 and I_T are the light intensities of the beams entering and leaving the absorbing substance, respectively; ε is the molar absorption coefficient, in $L \cdot mol^{-1}cm^{-1}$; c is the concentration of absorbing elements, in $mol \cdot L^{-1}$; and l is the absorption path length, in cm.

According to the Beer-Lambert law (Eq. 2.2), the intensity of the transmitted light I_T of wavelength λ_E is:

$$I_T(\lambda_E) = I_0(\lambda_E) exp\,[-2.3\varepsilon(\lambda_E) l c] \qquad (2.3)$$

Calculating I_A as the difference I_T - I_0 and inserting it into Eq. (1.1) yields:

$$I_F(\lambda_E, \lambda_F) = kF(\lambda_F) I_0(\lambda_E)\{1 - exp\,[-2.3\varepsilon(\lambda_E) l c]\} \qquad (2.4).$$

The portion of electromagnetic radiation of the emitted light from about 390 to 700 nm is visible to the human eye and is called the *visible* (VIS) *spectrum*. A *spectral color* is an electromagnetic radiation composed of a single wavelength. To determine what spectral color we are dealing with, the color wavelength should be correlated with the wavelength shown in Table 1 [23].

2.3 Saturation and Photo-bleaching

In the theory of spectroscopy, fluorescence is hardly regarded as a linear process, where the emitted fluorescence intensity is linearly dependent on the intensity of excitation light because the concentration of the excited molecule remains constant. Most of *fluorophores* are able of repeating excitation and emission cycles many hundreds and thousands times. The measurements under these conditions are called *steady-state measurements*. The steady-state fluorescence intensity is given by

$$i_F = \alpha i_0 \phi_F \qquad (2.5)$$

Table 1.1

Correlation Chart for Color Ranges

Spectrum	Spectral color	Range
Ultraviolet	Far-ultraviolet	10-200
	Near- ultraviolet	185-380
VIS region	Violet	380-450
	Blue	450-495
	Green	495-570
	Yellow	570-590
	Orange	590-620
	Red	620-750
Near-infrared		750-3000

where i_F and i_0 are the steady-state fluorescence intensity and the intensity of the incident light, respectively, in the amount of fluorescence in photons per liter and per second; α is a dimensionless proportionality factor representing a fraction of absorbed photons of the incident light; and Φ_F is the fraction of excited molecules – the fluorescence *quantum yield* – which return to the ground state by emitting fluorescence photons. In practical measurements, the measured quantity of the fluorescence intensity I_F is proportional to I_0, where the proportionality factor depends merely on instrumental efficiency factors.

However, at high light intensities, the frequency at which an individual molecule gets excited is determined by the average lifetime of the excited state τ_e and is independent of the excitation light intensity. This effect is called fluorescence *saturation*. If τ_p is the average time during which, after relaxation, a molecule has to wait for the next photon, and I_τ is fluorescence intensity where $\tau_p=\tau_e$, then the relationship between effective excitation light intensity, the amount of light that is absorbed by molecules I_{eff}, and the intensity of excitation light I_0 can be represented by the equation [24]:

$$I_{eff} = {}^{I_0 I_\tau}/_{(I_0 + I_\tau)} \qquad (2.6)$$

The relationship between I_{eff} and I_0 is shown in Fig. 2.4. Both the excitation light intensity I_0 and the effective light intensity I_{eff} are expressed relative to the light intensity I_τ. As can be seen from Figure 2.4, the curve asymptotically approaches the maximum value $I_{eff} = I_\tau$.

While some of the pathways used by an excited molecule for de-excitation lead to the ground state, others may lead to an altered state, in which the molecule can no longer repeat excitation and emission cycles. The effect of the destruction of a fluorophore in a process of

photoexcitation is called *photo-bleaching* and can be responsible for the non-linear dependence of emitted fluorescence intensity on the intensity of excitation light.

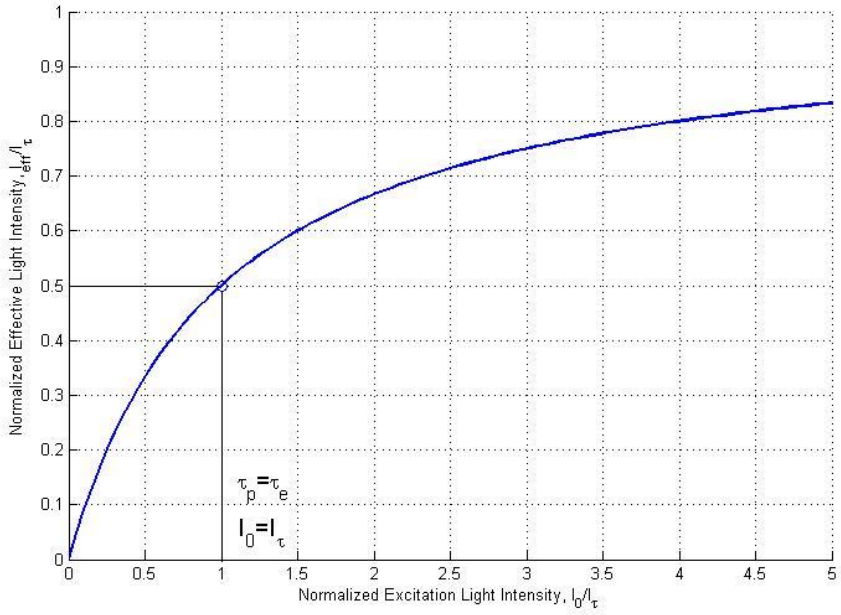

Figure 2.4. Fluorescence saturation.

2.4 Fluorescence Decay

If a very short pulse of light brings a certain number of molecules to the excited state by absorbing photons at time 0, after which some of them return to the ground state, the fluorescence intensity i_F at time t is proportional to the instantaneous concentration of the molecules that are currently in the excited state and is given by

$$i_F(t) = I_F(0) \cdot \exp\left(-{}^{t}/_{\tau}\right) \qquad (2.7)$$

where I_F is the fluorescence intensity in arbitrary units; t is time in sec; and τ is the *fluorescence lifetime* in sec.

The emission of fluorescence photons from a fluorophore does not occur at a fixed time. The fluorescence lifetime of a fluorophore τ is defined as the time required by a certain population of N excited molecules to be reduced by the factor of $1/e$ via a loss of energy by emitting fluorescence or heat. The typical fluorescence decay is presented in Fig. 2.5.

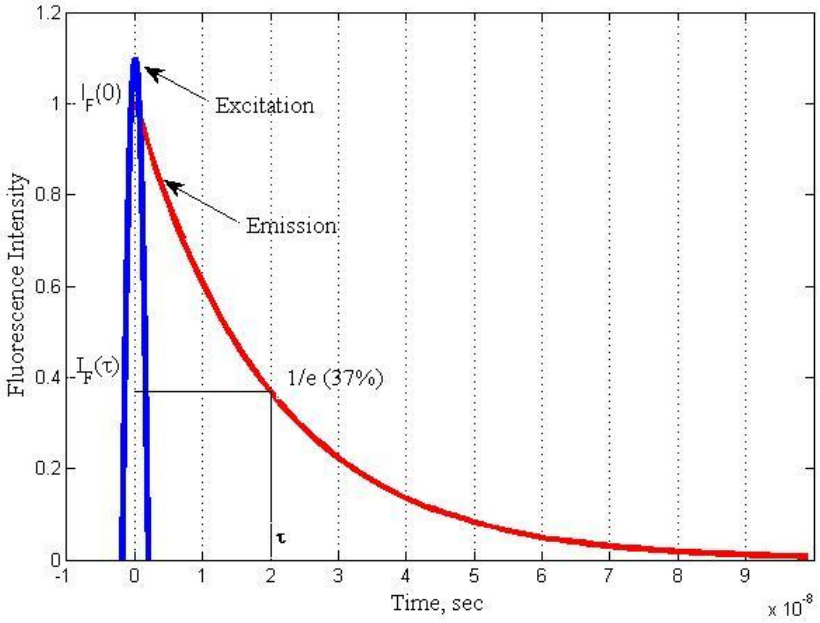

Figure 2.5. Typical fluorescence decay.

2.5 Fluorescence Excitation Mechanisms

Fluorescence can be observed as a result of a three-stage process: 1- photon absorption, 2 - excited lifetime, and 3 - photon emission, labeled in Fig. 2.6 with 1, 2, and 3, respectively. A *single-photon excitation* mechanism of fluorescence, represented in Fig. 2.6a, leads to the Stokes shift (See Fig 2.3). Under some circumstances, fluorescence emission photons are at a higher energy level than the photons of excitation light. The difference in the wavelength positions of the band maxima of the absorption and the emission spectra in this case is called the *anti-Stokes shift*. This shift is possible due to the *multi-photon excitation* mechanisms which involve two or more absorbed photons per one emitted photon. For instance, two-photon excited fluorescence occurs when two electrons appear together in the proper place, called a virtual state, and at the proper time for the summation of their energy values. A *two-photon excitation* mechanism of fluorescence is represented in Fig. 2.6b. A simultaneous absorption of these photons occurs rather rarely, and because the probability of a two-photon process scales as square of the incident light intensity, a high-photon flux of photons is needed to increase the probability of this process.

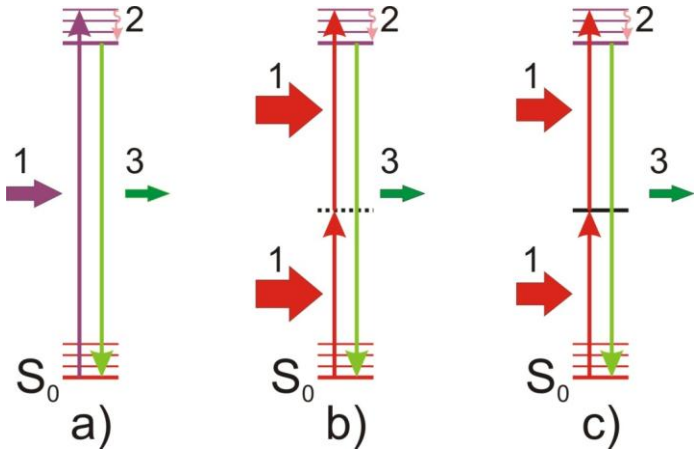

Figure 2.6. Fluorescence excitation mechanisms: a) single-photon excitation fluorescence; b) two-photon excitation fluorescence; and c) upconversion fluorescence.

Upconversion fluorescence (UCF) is another mechanism resulting in the conversion of low-energy photons into higher-energy photons. The UCF mechanism involves a multistep excitation by absorbing photons and transferring the molecule from the ground state to an intermediate real state, where a non-simultaneous interaction with another photon may occur (See Fig. 2.6c). The probability of the molecule initial excitation to a real intermediate state and its consequent non-simultaneous excitation to a higher state is much higher than the probability of a two-photon excitation and, therefore, the UCF mechanism allows for the use of the relatively low incident excitation light intensity.

2.6 Fluorescence Quenching

Fluorescence quenching is a process which decreases the intensity of fluorescence emission of a given substance. It can be achieved through a variety of process mechanisms, such as dynamic quenching, static quenching, quenching by energy transfer, and others. Dynamic, or collisional, quenching is a mechanism of the de-excitation of molecules occurring when the excited fluorophore experiences a contact with atoms or molecules of a *quencher* which facilitates non-radiative transitions to the ground state. Because dynamic quenching decreases the population of excited molecules without light emission, the fluorescence lifetime decreases as well. The Jablonski diagram, presented in Fig. 2.7, illustrates the fact that quenching does not change the energy of emitted photons; however, it decreases the population of excited molecules. Such depopulation caused by quenching occurs at the rate k_qQ, where Q is the concentration of quenching species. The dependence of the emission intensity I on the quencher concentration is given by the Stern-Volmer equation [1]:

$$I_0/I = \tau_0/\tau = 1 + k_q\tau_0 Q = 1 + K_D Q \qquad (2.8)$$

where I and I_0 are fluorescence intensities in the presence and absence of the quencher, respectively, in arbitrary units; τ and τ_0 are the fluorescence lifetimes in the presence and absence of the quencher, respectively, in sec; k_q is the diffusion-dependent quenching rate coefficient in M^{-1}sec; Q is the concentration of the quencher, in M; and K_D=K_{SV} is the Stern-Volmer constant, in M^{-1}.

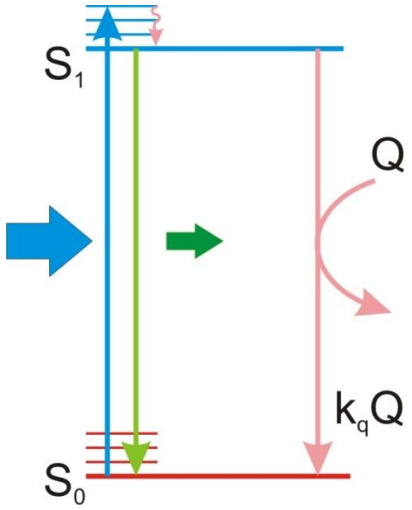

Figure 2.7. The Jablonski diagram illustrating dynamic quenching.

In static quenching caused by the formation of non-fluorescent complexes, τ does not change because the only observed fluorescence is produced by uncomplexed molecules which have the same τ as before quenching occurs. Thus, K_{SV} in Eq. (2.8) is represented by the static Stern-Volmer quenching constant K_S which is independent of τ.

$$I_0/I = 1 + K_S Q \qquad (2.9)$$

Static and dynamic quenching can be distinguished using temperature effects affecting quenching. While dynamic quenching rates increase with higher temperatures, due to an increase in diffusion rates, static quenching rates increase with lower temperatures because complex molecules tend to become stronger.

2.7. Diffusion

Dynamic quenching is a diffusion-controlled process. From Eq. 2.9, one can see that the Stern-Volmer constant $K_D=k_q\tau_0$ is related, via quenching rate coefficient k_q, to the diffusion of the quencher molecules in the media. According to the theory of diffusion-controlled reactions, along with the diffusion constant D, the temperature and viscosity of the media are important parameters characterizing quenching [20, 25, 26]. The diffusion process can be modeled using the diffusion equation, also known as Fick's second law [27]:

$$D\,\partial^2 Q(x,t)/\partial x^2 = \partial Q(x,t)/\partial t \qquad (2.11)$$

where D is the diffusion constant of the quencher, t is time, and Q is the quencher concentration in the media.

2.8 Sensors and Sensor Systems

Sensors are critical components of all measurement and control systems. In scientific literature, numerous terms are used as synonyms for ‘sensor’, including transducer, detector, meter, probe, gage, and indicator. The list of synonyms for the term ‘sensor’ can be continued (See Section 3.3.2) The definition of ‘sensor’ proposed by the Instrument Society of America [American National Standard, ANSI MC6.1, Electrical Transducer Nomenclature and Terminology, 1975] has been applied to electrical transducers and, thus, cannot be applied to any sensor. In their report [28], the Committee on New Sensor Technologies: Materials and Applications recognized that the term ‘sensor’ is the most widely used in the scientific literature and chose to adopt the following definitions:

Sensor element: The fundamental transduction mechanism (e.g., a material) that converts one form of energy into another. Some sensors may incorporate more than one sensor element (e.g., a compound sensor).

Sensor: A sensor element including its physical packaging and external connections (e.g., electrical or optical).

Sensor system: A sensor and its assorted signal processing hardware (analog or digital) either in or on the same package or discrete from the sensor itself.

If luminous radiation is used in any of incorporated sensor elements, the sensor is considered an *optical sensor* (OS). The *OS System,* therefore, is an optical sensor and its assorted signal processing hardware. In the OS system, the measured object’s magnitude, the measurand, or the input signal (V_i) introduce modifications or modulations in some of the characteristics (transmission, reflection, dispersion, absorption, etc.) of light in an optical system. After such modifications or modulations are detected, processed, and conditioned, the system will deliver the output signal (V_o), usually in the electric domain, which is a valid reproduction of the object variable V_i (See Fig. 2.8).

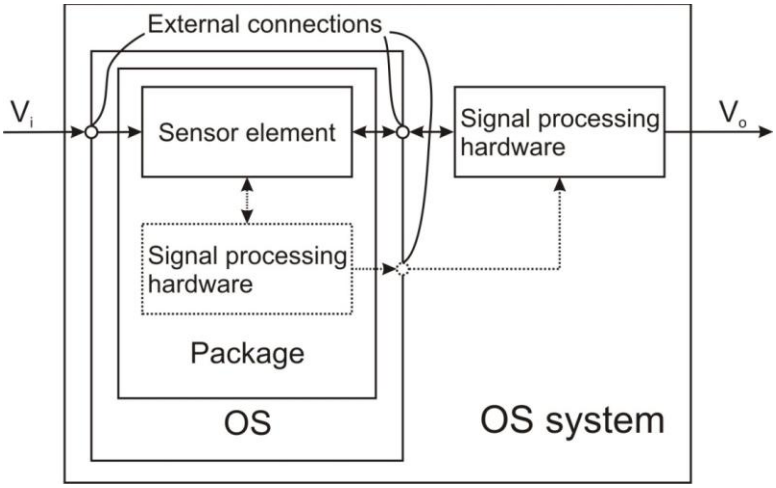

Figure 2.8. Conceptual block diagram of a general OS system.

Sensor performance can be characterized by using various static and dynamic parameters [29, 30]. A sensor is typically characterized by three basic parameters [31]:

Sensitivity: a measure of the change in sensor output that occurs when the being measured parameter changes by a given amount. The sensitivity of a sensor, therefore, can be considered as the slope of the calibration graph.

Resolution: the smallest change the sensor can detect in the quantity that it is measuring.

Selectivity: the ability to sense a particular substance free from interference.

Limit of detection: in analytical chemistry, the lowest quantity of a substance that can be distinguished from the absence of that substance (blank value) within a stated confidence limit (generally 1%). The limit of detection is usually estimated from the mean of the blank.

Response time: the time for a sensor to respond from zero concentration to a step change in concentration. The parameter used to characterize the response time in this study is the time t_{65} required to reach 65% of the final concentration change.

Dynamic range: the ratio between the largest and the smallest possible values of the measured signal.

Chapter 3

Development of the Prototype of a Portable, Low-Cost Oxygen Sensor Based on Fluorescence Quenching

3.1 Prior Art in Optical Sensors

As oxygen is a critical component in various fields of industry, energy, medicine, and environment, researchers have exerted significant efforts to develop reliable techniques for measuring oxygen concentrations, which resulted in a wide variety of oxygen sensors that proved to be reliable in different areas. Among the most known conventional gas-phase oxygen sensors [32][3] are *potentiometric equilibrium sensors*, which typically use oxygen-ion conducting materials as the electrolyte; *amperometric sensors*, where oxygen is pumped from one side of the electrolyte to the other by the application of an external potential; *semiconducting metal oxide sensors* based on the change of properties of oxide semiconductors upon their exposure to the test gas; *polarographic sensors*, the best known of which are Clark electrodes, based on the electromechanical reduction of oxygen at a negatively polarized electrode; *paramagnetic sensors*, which exploit the paramagnetic properties of oxygen; and *optical sensors*, which can be classified in terms of a certain optical property actually being measured or the technique used. Over the past several years, new types of oxygen sensors have started gaining in popularity in industrial applications [33]. However, most of the above-mentioned sensors are adequate only for a limited range of applications.

Numerous books and review articles have been published by experts in the field of optical chemical sensors, where the authors have highlighted the advantages of optical sensing over other transduction methods [5]. Oxygen optical sensors (OOSs) provide the measuring of oxygen concentration in a non-intrusive manner – oxygen is neither consumed nor heated during the measurements, and no moving parts are employed. However, according to the literature, only fluorescence-based OOSs have competitive advantages providing the possibility of adjusting design characteristics to satisfy simultaneously such customer needs as high sensitivity and a quick response time, low cost and low power consumption, non-distractive and non-invasive measurements, and easy miniaturization. Although considerable progress has been made in the development of OOSs, a need for a simple, low-cost, and robust design of the OOS, which, at the same time, is capable of high-sensitivity detection, still exists.

Supported by an industrial grant, the Optoelectronic Sensor Laboratory at Stony Brook University is currently conducting the Project "Development of a portable low-cost oxygen sensor based on fluorescence quenching." In this chapter, I present the results of the first stage of our work "Development of the prototype of an oxygen sensor based on fluorescence quenching."

I will exclude from further consideration potentiometric equilibrium sensors, amperometric sensors, semiconductor metal oxide sensors, polarographic sensors, and paramagnetic sensors because their characteristics do not simultaneously satisfy all mentioned-above customer needs. I will consider the most known conventional OOSs [5] – OOSs based on absorption spectroscopy, on measuring the refractive index, and on fluorescence quenching, in order to demonstrate the advantages of the last-mentioned type.

[3] The endnotes are to be found on pp. 108-116.

3.1.1. OOSs based on absorption spectroscopy. A schematic drawing of an OOS based on the optical absorption technique is presented in Fig. 3.1. To measure oxygen, the spectrally pure laser diode (LD) is used. This LD is controlled by temperature and current in order to be precisely tuned thermally and electronically to a particular oxygen absorption line, which has been selected for its strength and its spectral match to the output wavelength of the LD [34, 35]. A beam splitter splits the laser beam in two beams – one is directed toward the signal photo-detector, and the other toward the reference photo-detector. The beam directed toward the signal photo-detector passes through a sample chamber filled with oxygen. As the oxygen concentration in the sample chamber increases, the light intensity measured with the signal photo-detector decreases due to light absorption by oxygen molecules. This attenuated intensity is compared with light intensity measured by the reference photo-detector, to calculate oxygen concentration in the sample chamber.

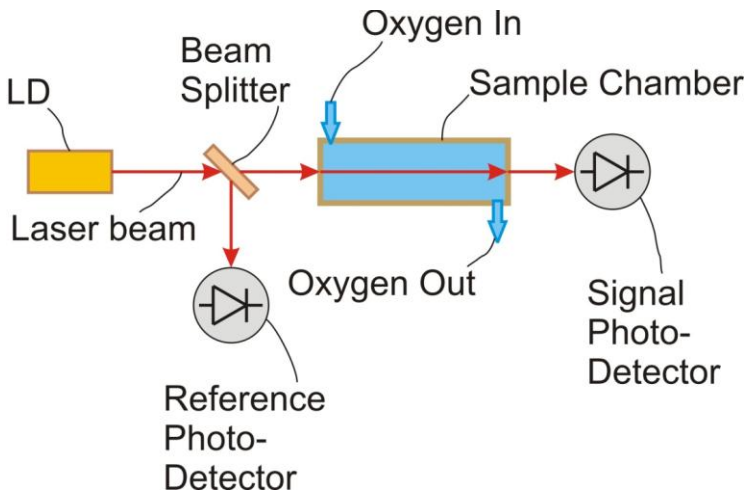

Figure 3.1. Operating principle of an optical absorption oxygen sensor.

The main disadvantage of the absorption-based sensor is that the change of the signal is insignificant, compared to the background signal, and the noise introduced by the LD deteriorates the detectability of the sensor.

3.1.2. OOSs based on measuring the refractive index. Every substance has a unique refractive index that can be measured accurately. The instruments for measuring substances' refractive index, in order to assess their composition or purity, are called refractometers. When a light beam passes through two parallel slits whose width is of the magnitude of the light's wavelength, interference patterns are observed. Bright fringes are produced by the light passing through different slits and arriving in phase, and dark fringes – by the light arriving out of phase. If light is passing through sample chambers containing gases with different refractive indices, two sets of fringes are produced, and the displacement between them can be measured as the difference in the refractive indices of these gases [36].

The operating principle of a refractometer is illustrated in Fig. 3.2. The light from the light source is split into two parallel beams by a beam splitter. One beam is passing through the

reference chamber containing air, for instance, and the other is passing through the measuring chamber, containing the gas under test, whose concentration is to be measured. The beams can be reflected back through the chambers to enhance the effect. Each beam is passing through a slit, producing two sets of interference fringes. A linear diode array can be used to accurately detect the varying displacement between the fringes.

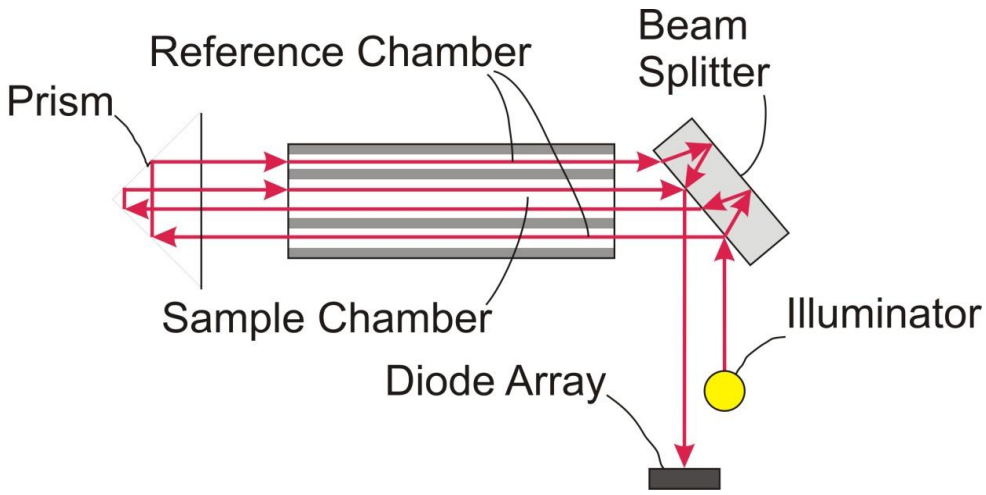

Figure 3.2. Operating principle of a refractometer.

The main disadvantage of the refractometer is that it can be inaccurate when oxygen is contaminated by water vapor, or it is mixed with some other gases because the refractometer measures the refracting index of the total mixture, and does not measure the concentration of any specific component of the mixture.

3.1.3. OOSs based on fluorescence quenching. OOSs employing the fluorescence technique are based on the principle of fluorescence quenching with oxygen. The degree of the fluorescence intensity quenching depends on oxygen concentration *Q*; therefore, the measured fluorescence intensity *I* can be used to calculate the concentration of oxygen (See Eq. 2.8). The operation of a fluorescence-based OOS requires an illuminator, a sensor element including fluorophores, and a photo-detector. Most of OOSs also need, for their operation, an exciter and barrier filters, lenses, and optical fibers. Fig. 3.3 illustrates the operating principle of a fluorescent OOS.

The illuminator sends excitation light toward the sensor element. The exciter filter permits only selected wavelengths from the illuminator to pass toward the sensor element and excite the incorporated fluorophore. If the sensor element is illuminated by the excitation light of wavelengths, selected from the fluorofore's absorption wavelength band, the fluorofore fluoresces. When the fluorofore encounters an oxygen molecule, the excitation energy is transferred to the oxygen molecule in a non-radiative transfer, quenching the fluorescence signal which is registered by the photo-detector. The barrier filter is used to suppress the excitation wavelengths passing toward the photo-detector. Optical fibers can be used to deliver excitation light from the illuminator to the sensor element and emission light from the sensor element to the photo-detector. Some of OOSs use lenses to focus excitation light on the sensor element and

collect emission light. The major challenge and drawback of the fluorescence-based OOS is its cross-sensitivity to temperature and humidity.

The comparison of schematic diagrams illustrating the operating principle of the most known OOSs presented in Figures 3.1-3.3 shows that the design of an OOS, based on fluorescence quenching, allows us to obtain a powerful output signal thanks to the easily adjustable layout with inexpensive components, compared to other OOSs [7, 37].

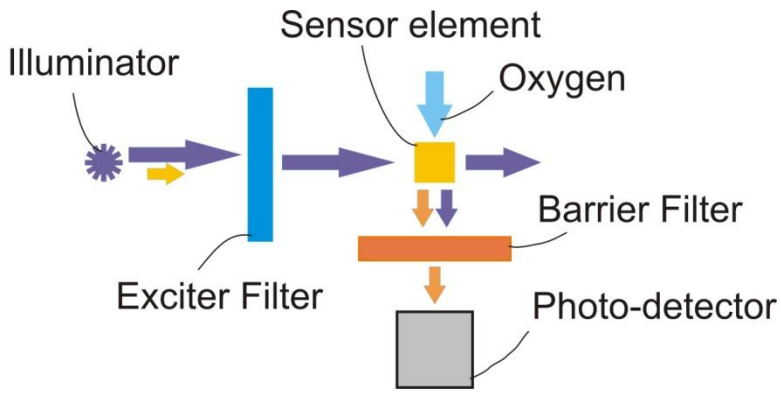

Figure 3.3. Operating principle of the OOS based on fluorescence quenching.

3.2. Prior Art in Fluorescence-Based OOSs

The operating principle of fluorescence-based OOS was presented in Section 3.2.3. However, the quality of a sensor system depends not only on the operating principle of the OOS, but also on the quality and matching of all components in the system, the optical design configuration of the OOS, its measurement techniques, and its evaluation software. In this section, I summarize the progress made in the field in terms of the OOS components, optical design configuration, measurement techniques, and data processing used.

3.2.1. Measurement techniques. Existing OOSs employ either an intensity- or a lifetime-based technique of measuring the sensor element's fluorescence response to oxygen concentration. The *intensity-based technique* is achieved by measuring the intensity I of a fluorescence response and calculating the oxygen concentration Q using Eq. 2.8, while the fluorescence *lifetime-based technique* involves measuring the fluorescence lifetime τ in either the time domain [38-40] or the frequency domain [37, 40, 41], and calculating the oxygen concentration Q using Eq. 2.8.

Time-domain lifetime detection. The most common time-domain lifetime detection technique based on combining pulsed excitation with time-gated detection is presented in Fig. 3.4. A pulse of excitation light is indicated in the figure by the blue line, and emission intensity is represented by the red line. The photo-detector is gated in such a way that it acquires windows of emission intensity data indicated by color regions. If the excitation decay is observed after the excitation pulse has died out, the difference Δt between the beginning and the end of two time

windows is equal, and the ratio of the integrated data collected during the two windows is I_1/I_2, then the fluorescence lifetime can be determined from the equation [39, 42]:

$$\tau = {t_2 - t_1}\Big/{\ln\left({I_1}/{I_2}\right)}. \qquad (3.1)$$

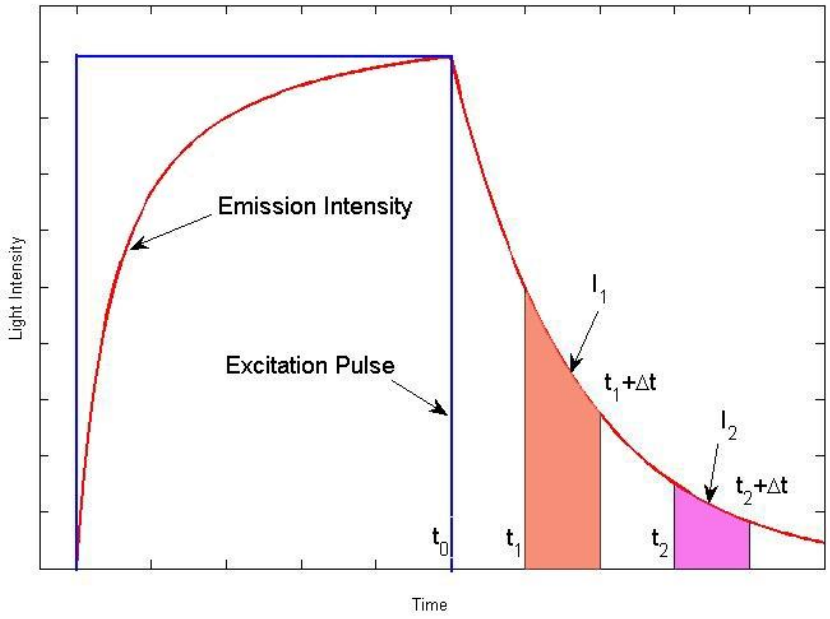

Figure 3.4. Time-domain detection technique.

As the photo-detector detects the fluorescence signal only when the illuminator is not emitting, and the effects of the ambient light are insignificant, the use of the barrier filter shown in Fig. 3.3 is not mandatory for time-domain lifetime detection [25]. However, in commercial low-cost applications, the lifetime is measured in the frequency domain because the direct measurement of the fluorescence lifetime requires expensive and sophisticated instrumentation and involves with time-consuming data processing [37, 40, 43].

Frequency-domain lifetime detection. Frequency-domain lifetime detection is based on measuring the phase shift between the excitation light intensity and emitted light intensity waveforms [37, 40, 44-47]. The signals resulting from the sinusoidal excitation of a fluorophore are presented in Fig. 3.5. The relationship between the phase shift ϑ of the fluorescent signal, in radians, the emission lifetime τ, in seconds, and modulation frequency f, in Hz, can be presented as follows [1]:

$$\tau = {tan\,\vartheta}\Big/{2\pi f}. \qquad (3.2)$$

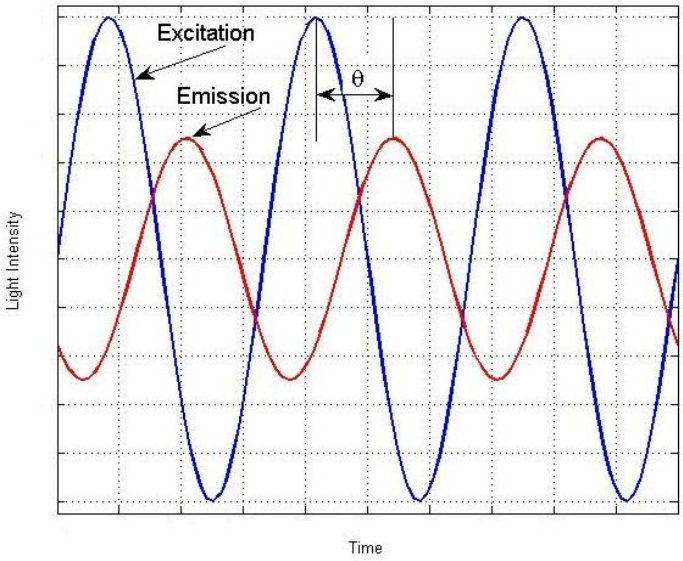

Figure 3.5. Frequency-domain detection technique.

The oxygen concentration Q is calculated using Eq. 2.8, where the Stern-Volmer constant K_D is obtained from the linear calibration plot of τ_0/τ-*1* vs. *Q*. However, when the fluorofore is immobilized on a solid support to create a sensor element, the decay profile usually departs from *monoexponential* kinetics predicted by Eq. 2.7:

$$I_t = \sum_i I_i e^{-t/\tau_i}. \qquad (3.3)$$

Generating calibration curves for lifetime measurements may be a rather complex problem because *multiexponential* decays (See Eq. 3.3) are rather a rule than an exception. In this case, to fit the multiexponential kinetic data to a sum of exponentials I_t, mean lifetime values τ_M characterizing the return of the excited molecule to the ground state are used [48]:

$$\tau_M = \sum_i I_i \tau_i \Big/ \sum_i I_i. \qquad (3.4)$$

In practice, decays are represented by a sum of two exponential decays. Even so, the sum of two lifetimes does not obey the simple Stern-Volmer equation (2.9) [49].

Frequency-domain lifetime detection measurements offer certain advantages in respect of the performance of the OOSs. As the lifetime is an intrinsic property of the fluorophore, instrumental fluctuations, loss of the fluorophore, such as photo-bleaching and photodegradetion, do not affect the OOS performance [43]. Nevertheless, the low-cost phase-shift-based lifetime instrumentation can be used with fluorophores, whose lifetime is greater than 100 ns, which limits its use to the systems based on metal complexes such as platinum metals (Ru, Ir, Os, and Pt) [50].

Intensity-based technique. The intensity-based technique involves only the detection of fluorescence intensity and enables simpler data processing and the implementation of less expensive instrumentation. According to the intensity-based technique, the oxygen concentration *Q* is calculated using Eq. 2.8, where the Stern-Volmer constant K_{SV} is obtained from the linear

calibration plot of $I_0/I-1$ vs. Q. However, most of fluorophores exhibit the presence of both quenching mechanisms – dynamic and static – resulting in a non-linear K_{SV} vs. the Q plot of experimental data (downward curvature) which can be fitted by the modified Stern-Volmer equation:

$$I_0/I = (1 + K_D Q)(1 + K_S Q) \qquad (3.5)$$

where K_D and K_S are dynamic and static Stern-Volmer quenching constants, respectively. The non-linearity of the real response of some fluorophores (See Eq. 3.5) hinders the acquisition of reliable calibration curves. Various mathematical models have been proposed to linearize the Stern-Volmer plot for generating calibration curves used for calibrating sensors. For example, an elegant model was derived from the Stem-Volmer equation taking into consideration two populations of ruthenium within the sensor element, one quenchable and one non-quenchable [51]. The measured intensities in the absence and in the presence of a quencher are presented as sums of non-quenchable I_{NQ} and quenchable I_Q light: $I_0=I_{0Q}+I_{NQ}$ and $I=I_Q+I_{NQ}$. Rearranging and putting the quenchable intensities into the Stern-Volmer equation (2.8), we obtain:

$$I_{0Q}/I_q = (I_0 - I_{NQ})/(I - I_{NQ}) = 1 + K_{SV} Q \qquad (3.6)$$

or

$$I = I_{NQ} + (I_0 - I_{NQ})/(1 + K_{SV} Q) \,. \qquad (3.7)$$

As can be seen from Eq. 3.7, in the absence of the quencher, the measured signal I is equal to $I_{0Q}+I_{NQ}$; when quencher concentration increases, the measured signal decreases to I_{NQ}. A linear calibration plot can be generated by using the fitted Stern-Volmer constant to plot the measured signal I vs. $(1+K_{SV}Q)^{-1}$.

The described intensity-based technique has several drawbacks, including the dependence of the observed fluorescence emission on fluctuations of excitation light-source intensity, variations in the efficiency of transmission optics, as well as aging and photo-bleaching of the fluorophores. Nevertheless, this technique has been successfully used for gaseous oxygen detection [52-59]. The source intensity, the state of optical devices, and photo-detector sensitivity fluctuations can be corrected by several methods. The *ratiometric method*, where the sensor element contains two fluorophores with different spectra, is considered to be the most investigated: one fluorophore is oxygen-sensitive, and the other is oxygen-insensitive, the latter being used as a temperature reference to account for intensity fluctuations. For example, the investigation of an OOS with a ruthenium (II) complex, used as an oxygen-sensitive fluorophore, and an oxygen-insensitive fluorophore, used as a reference to account for intensity fluctuations, showed that the intensity referencing not only markedly improved the response curves obtained by intensity-based measurements, but also extended the linear dynamic range beyond the corresponding value of the lifetime-based measurements [57].

The experimentally confirmed theoretical formalization and mathematical modeling made it possible to quantify all the contributions related to photochemical, thermal and oxidative degradation of both the polymeric matrix and the incorporated fluorophore and determine light intensity drift and Stern-Volmar constant drift [60]. The obtained results can be utilized in the design of a new light-intensity-based OOS working with high accuracy and precision [61]. The

proposed algorithm makes the light-intensity-based OOS as accurate as the most expensive phase-shift-based commercial OOS, even if measurements are conducted under unfavorable conditions.

3.2.2. Sensor components. ***Sensor elements*.** The sensor element used in OOSs includes an *optical oxygen sensing material* entrapped in a *matrix* with a high permeability to oxygen [9, 62, 63]. It should be noted that, in different papers, numerous terms are used to identify the sensor element and its components. For example, the sensor element has been mistakenly called "sensor" in the review [9] or referred to using the terms "chemosensor" [8, 20, 64], "membrane" [43, 54, 56, 65] or "film" [27, 52, 58, 66]. The terms "indicator" [25], "indicator dyes" [63], and "probe" [62, 67] are sometimes used as synonyms for an optical sensing material [9].
An oxygen sensing material can consist of one or several fluorophores and a) various kinds of additives, including plasticizers used to improve the efficiency of quenching by oxygen; b) optical isolations used to reduce or eliminate the interference of ambient light; and c) scattering particles used to produce more homogeneous excitation and emission light. The first generation of optical oxygen sensing materials made use of fluorophores, such as pyrene [68], which is characterized by a relatively low fluorescence lifetime, typically less than 100 nm and, thus, resulting in the low sensitivity of the sensor element employed in an OOS. The second generation of oxygen sensing materials is represented by phosphorent transition metal complexes, such as Ru(II) complexes [69, 70] whose typical lifetime ranges from 1 ns to 1 μs. The third generation of optical oxygen sensing materials uses palladium and platinum metal complexes Pd(II) and Pt(II) [47] whose typical lifetime ranges from 20 μs to 100 μs, or even longer [25].

Despite the fact that both the excitation and emission bands of ruthenium-based complexes are rather broad, which can be viewed as a positive property due to the higher flexibility in the choice of excitatio0n sources, a ruthenium-based oxygen sensing material remains so far one of the most popular materials [42].

The function of the matrix is a solid support which can provide not only the immobilization of oxygen sensing materials in or on the matrix, but also some penetration selectivity for oxygen, while rejecting other substances. The most common methods of immobilizing oxygen sensing materials in a matrix are presented in Fig. 3.6. Molecules of the oxygen sensing material, shown in the figure by blue dots, can be homogeneously distributed in the matrix media (shown with a solid yellow color) (See Fig. 3.6a); or they can be absorbed on the surface of nanoparticles (shown green) which are incorporated into the matrix (See Fig. 3.6b); or they can be homogeneously distributed in micro- or nanoparticles (shown pink) which are incorporated into the matrix (See Fig. 3.6c).

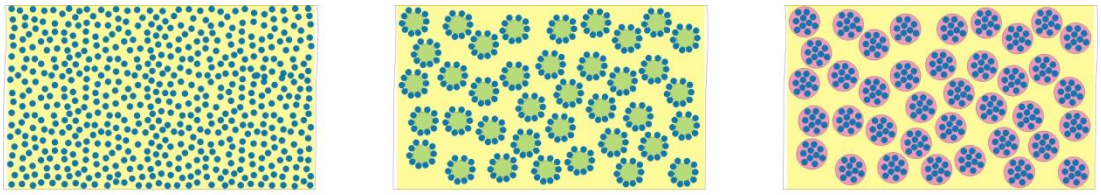

Figure 3.6. Most common methods of immobilizing oxygen sensing materials in a matrix.

OOSs presented in the literature invariably embed oxygen sensing materials in either a polymer [71] or a sol-gel [72, 73] matrix [59]. Many researchers have reported that sol-gel-derived glass is an ideal material for oxygen sensing applications, and sol-gel matrixes have certain advantages over polymer matrixes [72]. In comparison with organic polymers, sol-gel glass has superior optical quality; its mechanical properties provide a chemically inert cage for a large number of organic and inorganic dopants [73, 74] as well as an ability to tailor matrix properties [72]. A properly immobilized oxygen sensing material can be deposited in the form of a viscous solution on a mechanical support such as a thin film of an inert, transparent polymer, fiber, optical filter, light emitting diode (LED), or a photo-detector [27, 58, 75]. A schematic cross-section of a typical planar sensor element is shown in Fig. 3.7 [9, 75].

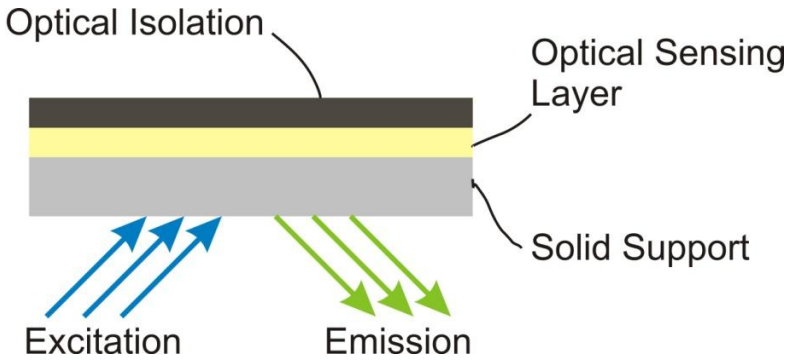

Figure 3.7. Schematic cross-section of a typical planar sensor element.

The sensitivity of a sensor element is defined as the ratio of detected fluorescence intensity I_0 in the absence of oxygen and fluorescence intensity I_{100} in the presence of oxygen [9]:

$$S = {}^{I_0}/_{I_{100}} . \qquad (3.8)$$

Overall, the sensor element with the ratio I_0/I_{100} exceeding 3.0 is a practical oxygen-sensing device [76]. Sensitivity, as well as other properties of a sensor element, depend on a number of factors, especially, on the sensitivity of the oxygen sensing material employed and the oxygen diffusion constant of the matrix [25]. Eq. 3.8 can be used for the rough evaluation of OOS sensitivity. Another method of evaluating the sensitivity of a fluorescence-based sensor is the value $P_{O2}(S=1/2)$ of the partial pressure of oxygen necessary to reduce the initial fluorescence (I_0) of the sensor element by 50% [55, 77]. In a homogeneous medium, where quenching obeys Eq. (2.8), we obtain

$$P_{O_2}(S = 1/2) = {}^{1}/_{K_{SV}} . \qquad (3.9)$$

The sensing ability of an OOS heavily depends on the sensor-element matrix thickness and the diffusion coefficient for oxygen through the matrix. The thicker the sensor element is, the longer the response time of an OOS is [27, 78]. For instance, in order to obtain a polysulfone/Ru(II)-based OOS with response time t_{90}=1 s, the matrix from polymer and fluorophore should be 2 μm thick[78]. The higher is the diffusion coefficient of oxygen, the

higher is the Stern-Volmer constant and, consequently, the higher is sensitivity of OOS. The diffusion coefficient for oxygen through the matrix and, thus the sensitivity of the OOS, can be increased by increasing the matrix porosity [26]. As it is common knowledge that the sensitivity of OOSs increases with an increase of the surface area per unit mass of the matrix medium [59, 79], various other designs for OOSs with enlarged sensing surfaces of matrixes have been proposed.

Among the major factors that influence the response characteristics of OOSs is temperature. However, the temperature dependence of some oxygen sensing material characteristics is nearly unrelated to oxygen concentration, which is a desirable property to perform a simple temperature correction of the OOS's response [57, 75]. The temperature dependence of the Stern-Volmer constant K_{SV} [57] and the lifetime [75] of ruthenium-based oxygen sensing materials have been presented in the literature by empirical calibration curves as the function of temperature. To fit these curves to the experimental data, a second order polynomial is usually applied, e.g.

$$K_{SV} = aT^2 + bT + c \qquad (3.10)$$

where K_{SV} is the Stern-Volmer constant, in atm^{-1}; a, b, and c are correlation coefficients; and T is the temperature on the Kelvin scale.

For some OOSs, the humidity of the gas under test is also an important factor that influences their response by reducing their sensitivity; for others, this influence can be negligible. For sensor elements with the matrix made with platinum octaethylporphyrin (PtOEP) as an oxygen sensing material and ethyl cellulose used as a polymer encapsulating medium, for example, the sensitivity is almost halved at 85% relative humidity (RH) as compared to 0% RH. For sensor elements using silicones, polyvinyl chloride, and polystyrene as a polymer encapsulating medium, humidity is not an important factor in the OOS response characteristics [80].

Illuminators. The type of illuminator used to excite the fluorophore immobilized in the sensor element should be critically considered while designing an OOS. The illuminator needs to emit light in the spectrum compatible with the spectrum of the fluorophore. Moreover, the illuminator should not emit light in the emission spectrum of the fluorophore. If it does, an exciter filter should be installed between the illuminator and the sensor element to permit only selected wavelengths from the illuminator to pass toward the sensor element (See Fig. 3.3). Conventional illuminators used in commercial OOSs are lasers, LD, and LED [25, 32, 49] because they have a relatively narrow spectral bandwidth and may be pulsed and modulated. It is generally recognized that brighter illuminators are preferable for the OOS because a higher excitation light power produces higher fluorescence signals. However, variations in the output of a powerful illuminator are principally responsible for the noise level while measuring these signals. Lock-in amplification is frequently used to minimize such noise [81]. In addition, a high radiant power can result in photo-bleaching of the fluorophore immobilized in the sensor element, which affects the OOS performance.

The bandwidth of LEDs spectra is generally specified in terms of the FWHM. For a typical quasi-monochromatic LED, it varies between 20 and 70 nm, which is similar in size to the excitation bandwidth of many fluorophores; and, for a typical LD, it varies between 2 and 5 nm [82].

***Photo-detectors*.** Photo-detectors are used to convert optical signals carrying the information about the measurand into electrical signals. It is necessary that the spectral response of the photo-detector employed in an OOS be compatible with the emission spectrum of the oxygen sensing material. Besides, the photo-detector's characteristics should satisfy the parameters for which these measurement techniques are employed, e.g., the intensity-based or the lifetime-based technique. According to the literature, the most typically chosen photo-detectors are a photomultiplier tube (PMT) [38, 41, 44, 50, 57, 58, 70], an avalanche photodiode (APD) [44], a spectrometer [54, 56, 59, 74, 76], and a photodiode [27, 46, 52, 66, 83].

PMTs are used in case the emission level is low, and there is a need to guarantee quality light-to-electrical-signal conversion because the PMT provides low dark current, ultimate sensitivity, and produces low noise. However, PMTs are mechanically fragile, susceptible to external magnetic fields, bulky, expensive, and rather demanding as far as a stable high voltage supply is concerned. As for APDs and silicon photodiodes, they are small in size and lightweight, they can easily measure from 10^{-12} to 10^{-3} W of optical power, have reproductive sensitivity, can be rather responsive, with risetimes as fast as 10^{-12} s, and are most practical for a wide range of portable, compact OOSs.

APDs can offer extremely high sensitivity competing with PMTs; however, they have additional noise (avalanche noise) and their sensitivity is dependent on temperature to a greater degree [84]. To keep a constant temperature, some APDs are refrigerated by means of Peltier cells and control closed loops to compensate for temperature variations. However, the use of such devices will raise the APDs cost on be on par with that of PMTs.

The photodiodes are compact, monolithic devices, which are much smaller than PMTs. They are suitable for medium-to-high level measurements because their noise base is typically three orders of magnitude higher than that of PMTs [85]. To detect optical power measured in picowatts, APDs and advanced photodiodes require a pre-amplifier; however, for high optical power levels (less than 10^{-3} W), a simple load resistor configuration can be used [84]. Incorporating additional electronics directly onto a semiconductor sensor chip makes it possible to add additional functions to the sensor. For example, an optical integrated circuit can comprise a photodiode and electronic-signal-processing-circuits [86-88].

As is known from the literature, high sensitive, versatile, and compact spectrometers are rather frequently used in OOSs. These spectrometers, as a rule, have been optimized for low light fluorescence applications, where the ability to detect weak signals is crucial for proper measurements. One of the most popular is a fiber-optic spectrometer USB 2000 from Ocean Optics [89]. The attractive feature of spectrometers used as the photo-detector of an OOS is their ability to measure the fluorescence signal intensity of a particular wavelength. The major limitation of employing spectrometers in portable OOSs is their high cost and risk of their damage.

3.2.3. Optical design configurations.

Once an appropriate sensor element and a measurement technique have been identified, they may be applied in numerous optical design configurations. These are divided into two main categories: *fiber optic sensors*, where optical fibers are used in designing sensing systems, and *non-fiber optic sensors*.

The fiber in fiber optic sensors can be used not only as a passive transmission medium but also as a sensor element. For example, if an oxygen sensing material is applied to the tip of a fiber, this fiber can be used as a sensor element of an OOS. Schematics of two possible connections between an illuminator, a sensor element, and a photo-detector are presented in Fig.

3.8. Various other configurations have been presented in a number of books and review articles [4, 5, 8, 90-96]. Fiber-optic OOSs are superior to other kinds in the market to such an extent that the term the "optical oxygen sensor" in the literature is typically applied only to fiber-optic oxygen sensors (See, e.g., ref. [32]).

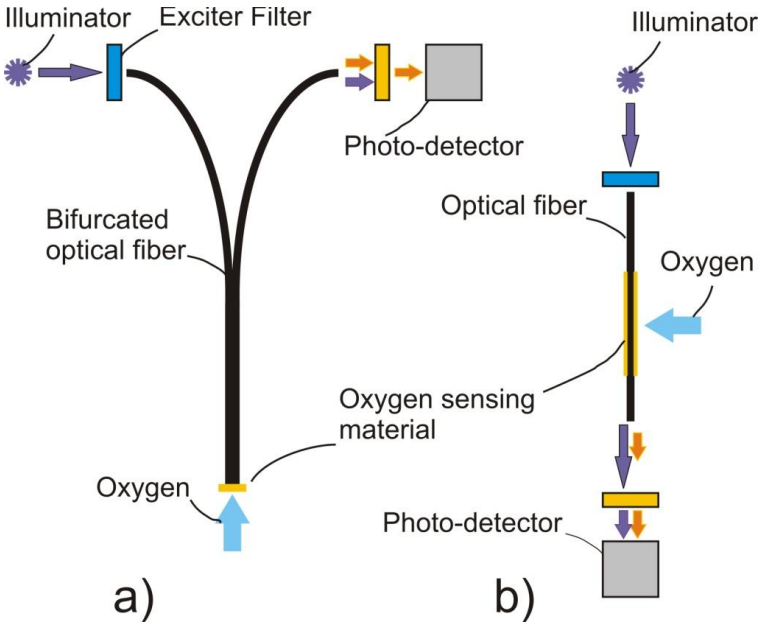

Figure 3.8. Optical design configuration of fiber optic oxygen sensors.

Among the disadvantages of fiber optic sensors, are unavoidable coupling losses between the illuminator and the optical fiber, which results in the need to increase the power consumed by the illuminator in order to provide sufficient excitation power density. Another disadvantage is unavoidable coupling losses between the oxygen sensing material and the optical fiber leading to the attenuation of the fluorescence signal. The amount of oxygen sensing material which can be applied to the tip of an optical fiber is limited because the fiber diameter is generally small. The entire amount of excitation light energy, which can be transmitted along the optic fiber, is also limited because the energy is directly proportional to the cross-section area of the fiber. All of these factors tend to limit the amplitude of the optical signal emitted by the sensing material and transmitted back along the fiber to the proximal end, which results in the need of a high-sensitive and expensive photodiode to register this signal. According to the literature, fiber optic-based OOSs commonly employ high-sensitive photo-detectors such as PMTs [38, 41, 44, 50, 57, 58, 70] and spectrometers [56, 59].

The advantage of non-fiber optic sensors, as compared with fiber optic sensors, is their robust nature, which is an attractive characteristic, when considering the development of practical sensor devices intended for deployment outside a laboratory environment. When producing a sensor element for a non-fiber optic sensor, there is no limitation on the amount of oxygen sensing material which can be applied to a solid support, which normally has a planar surface, (See Fig. 3.7). Two possible options of non-fiber optic design configurations of OOSs are presented in Fig. 3.9. In a double-sided design configuration, the sensor element is located between the illuminator and the photo-detector and, in a single-sided design configuration, the illuminator and photo-detector are located on one side of the sensor element.

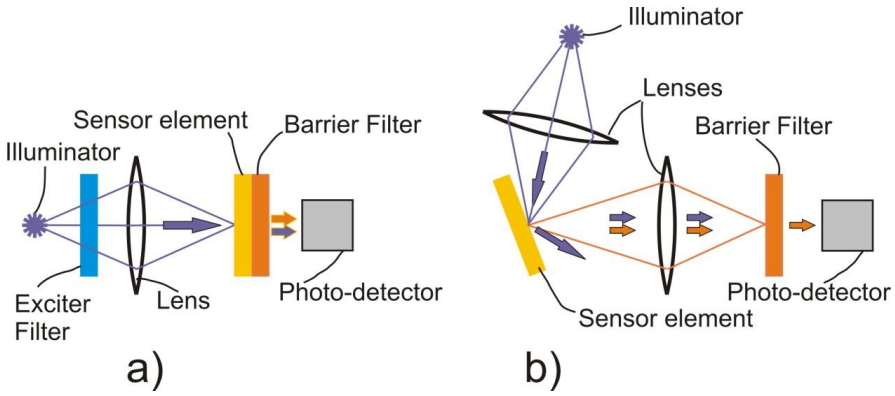

Figure 3.9. Non-fiber optic design configurations: a) double-sided design configuration b) single-sided design configuration.

The double-sided design configuration is more attractive than the single-sided design configuration because it is more compact and allows the designer to decrease the number of the OOS elements. However, the excitation light affects fluorescence signal detection because the photo-detector is located in the optical path of the illumination light beam. The single-sided design configuration has an advantage over the double-sided configuration due to the separation of the excitation light from fluorescence by reflecting the illumination beam aside from the path of fluorescence towards the photo-detector. The angle of incidence of the excitation light is customarily fixed to 45^{o} because it is the optimal angle to minimize the excitation wavelength interference by reducing the reflection of the excitation light back to the probe. Due to the radiation isotopy of fluorescence, the angle of incidence is not critical because the system loses only 0.29 dB if the angle is 45^{o}, as compared to the case where the angle is around 0^{o}[97].

The OOS based on a planar waveguide sensor, which represents a relatively recent innovation in the field of optical chemical sensing, can also use several design configurations (See Fig. 3.10) [5, 98]. The planar waveguide sensor comprises a plastic, a glass, or a silicon substrate, which can act as a planar waveguide. The waveguide can also be deposited on the substrate as an additional layer. An oxygen sensing material layer is deposited onto the waveguide to which the excitation light is coupled, using one of a variety of techniques such as prism coupling, grating coupling, or end-fire coupling. The evanescent field of the guided excitation light extends into the oxygen sensing material layer and excites the immobilized in this material fluorophores located within a distance of typically 100-200 nm from the waveguide surface (See Fig. 3.10a). Another configuration, shown in Fig. 3.10b, enables the direct excitation of the layer of the oxygen sensing material, either above this layer or below the substrate.

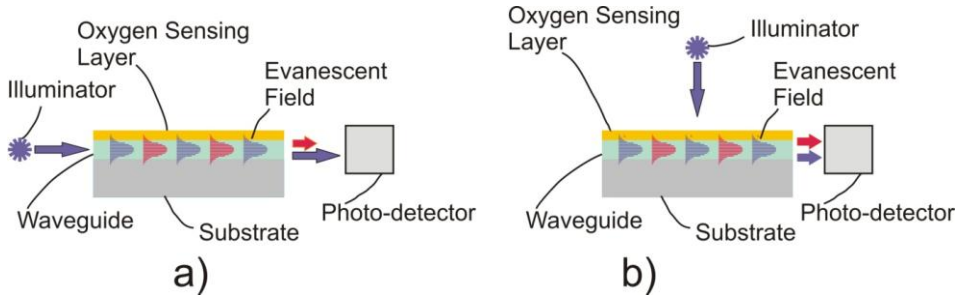

Figure 3.10. Schematic of a planar waveguide sensor element cross-section.

3.3. Selection of a Measurement Technique and Components of the OOS

3.3.1. Measurement technique. Owing to the specifications of the OSS under design, we were to avoid the use of costly and sophisticated instrumentation. Therefore, employing the technique based on the direct measurement of the fluorescence lifetime was not appropriate. The instrumentation employing the intensity-based technique is less complex and less expensive than instrumentation employing a phase shift. However, the intensity-based technique has a major disadvantage as regards to source intensity, the state of optical devices, and photo-detector sensitivity fluctuations. The literature provides us with several methods to cope with the disadvantage. As for the major disadvantage of the lifetime-based technique, it is the calibration curve generation problem. According to the literature, despite the efforts to simplify the generation of calibration curves for lifetime-based measurements, fitting intensity data is much easier than fitting lifetime data.

We have preferred the intensity-based technique over others because it does not limit us in the selection of the appropriate sensor element and can potentially outperform the phase-shift-based technique due to the use of a proper correction algorithm or ratiometric methods, which can be implemented easier than in the case of using the phase-shift-based technique.

3.3.2. Sensor element. The literature testifies to the large number of oxygen sensing materials and various home-style fabrication technologies for manufacturing sensor elements (See Section 3.3.2). As the production of a sufficient batch of reproducible sensor elements in a laboratory environment is questionable, we did not try to implement a technology that can result in the best characteristics of the sensor element for our OOS. Instead, we decided to select a sensor element that has characteristics proven in the market. Although well-known manufactures [9] of OOSs produce sensor elements with rather attractive characteristics, they can sell only a limited number of their sensor elements which is enough only for scientific research. The only producer that offers the unlimited number of their sensor elements, known as RedEye, is Ocean Optics, Inc. (www.oceanoptics.com) [99].

According to its specifications, the RedEye is a ruthenium complex entrapped in a sol-gel matrix and effectively immobilized and protected from water and supplied as patches of 4, 8, or 25 mm (See Fig. 3.11). Due to its relatively long lifetime τ~5 μs, it ensures high oxygen sensitivity as quantified in the Stern-Volmer constant in Eq. 2.8, providing the possibility for measuring oxygen concentration in gaseous phase in the range of 0-100% with the response time less than 1 sec, the minimal 0.1% detectable level, and the 5% accuracy of reading. The exact location of absorption and emission peaks vary but, due to the large quantum yield of ruthenium complexes (Φ=0.38) and a large Stokes shift ($\Delta\lambda$=30 nm), we can use a readily available and inexpensive 400-550 nm blue LED as the excitation source, and an inexpensive barrier filter to separate the 600-615 nm fluorescence light from the excitation light (See Fig. 3.12). Comprehensive investigations carried out in order to establish the optimal film-processing parameters of the ruthenium complex, which has been entrapped in a porous sol-gel film, demonstrated that there is good reproducibility both within a batch and from batch to batch of films [72].

Figure 3.11. RedEye patches, 8 mm and 25mm in diameter.

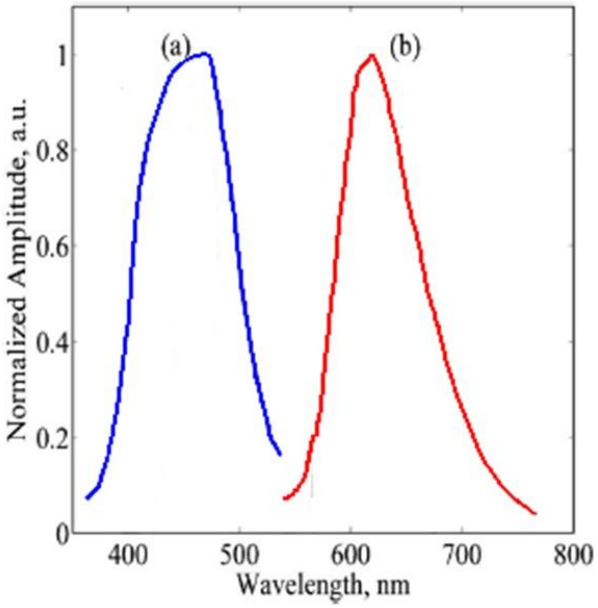

Figure 3.12. Absorption (a) and emission (b) spectra of a ruthenium complex.

3.3.3. Illuminator. Traditional fluorometry employs intensive broad-spectrum illuminators such as Xenon or Halogen arc lamps. However, broad-spectrum illuminators are energy inefficient due to the fact that merely a small percentage of the generated light is useful in any particular application. Fig. 3.12 demonstrates that, to excite the RedEye, we need an energy efficient illuminator emitting light in the narrow wavelength band of 400-500 nm. According to the literature (See Section 3.3.3), both LEDs and LDs satisfy these requirements. LDs provide a higher optical power density than LEDs do and are preferably employed to excite a substance with a low fluorescence quantum yield. For our sensor, however, we have selected LEDs over LDs because the latter type is more expensive, and we do not require their high power density, as the quantum yield of ruthenium complexes is high enough – strong fluorescence is being observed when the RedEye is illuminated even with a low power (under 0.5W) LED.

The primary consideration in selecting a particular LED for our oxygen sensor is the distribution of the LED emission spectrum in relation to the absorption spectrum of the RedEye.

LEDs produce wavelengths of a defined bandwidth of around 30 nm. In our setup, we used low power LEDs: L200CUV405-8D Ultra Violet LED (0.12 W, 405 nm), LED435-03 (20 mW, 440 nm), RL5-P0345 Pink LED (20 mW 440 nm), and LD CN5M Deep Blue LED (under 0.45 W, 453 nm). Figures 3.12 and 3.13 demonstrate the ideal distribution of the spectrum of the Deep Blue LED in relation to the absorption spectrum of the RedEye. The typical forward voltage of these LEDs is about 3.5V.

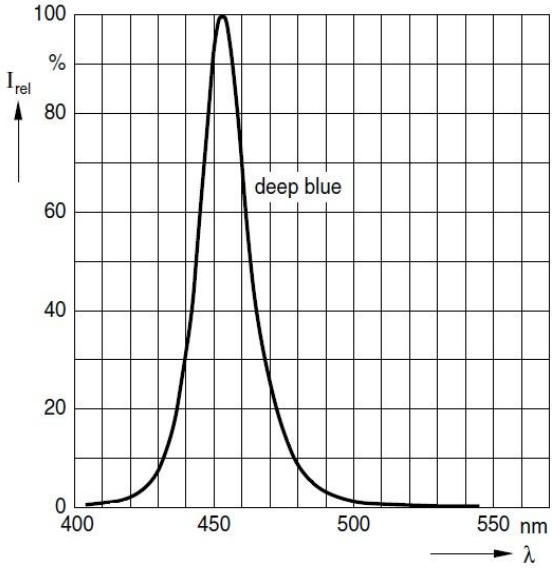

Figure 3.13. Relative spectral emission of the Deep Blue LED [100].

Having obtained a linear approximation of the curve representing relative luminous intensity Φ(i)/Φ(20 mA) of the Deep Blue LED, we presented this approximation in the form:

$$\Phi(i)\Big/_{\Phi(15\ mA)} = 0.075i + 0.25. \qquad (3.11)$$

The LED's lifetime is measured in tens of thousands of hours. Taking into account the fact that an oxygen sensor needs to be turned on merely for the time needed to excite the RedEye, the LED's effective lifetime can be considered practically indefinite.

3.3.4. Photo-detector. A vast assortment of photo-detector types is presented in the market. The primary consideration in selecting a photo-detector is the distribution of its spectral response in relation to the RedEye emission spectrum, as well as the photo-detector's sensitivity, size, cost, and energy consumption. Although such photo-detectors as PMTs and APDs provide extremely high sensitivity, we did not consider their use in our OOS design because of their relatively high cost and large size. In the current market such sensors as photo-resistors, photodiodes, and phototransistors are available approximately at the same price and their characteristics are very similar; for that reason, we selected the most popular photo-detector in the market.

In our setup, we used a programmable light-to-frequency converter TSL230 and a light-to-frequency converter TSL235. Figures 3.11 and 3.14 demonstrate that the emission spectrum of

RedEye coincides with the spectral response of the afore-mentioned devices. Employing for our setup the TSL230 or the TSL235 allowed us to use the same power supply for both the illuminator and the photo-detector because the nominal supply voltage of each of the TSL230 and TSL235 is equal to the typical forward voltage of an LED employed as an illuminator. Electronic-signal-processing circuits incorporated into these semiconductor sensor chips provide effective noise suppression.

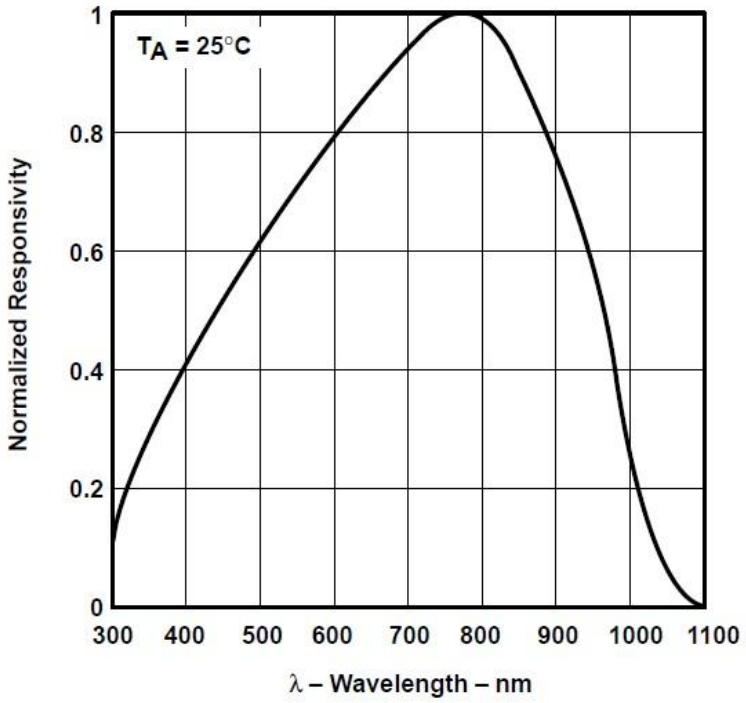

Figure 3.14. Spectral responsivity of TSL230 and TSL235 [86-88].

3.3.5. Optical filters. A number of companies are offering a full range of precision short-pass edge filters, used to transmit wavelengths shorter than the cut-off wavelength of the filter, long-pass edge filters, designed to transmit wavelengths greater than the cut-on wavelength of the filter, cut-off**,** and band-pass filters, used to selectively transmit a portion of the spectrum while rejecting all other wavelengths. Short-pass edge filters can be used as exciter filters, and long-pass edge filters – as barrier filters. These filters have almost ideal transmission characteristics, i.e., the filter is able to pass more than 90% of the light of its pass-band and attenuate the light of its stop-band almost completely. Fig. 3.15 illustrates the transmission characteristic of Long-Pass Glass Color Filter OG 515 from Edmund Optics Filter Kits (VIS Kit), which we used in our preliminary experiments. Unfortunately, the employment of these filters in the oxygen sensor may increase the price of the oxygen sensor and limit the possibilities of decreasing its size.

In Fig. 3.16 is presented the transmission characteristic of Roscolux Color Filter #22 (Deep Amber) employed in our sensor. The transmission characteristic of Edmund Optics Filters exceeds to a great degree that of Roscolux Color Filters because the former have a large transition region, i.e. a large distance between stop-band and pass-band wavelengths. In addition, the transmission coefficient of Roscolux Color Filter #22 is lower in its pass-band and higher in

its stop-band. However, Roscolux Color Filters are rather inexpensive, and are supplied as sheets of thin but stiff plastic film which can be cut into any desirable size.

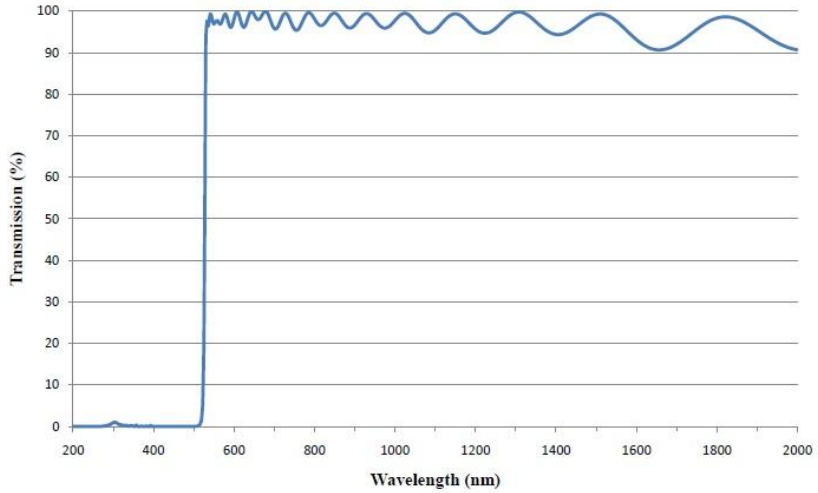

Figure 3.15. Transmission characteristic of Edmund Optics Long-Pass Glass Color Filter OG 515.

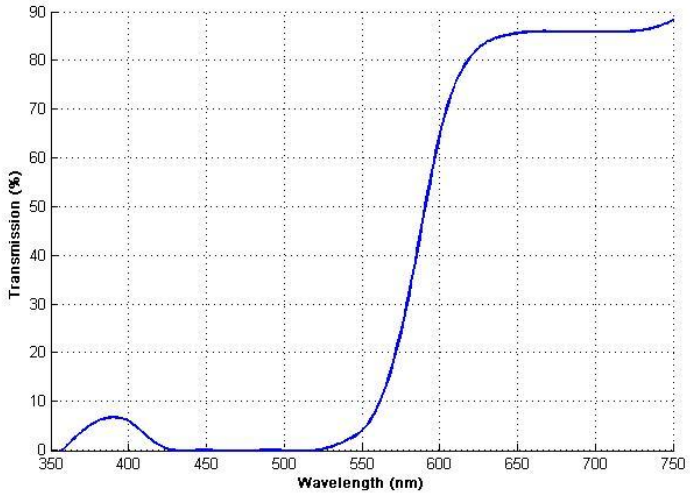

Figure 3.16. Transmission characteristic of Roscolux Color Filter #22.

3.3.6. Optical design configuration. We did not consider the optical design configuration based on the planar waveguide sensor because our selection of the RedEye, to be used as a sensor element, makes it possible to use either the fiber optic or the non-fiber optic design configuration presented in Section 3.3.5. Considering that non-fiber optic design configuration allows us to use an inexpensive photodiode or integrated circuits comprising a photodiode such as TSL230 and TSL235 (See section 3.4.3), we have selected this design configuration over fiber optic design configuration.

Owing to this configuration, we can increase the amount of fluorescence reaching the photo-detector and reduce the amount of background excitation stray light, which will help compensate

for the photodiode's lower sensitivity, as compared to such photo-detectors as a PMT or a spectrometer. We can also decrease the operational current passing through the LED, thus increasing the battery life and preventing photo-bleaching.

Two possible options of non-fiber optic design configurations considered for our OOS are presented in Fig. 3.17. Both these configurations have their benefits and drawbacks suggesting that both these configurations should be optimized and tested. The optimization of the optical design configuration increases the fluorescence collection and, therefore, improves the response of the OOS providing a wider dynamic range and a lower limit of detection.

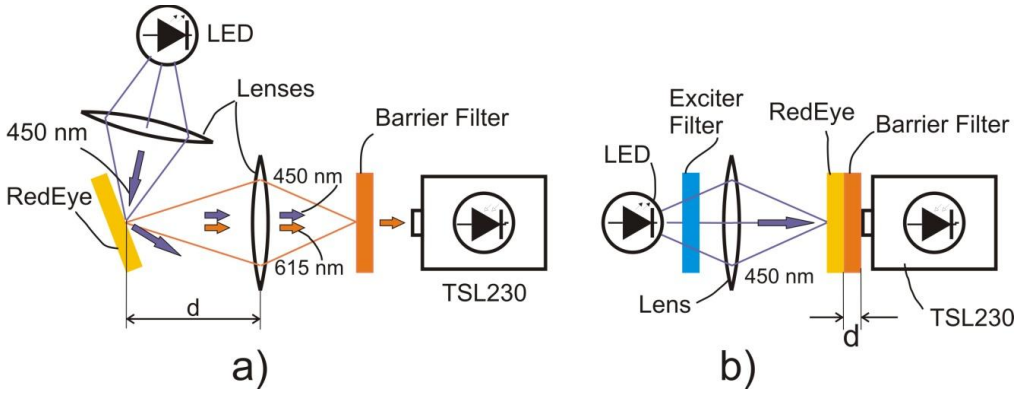

Figure 3.17. Non-fiber optic design configurations: a) single-sided design configuration b) double-sided design configuration.

Fig. 3.17 demonstrates that the distance *d* between the sensor element and the collecting lens is a critical parameter affecting the fluorescence collection efficiency. A single-sided configuration allows us to increase the amount of emitted fluorescence by increasing the illuminated area on the surface of the sensor element. To collect the maximum amount of fluorescence emitted from a large illuminated area, the distance *d* should be as small as possible. However, if the distance *d* is small, the excitation light reflected from the sensor element can pass through the lens and be directed to the photo-detector. Alternatively, a double-sided design configuration allows us to focus excitation light on such a small area as that of the photodiode area (1.36 mm^2 of the TSL230 photodiode) and collect almost all emitted fluorescence without using a collecting lens due to a decrease in the distance *d* by locating the photo-detector back-to-back with the barrier filter, as it is shown in Fig. 3.17b. An increase of fluorescence intensity due to the increase of power density of excitation light, when the light is focused, can compensate for the decrease of the amount of fluorescence caused by the decrease of the size of the illuminated area. Also, the employment of a lens makes the design more complex and difficult to miniaturize, and a high radiant power can result in photo-bleaching.

Since both of the above mentioned design configurations have their pros and cons, we decided that we would select the desired configuration only after our experiments, which would reveal additional advantages of either of the configurations.

3.4. OOS Based on a Single-Sided Design Configuration

3.4.1. Optimization of the single-sided design configuration. We used a trade-off approach with a view to finding the optimal incident angle of the LED-emitted blue light beam. The intensity of emitted and reflected light was measured with a spectrometer [89]. To increase the intensity of fluorescence emitted by the RedEye, we need to increase the power density of excitation light by decreasing its incident angle. However, in this case, the angle of reflection decreases too, and the reflected light affects the photodiode area. To decrease the effect of the excitation light, we need to increase the distance *d* between the RedEye and the TSL230, which leads, however, to a decrease in the amount of fluorescence reaching the photodiode area. Figures 3.18a and 3.18b demonstrate that the increase of the incident angle allows us to decrease the distance *d* and increase the ratio of the fluorescence emitted by the RedEye that reaches the photodiode area to the fluorescence lost. However, in this case, the illuminated spot on the surface of the RedEye increases, while the power density of excitation light decreases, which results in the decrease of fluorescence intensity. Besides, the amount of fluorescence that reaches the photodiode area can also decrease because the incident angle of fluorescence emitted by the periphery of the illuminated spot increases to such a degree that the fluorescence emitted by the periphery becomes reflected from the photodiode area.

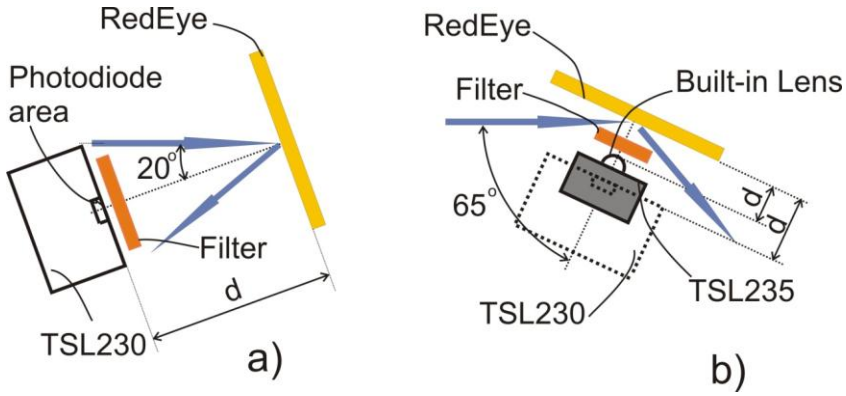

Figure 3.18. Optimization of the single-sided design configuration.

The above-mentioned is also true if fluorescence is being collected with the collecting lens. In this case, the minimum distance *d* between the RedEye and the lens with the diameter *D* is equal to $d_{min}=D/(2\cdot sin\alpha)$, where α is the incident angle of the excitation light. Because of the large size of the TSL230 (8.26 mm x 10.92 mm x 5.08 mm) or the large size of the collecting lens, such a trade-off cannot be achieved: the insufficient amount of fluorescence is not enough to obtain an acceptable dynamic range of the device. The optimal incident angle (65^o) becomes possible with the use of a light-to-frequency converter TSL235 with a built-in lens [88], whose size is as small as 4.8 mm x 4.85 mm x 2.74 mm. Due to the built-in lens, fluorescence emitted from the periphery of the illuminated spot is not reflected from the photodiode area, i.e., it is not lost when the size of the illuminated area increases and the distance *d* decreases. The distance *d* between the TSL235 and the RedEye can be decreased not only due to the small size of the TSL235 as compared to that of the TSL230, but also due to replacing the glass barrier filter used in our initial prototype with the color gel Roscolux Color Filter #22 (F22), which is a thin sheet of polycarbonate.

The optimized single-sided design configuration is presented in Fig. 3.19. Using the photodiode with a built-in lens and an additional element which is a foil shield protection with a small-sized diagram allowed us to exclude from the configuration the focusing and collecting lenses. Because the diaphragm effectively prevents the stray excitation light from reaching the photodiode, the photodiode and the barrier filter are located close to the RedEye. The LED can also be located in close proximity of the photodiode. Due to decreasing the distance *d* between the RedEye and the photodiode, the amount of fluorescence reaching the photodiode increases to such an extent that we can obtain an acceptable dynamic range of the device.

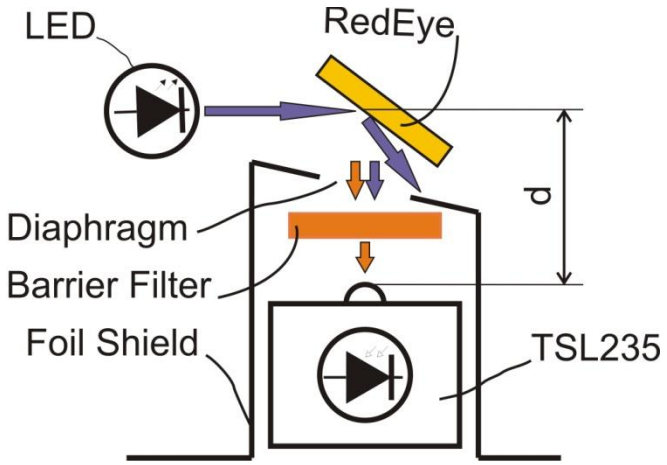

Figure 3.19. Optimized single-sided design configuration.

3.4.2. Prototype of OOS based on a single-sided design configuration. The prototype of our OOS based on the single-sized design configuration is presented in Fig. 3.20. The parts of the OOS casing are made of acrylic sheets. To change the barrier filter characteristics, we can replace, through a narrow slot, the barrier filter F22 (a red strip of polycarbonate) either with other filters from a set of gel Roscolux Color Filters or with combinations of these filters. The RedEye patch can be replaced with another patch through the same slot. Another slot allows us to replace the photo-detector: the Light-to-Frequency Converter TSL235 with the Light-to-Voltage Converter TSL250. The LED used as an illuminator is soldered to the connector and needs tools for its replacement. The prototype is installed in the C-Mount Cube (See Edmund Optics C-Mount Cube Accessories) provided with two handcrafted male hose nozzles used to connect the Cube to a gas distribution system, containing compressed oxygen and nitrogen gas cylinders. Two unused openings of the cube are covered with its protective covers.

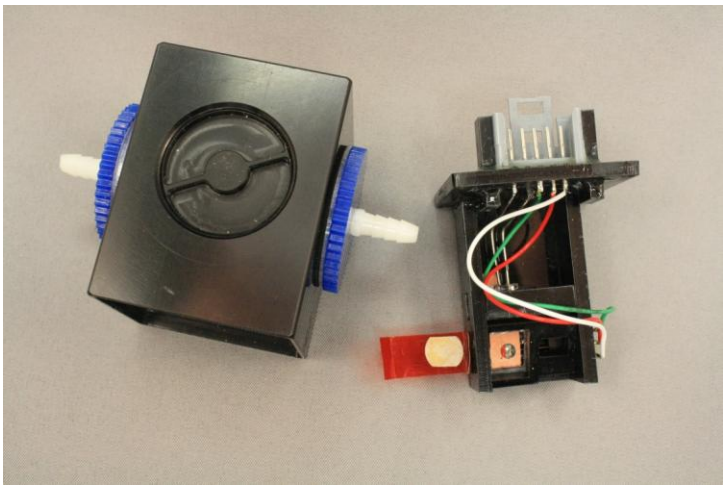

Figure 3.20. Prototype of the OOS based on a single-sided design configuration.

3.4.3. Testing of OOS based on a single-sided design configuration. Our experimental setup for testing the OOS based on a single-sided design configuration is shown in Fig. 3.21. A Tektronix Laboratory DC Power Supply PS280 was used to power the photo-detector and the 120 mW L200CUV405-8D Ultra Violet LED with the 405 nm wavelength at the peak emission (or the LD CN5M Deep Blue LED 0.5 W with the 453 nm wavelength at the peak emission). The 5V fixed output of the Power Supply provided the nominal supply voltage for the photo-detector TSL235 (or, optionally, the TSL250). One of the two adjustable outputs of the power supply was used to set the LED current which was measured by the Digital Multimeter DT9205A. The photo-detector was connected to the Agilent Frequency Counter 53131A and to the Tektronix Digital Storage Oscilloscope TDS2022 to measure the TSL235 frequency output or the TSL250 voltage output. One of the C-Mount Cube's nozzles was open and the other could be connected either to the Air Pump E114229, or to the Respironic UltraFill Cylinder (Tri-Med, Inc), or to the Disposable Helium Tank (balloons from 'Party City').

In our measurements, we used only three reference points of oxygen concentration in the enclosed area with the OOS: the first point was the 20.9% concentration of the air volume, the second and the third points were 100% and 0% of the volume, respectively. Having connected one of the C-Mount Cube's nozzles either to the air pump, or the cylinder with oxygen, or the helium tank, and having left the other nozzle open, we set these concentrations by sweeping the Cube with either air, or oxygen, or helium. All the experiments have been carried out at regular atmospheric pressure and at room temperature of 20^{o}C (68^{o}F).

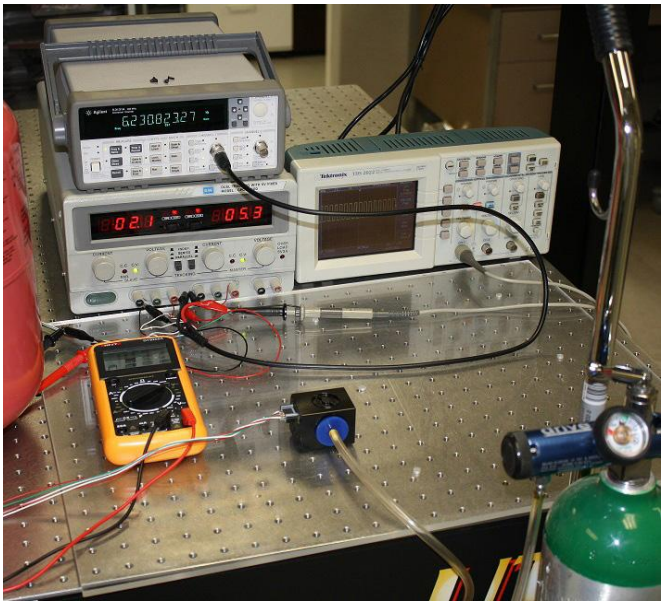

Figure 3.21. Experimental setup for testing the OOS based on a single-sided design configuration.

The first series of experiments was carried out in order to estimate such basic characteristics of the sensor as dark count and the signal-to-background-noise ratio (SNR). Oxygen concentration was equal to 20.9% of the air volume (normal air conditions), and the current flowing through the LED was set at 15 mA. The results of our preliminary experiments showed that the fluorescence intensity provided by the 25 mm RedEye patch was 3.75 times higher than that provided by the 8 mm RedEye patch. Thus, for the single-sided design configuration, we selected the 25 mm RedEye patch over the 8 mm patch.

The preliminary test results of the sensor are presented in Table 3.1. In a number of experiments, we replaced the RedEye with a white paper sheet (Paper) identical in size to the RedEye, or replaced the F22 with foil (Foil). The minus sign ("-"), next to the element in Table 3.1, means that the element was inactive, i.e., either the LED was OFF or the F22, the RedEye, Paper, or Foil were uninstalled. And conversely, the plus sign ("+"), next to the element, means the element was active, i.e., either the LED was ON or the F22, the RedEye, or Paper were installed. To distinguish these experiment results from the results, where we used two filters, we marked the element "F22" with two plus signs "++".

Experiment #1 demonstrates that if the LED is off, the dark count of our device is almost zero (the TSL235 output is f_1=0.5 Hz) and, therefore, the influence of ambient light can be neglected. If the LED is on, the output of the TSL235 increases to f_2=568 Hz (See Experiment #2), which indicates that the shield's efficiency from using foil is not faultless, and the LED-emitted stray blue light penetrates through the diaphragm. However, if the diaphragm is closed with Foil, the TSL235 output is equal to zero (f_{11}=0 Hz), even if the LED is ON (See Experiment #11). Therefore, the TSL235 is sensitive to the light passing through the diaphragm alone.

Table 3.1

Testing the OOS Based on a Single-Sided Design Configuration

Experiment #	LED	Filter #22	RedEye	Paper	Foil	Frequency, Hz
1	-	-	-	-	-	0.5
2	+	-	-	-	-	568
3	+	+	-	-	-	38
4	+	-	-	+	-	44740
5	+	+	-	+	-	3160
6	+	-	+	-	-	19430
7	+	+	+	-	-	8640
8	+	++	-	+	-	792
9	+	++	-	-	-	7
10	+	++	+	-	-	5860
11	+	-	-	-	+	0

We performed an analysis of the testing results under the assumption that the LED emits the blue light of around a 405 nm narrow wavelength band, and the RedEye emits the fluorescence light of around a 615 nm narrow wavelength band. According to the datasheet of TSL235, its output is proportional to irradiance, i.e.

$$f = k \cdot E \qquad (3.12)$$

where f is the TSL235 output, in Hz; E is irradiance, in W/cm2; and k is the proportionality constant.

From Experiments #2 and #3, we can evaluate the transmission coefficient of F22 T_{405} as the ratio of irradiances E_2 and E_3 before and behind F22: $E_2=f_2/k=568/k$, $E_3=f_3/k=38/k$, and $T_{405}=E_3/E_2= f_3/f_2=38/568=0.067$, or 6.7%. This value, along with the values of T_{405} calculated using measurement results obtained in our other experiments, exceeds the value given by the F22 specifications (T_{405}=5.0%). Moreover, calculations based on measurements involving two F22 give us unexpectedly large T_{405} values. Our assumption that the LED-emitted light is a narrow wavelength band of around 405 nm has not been validated.

Our next assumption was that the LED peak emission is accompanied by a certain tail. In addition to the relatively narrow peak of 405 nm, the LED also has a tail – the light emitted in the wavelength range of above 600 nm which cannot be suppressed by the F22 because the transition coefficient for this wavelength range T_{615} is about 71%. Therefore, the measurement results of irradiance E_2 behind F22 and the calculated value of $T_{405}=E_3/E_2$, in effect, are greater than those obtained in the case of the absence of the tail. A large error is especially noticeable when additional filters F22 are involved, because the blue light might have already been suppressed by the first set of F22s due to small value of the transmission coefficient T_{405}=0.05 and, therefore, an additional F22 does not decrease the absolute value of this suppressed light power, as it does not affect the tail due to the high value T_{615}=0.71. In this manner, our

hypothesis helped explain why the T_{405} values calculated above are larger than the value from the F22 specifications.

According to our assumption, the LED light of irradiance E_{LEDi} (i=2, 3, …, 11 is the number of experiment) that passes through the diaphragm consists of the blue light of a narrow wavelength band, whose peak wavelength is 405 nm and irradiance is E_{Pi}, and a tail – the light of a wavelength band, whose peak wavelength is 615 nm and irradiance is E_{Ti}, i.e., $E_{LEDi}=E_{Pi}+E_{Ti}$. Taking into account that $E_{LED2}=E_{LED3}=E_{LED9}$, $E_{LED4}=E_{LED5}=E_{LED8}$, and $E_{LED6}=E_{LED7}=E_{LED10}$, we can evaluate the ratio of values E_{LEDi}, E_{Pi}, E_{Ti}, and E_{Fi} by solving the system of equations that follows from conditions of experiments presented in Table 3.1. For example, the conditions of Experiments #6 and #7, involving the RedEye, give us the following system of equations:

$$E_{P6}+E_{T6}+E_{F6}={}^{f_6}\!/_{k}=19430/k \qquad (3.13)$$

$$0.05E_{P7}+0.71(E_{F7}+E_{T7})={}^{f_7}\!/_{k}=\frac{8640}{k}. \qquad (3.14)$$

Solving this system of equations, we obtain E_{F7}=8588/k and $E_{P7}+E_{T7}$=10841/k. Solving the system of equations related to Experiments #4 and #5, involving paper, we obtain E_{P5}=43342/k and E_{T5}=1356/k or E_{T5}/E_{P5} =0.032. Assuming that E_{Ti}/E_{Pi} =0.032 is true for all experiments, we have E_{P7}=10505/k and E_{T7}=336/k.

Defining the signal-to-background-noise ratio behind one F22 as $SNR_7=0.71E_{F7}/(0.05E_{P7}+0.71E_{T7})$ and behind two F22s as $SNR_{10}=0.71^2E_{F10}/(0.05^2E_{P10}+0.71^2E_{T10})$, we can obtain values SNR_7==6098/(525+239)=8 and SNR_{10}=4329/(19+366)=22.

Our hypothesis about the influence of the tail of the LED emission spectrum on our measurement results has been proven by studying the spectra of the LED-emitted light. The spectra were measured by USB4000 Fiber Optic Spectrometer (Ocean Optics). The light from the LED, attenuated by the Fiber Optic Variable Attenuator FVA-UV (Ocean Optics), was coupled to one connector of the FHS-UV In-Line Filter Holder (Ocean Optics) and the spectrometer was coupled to the other connector. This simple setup allowed us to obtain an undistorted spectrum of LED emission, as well as spectra measured behind the filters inserted into the filter holder. Fig. 3.22 demonstrates the RedEye's fluorescence emission spectrum obtained using Short-Pass Edge Glass Color Filter (with the 500 nm cut-off position) from Edmund Optics Filter Kits (VIS Kit), which was used as an exciter filter. As can be seen from the figure, the precision filter, due to its perfect characteristics, allows us to obtain a strong fluorescence signal with the peak emission at 615 nm, while the excitation light from the LED is completely suppressed.

The LED emission spectrum obtained behind one of F22s inserted in the filter holder and used as a barrier filter is presented in Fig. 3.23. The figure clearly demonstrates the existence of the tail in the wavelength range from 550 nm to 650 nm which overlaps with the wavelength range of the fluorescence emission, affecting thus fluorescence detection because barrier filters are not capable of suppressing the tail effectively. The figure also demonstrates that the F22 does not suppress LED emission completely as it can be done with precision filters (See Fig. 3.15). The transmission coefficient of the F22 increases up to T_{405}=0.05 due to a distinct local extremum located at around 390 nm of the curve, representing the transmission characteristic of this filter (See Fig. 3.16). However, despite this drawback, we preferred to employ the F22 because of its low price and the low thickness of the film, as compared to the price of and the thickness of the film in precision filters.

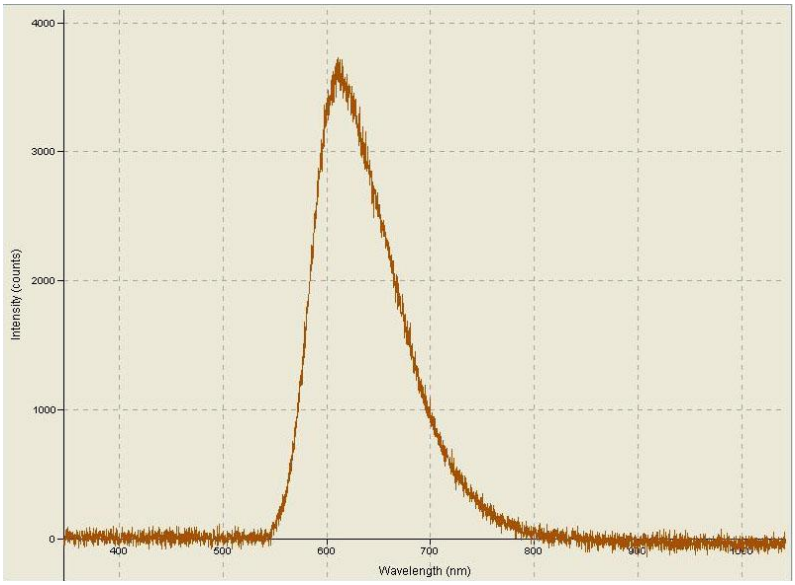

Figure 3.22. Fluorescence emission spectrum of the RedEye.

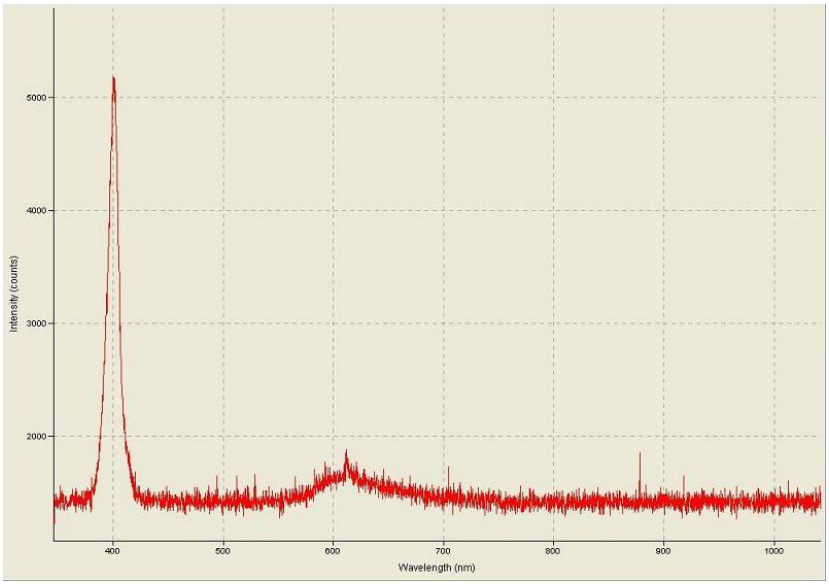

Figure 3.23. LED emission spectrum obtained using one F22.

The response of our sensor to different oxygen concentrations Q is presented in Table 3.2. The 95% confidence interval of four frequency measurements for all reference points was less than $\Delta f(Q)$ =0.03kHz.

Table 3.2

Results of Measuring the Fluorescent Response

Oxygen Concentration, % by volume	0	20.9	100
Frequency *f*, kHz	175	89.5	33.5
$f_0/f-1$	0	0.96	4.22

Bearing in mind that the light intensity value *I* is proportional to the irradiance value *E* measured by the TSL235 and that, according to Eq. (3.12), the irradiance *E* is proportional to the corresponding TSL235 output *f*, we used the function $f_0/f-1$, instead of the function $I_0/I-1$ for the sensor calibration

$$f_0/_f = 1 + K_{SV}Q. \qquad (3.15)$$

The plot illustrating the results of measuring the fluorescent response is shown in Fig. 3.24. The output dependence on oxygen concentration can be approximated by the function $f=30+145\cdot exp(-0.04Q)$. The calibration graph shown in Fig 3.25 was plotted using data from Table 3.2. A linear interpolation with the 95% confidence interval provides us with the Stern-Volmer constant

$$f_0/_f - 1 = 0.042\%^{-1}Q + 0.034 \qquad (3.16)$$

where *Q* is oxygen concentration in % by volume and the constant $0.042\ \%^{-1} = 0.032$ torr^{-1} can be considered as K_{SV}.

The sensor sensitivity evaluated using parameter I_0/I_{100} is $f_0/f_{100}=175/33.5=5.2$**,** and using parameter $P_{O2}(S=1/2)$ is $1/0.032=32$ torr (See Eq. 3.9).

To calculate our sensor's oxygen concentration resolution, we used the equation obtained from Eq. (3.15):

$$\Delta f(Q) = \left(\frac{df}{dQ}\right)\Delta Q \qquad (3.17)$$

where $\Delta f(Q)$ is the measurement uncertainty of frequency when oxygen concentration is *Q*, and ΔQ is the resolution of the corresponding oxygen concentration.

Fig. 3.24 illustrates an increase of value $|df/dQ|$ with a decrease of oxygen concentration *Q* until value $|df/dQ|$ reaches its maximum in the case where oxygen concentration equals zero. According to Eq. (3.17), we obtain the minimal resolution ΔQ when $Q=0\%$. Thus, to calculate the oxygen detection limit, we have to calculate df/dQ at $Q= 0\%$.

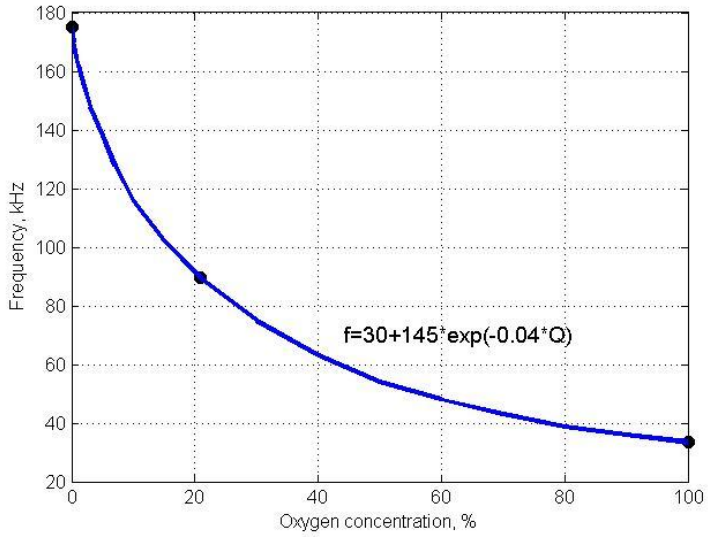

Figure 3.24. Measurement results of the fluorescence response.

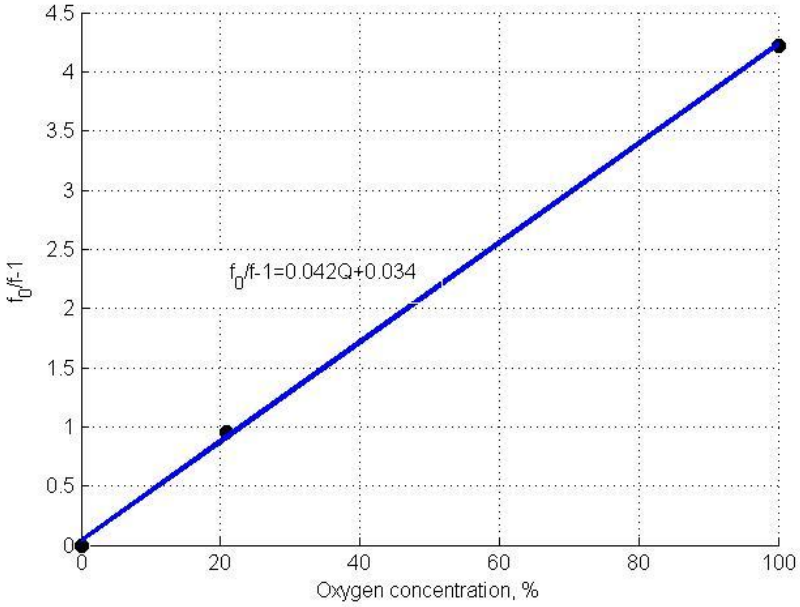

Figure 3.25. Stern-Volmer plot $f_0/f-1$ vs. oxygen concentration.

From Eq. (3.15) we have

$$df/dQ = -K_{SV} f_0 / (1 + K_{SV} Q)^2 \qquad (3.18)$$

and $(df/dQ)_{Q=0}=-K_{SV}f_0$. We obtain the minimum resolution $\Delta Q_{Q=0}$ when oxygen concentration Q=0% by substituting the value $df/dQ)_{Q=0}$ into Eq. (3.17): $\Delta Q_{Q=0}=\Delta f(Q)/(K_{SV}f_0)=$ 0.03/(0.042·175) = 0.0041% or, in terms of the oxygen partial pressure, $\Delta P_{Q2=0}=3.1$ torr. If

oxygen concentration is Q=20.9% $(df/dQ)_{Q=20.9}$=-0.28$K_{SV}f_0$, then resolution $\Delta Q_{Q=20.9}$=0.0144% or $\Delta P_{Q=20.9}$=11 torr.

3.5. OOS Based on a Double-Sided Design Configuration

3.5.1. Optimization of the double-sided design configuration. To study factors affecting the characteristics of our OOS, we developed such experimental setup which allowed us to use various combinations of filters and RedEye patches and compare not only the output of the photodiode these combinations resulted in, but also the spectra of the fluorescence signal. We also developed the MatLab software which allowed us to conduct various numerical experiments necessary for comparing the effectiveness of using different combinations of filters for suppressing unwanted peaks.

Experimental setup and preliminary experiments. The experimental setup for testing our OOS based on a double-sided design configuration is shown in Fig. 3.26. A Tektronix Laboratory DC Power Supply PS280 was used to power a photo-detector and an LED – either L200CUV405-8D Ultra Violet LED (0.12 W, 405 nm), or LED435-03 (20 mW, 440 nm), or RL5-P0345 Pink LED (20 mW 440 nm), or LD CN5M Deep Blue LED (under 0.45 W, 453 nm). The 5 V fixed output of the power supply provided the nominal supply voltage for the photo-diode TSL250. One of the two adjustable outputs of the power supply was used to set the LED current which was measured by the Digital Multimeter DT9205A. The photo-detector was connected to the Tektronix Digital Storage Oscilloscope TDS2022, to measure TSL250 voltage output.

Our design of the OOS allowed us to replace various combinations of RedEye patches, exciter filters and barrier filters by loading them into the filter holder while conducting experiments. The photo-detectors – photodiode TSL250 and USB 4000 Spectrometer – were replaceable as well. A 74-VIS collimating lens (Ocean Optics) could be easily installed instead of the TSL250 to couple fluorescence light into the optical fiber of the spectrometer. All filters were selected from the stock-list of Roscolux Color Filters, including Filter #22 (Deep Amber), further referred to as F22, Filter #359 (Medium Violet), further referred to as F359, and Filter #370 (Italian Blue), further referred to as F370. The schematic of the OOS based on a double-sided design configuration is presented in Fig. 3.27.

The OOS case is provided with only one nozzle which can be connected either to the Air Pump E114229 or to UN1066 type cylinders with compressed oxygen (UN# 1072) and nitrogen (UN# 1066). The gas under test was directed to the bottom of the filter holder and went out through the holder's top. In our measurements, we used three reference points of oxygen concentration: the first point was the 20.9% concentration of the air volume, and the second and the third points were 100% and 0% of the volume. Having connected the hose nozzle either to the air pump, or to cylinders with compressed gases, and having opened the filter holder at its top, we set these concentrations by sweeping the filter holder with either air, or oxygen, or nitrogen. All the experiments were carried out at regular atmospheric pressure and at room temperature 20^{o}C (68^{o}F).

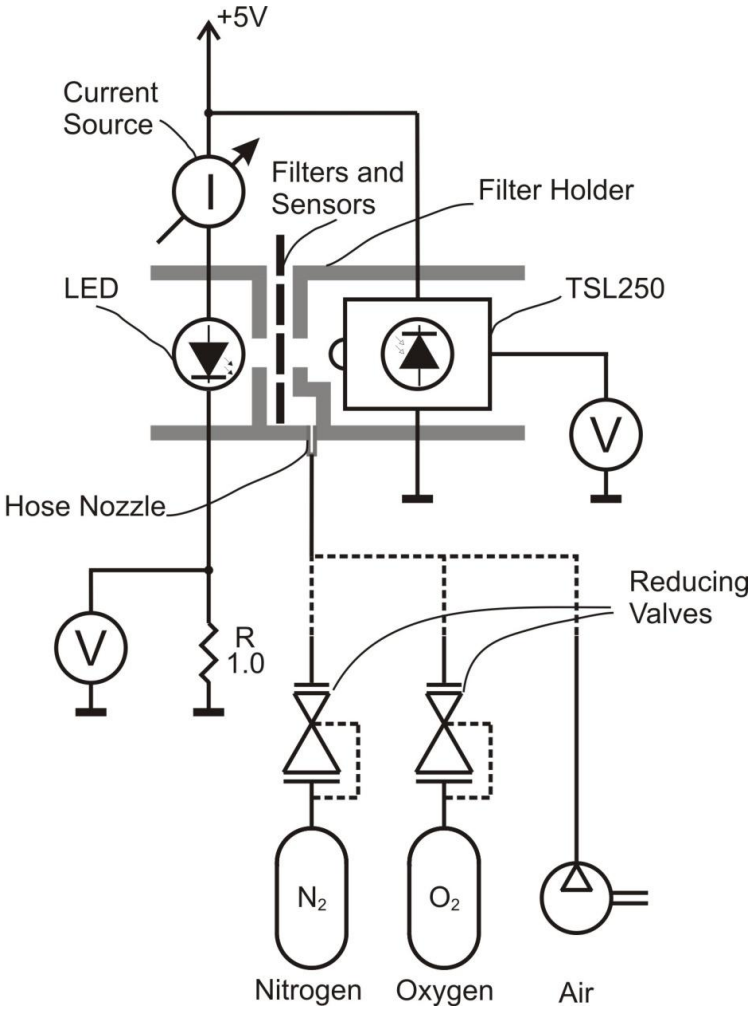

Figure 3.26. Experimental setup for testing the optical oxygen sensor based on a double-sized design configuration.

Taking into account the datasheet, where the TSL250 output V is proportional to irradiance, Eq. (3.15) used to describe the TSL235 performance, can be rewritten for the TSL250 as

$$V_0/V - 1 = K_{SV}Q. \qquad (3.19)$$

The results of our preliminary experiments show that fluorescence intensity measured at the illuminated and reverse sides of an 8 mm diameter RedEye patch is almost the same value, while fluorescent intensity measured on the reverse side of a 25 mm diameter patch is attenuated by 4 times. Thus, for the double-sided design configuration, we need to use the 8-mm-diameter patch.

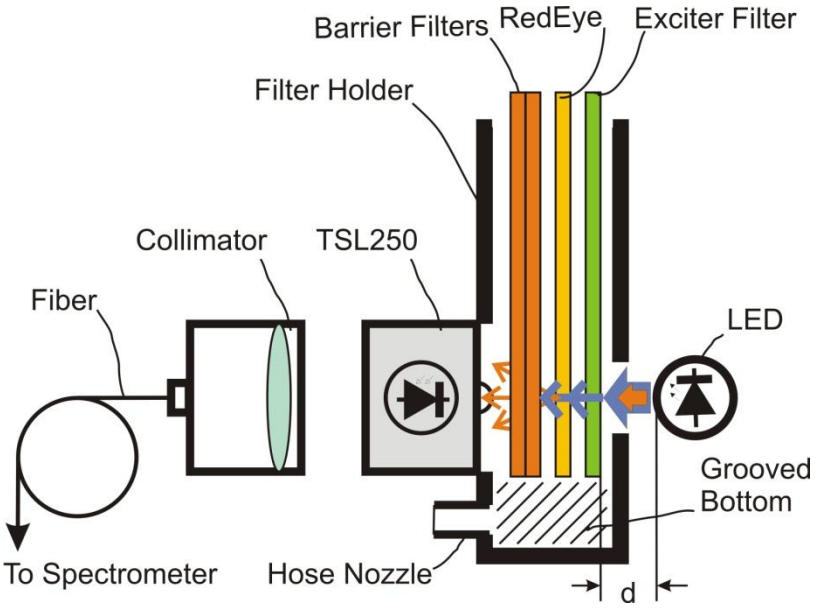

Figure 3.27. Schematic of the OOS based on a double-sided design configuration.

Preliminary experiments allowed us to define the number of barrier filters needed in a sensor based on a double-sided design configuration. Fig. 3.28 demonstrates the efficiency of the suppression of the LED light, depending on the number of barrier filters. We do not succeed in suppressing the 440 nm peak with the first filter (the blue curve). The second filter (the red curve) completely suppresses the 440 nm peak, not being able, however, to handle the 606 nm peak of the LED's tail. Using the third and the fourth filters (the green and the black curves) helps attenuate the LED tail's light by mere 10%, which is by no means effective. Having this in mind, we came to the conclusion that the optimal number of barrier filters is two, and that to suppress the LED's tail, we need to employ an exciter filter.

The second noteworthy result of our preliminary experiments allowed us to increase the sensor sensitivity almost by twice. During preliminary experiments, our attention was attracted to the existence of an optimal relationship between the intensity of excitation light and the thickness of the RedEye patch. In the low power mode, the fluorescence signal linearly increases with LED power and, in the high LED power mode, the fluorescence signal saturates. An increase of the LED power to the value exceeding P_S which corresponds to the end of the unsaturated mode will lead to no effect since the fluorescence signal cannot increase higher than its saturated value, and an excess of excitation power can affect fluorescence detection. Most likely, power P_S is not the optimal power because a thin RedEye patch is capable of absorbing only a small amount of excitation light. Thus, the power of excitation light should be selected considering how effective the absorption of the RedEye is. An increase in the RedEye thickness higher than the optimal thickness S_O will not produce the desired effect either because an increase of fluorescence intensity due to absorption of an additional amount of excitation light cannot compensate for the decrease of fluorescence intensity caused by the increase of the absorption of fluorescence light. Thus, the thickness of a RedEye patch should increase only until the fluorescence signal increases. A further increase in its thickness is not effective. Moreover, a large thickness of the RedEye patch results in slowing the sensor response as oxygen molecules need more time to diffuse into the thick patch. To avoid the increase in the sensor response time, we increased the

RedEye thickness by using a ‘sandwich structure’, assuming that oxygen molecules are capable of penetrating between the patches. However, we did not observe an increase in the OOS sensitivity, using three and more RedEye patches.

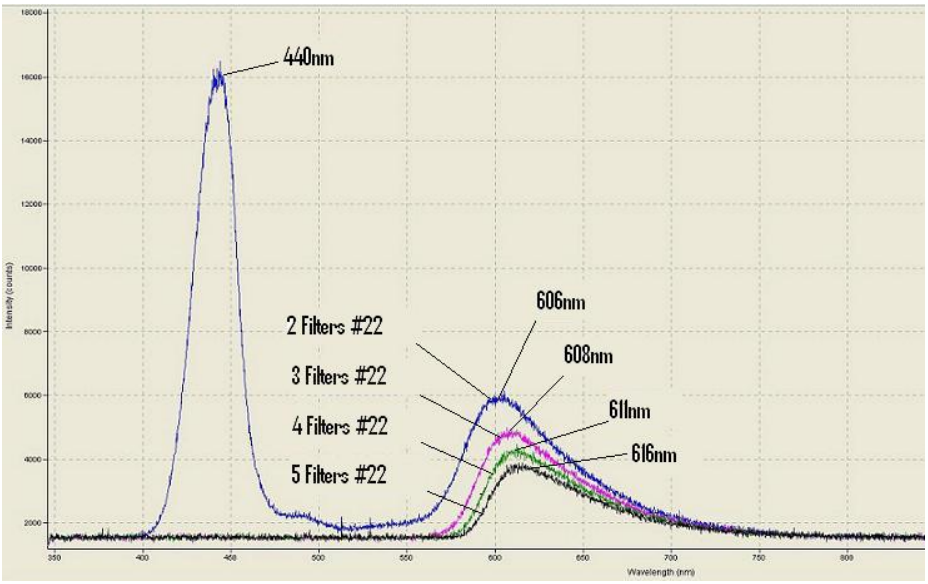

Figure 3.28. Suppression the LED light by increasing the number of barrier filters.

Numerical experiments. The software developed in MatLab allowed us to conduct various numerical experiments necessary for comparing the effectiveness of using different combinations of filters for suppressing unwanted peaks. Comparison of experimental and numerical results has demonstrated that numerical experiments can be considered as preliminary experiments. The results of a series of numerical experiments with the F22 used to suppress the LED light by multiplying the number of these filters is shown in Fig. 3.29. Analyzing the results of numerical experiments shown in Fig. 3.29, we came to the same conclusions that we obtained analyzing experimental results shown in Fig. 3.25. The F22 we employed as a barrier filter because of its advantage in transmission properties (See Fig. 3.15) exceeded properties of all other filters from the large stock-list of Roscolux Color Filters.

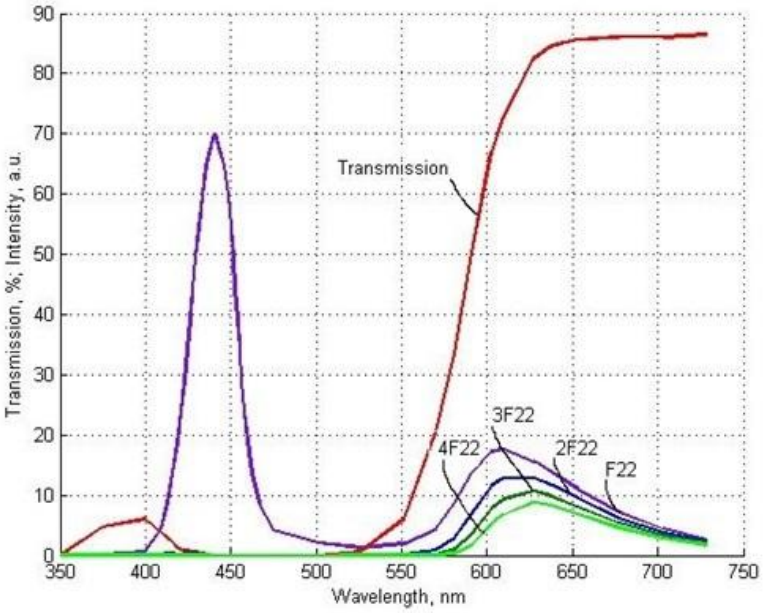

Figure 3.29. Numerical experiments with F22 used to suppress the LED light: F22, 2F22, 3F22, and 4F22 correspond to experiments with 1, 2, 3, and 4 filters, respectively.

The Roscolux Color Filter appropriate to use as an exciter filter has far more complex transmission properties than F22 and, for that reason, it is difficult to select the proper filter without a rather thorough consideration using our MatLab software. Fig. 3.30 demonstrates the comparison of two best suited exciter gel filters selected from the stock-list. Both of the selected filters, F359 (Medium Violet) and F370 (Italian Blue), not only suppress the 615 nm peak related to the tail, but also attenuate the excitation light emitted by the LED, providing 45% transmittance by the F370 and 60% transmittance by the F359. Out of the two, the F370 is preferable over the F359 because the F370 provides less loss of the excitation light.

The same results could be easily obtained by comparing the transmission characteristics of the above-mentioned filters without applying our Matlab software. However, the software allows us to notice that F370 has the advantage which can be proven only numerically or experimentally. Using our MatLab software, we are able to enlarge the graph presented in Fig. 3.30 by changing the scale of axis Y, which allows us to see that the F370 suppresses the LED's tail almost completely, while the F359 passes a certain amount of excitation light in the wavelength region of 650-750 nm (See Fig. 3.31).

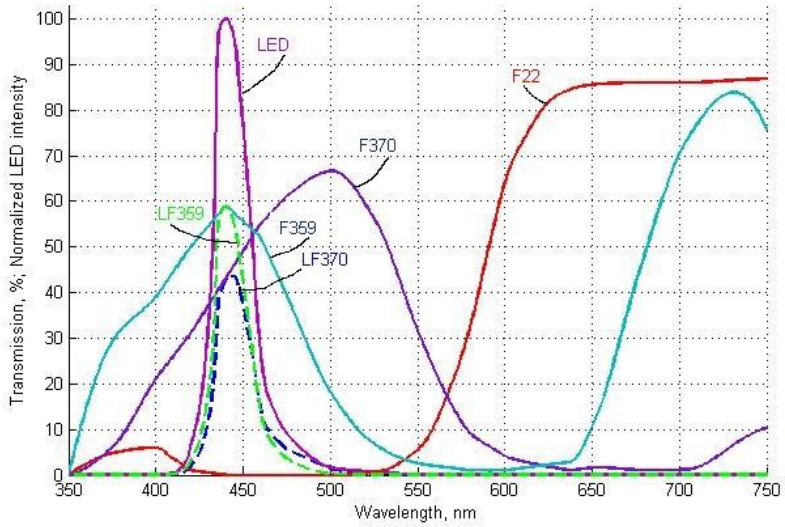

Figure 3.30. Comparison of exciter filters' performance: normalized spectra of excitation light before exciter filters, behind F359, and behind F370 are marked as LED, LF359, and LF370, respectively.

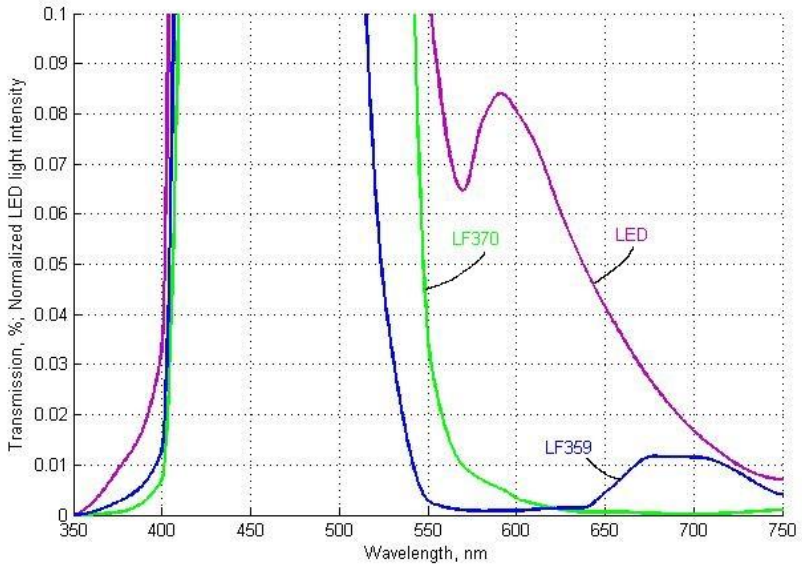

Figure 3.31. Comparison of exciter filters' performance, magnified view: LED, LF359, and LF370 denote normalized spectra of excitation light before exciter filters, behind F359, and behind F370, respectively.

3.5.2. Testing the OOS based on a double-sided design configuration.

Performance of the OOS with different combinations of RedEye patches and filters. During our tests of OOSs based on double-sized design configuration, we used three different types of the 8 mm-diameter RedEye patch (RE-FOX-8, RE-FOS-8, and RE-HI-8 marked as S1, S2, and S3, respectively), two exciter filters, F370 and F359, and a barrier filter F22. We marked the OOSs employing combinations of these elements with sequences of symbols representing

combined elements. For example, the sensor F370S3F22 employs the combination consisting of an exciter filter F370, a RedEye patch S3, and a barrier filter F22. The symbol 'D' (double) was used to denote OOSs employing the combinations comprising two RedEye patches or filters (e.g., the OOS F370DS3DF22 employs two RedEye patches S3 and two barrier filters F22).

Three reference points (100% oxygen; 100% nitrogen or 0% oxygen; and 20.9% oxygen were denoted by symbols 'O_2', 'N_2', and 'A' (air). Gas concentrations of the reference points were achieved after the filter holder was swept by the gas under test for 5 minutes. Measurements of TSL250 output were performed at different values of excitation light power, which was varied by controlling the current flowing through the LED. After setting each point of light power, we had to wait for a few seconds, until the output of the TSL250 stabilized or reached its maximum. In the case of the RedEye sandwich structure, the waiting period, or the exposed time, was approximately two times longer.

The TSL250 output voltage in the experiments with the RedEye patch S2 was far higher than in the case of employing patches S1 and S3, which is why we present only our results of experiments with the RedEye patch S2. The experiment results with a double-sized design configuration of the OOS employing one and two RedEye patches S2 are presented in Fig. 3.32. Linear approximations of the curves *V(i)* presenting the measurement results, linear intervals of the curves *V(i)* calculated for the 0.95 confidence level, and the sensitivity of the sensor with one and two RedEye patches S2 are demonstrated in Table 3.3. To evaluate the sensitivity of the OOS under test, we used the ratio I_0/I_{100}, which is equal to V_0/V_{100}, where V_0 and V_{100} are approximate values of the output of TSL250 in the presence and absence of the oxygen, respectively.

Table 3.3

Linear Approximations of the Curves Representing the Measurement Results, Linear Intervals of the Curves, and Sensitivity of the Sensor with One and Two RedEye Patches S2

Oxygen Sensor	Concentration of O_2, %	Linear approximation, V	Linear interval, mA	Sensitivity, V_0/V_{100}
S2DF22	21 (A)	0.272*i+0.065	0-10	1.97
	0 (N_2)	0.443*i+0.023	0-6	
	100 (O_2)	0.218*i+0.071	0-10	
DS2DF22	21 (A)	0.323*i+0.062	0-8	3.23
	0 (N_2)	0.693*i+0.057	0-5	
	100 (O_2)	0.211*i+0.052	0-10	

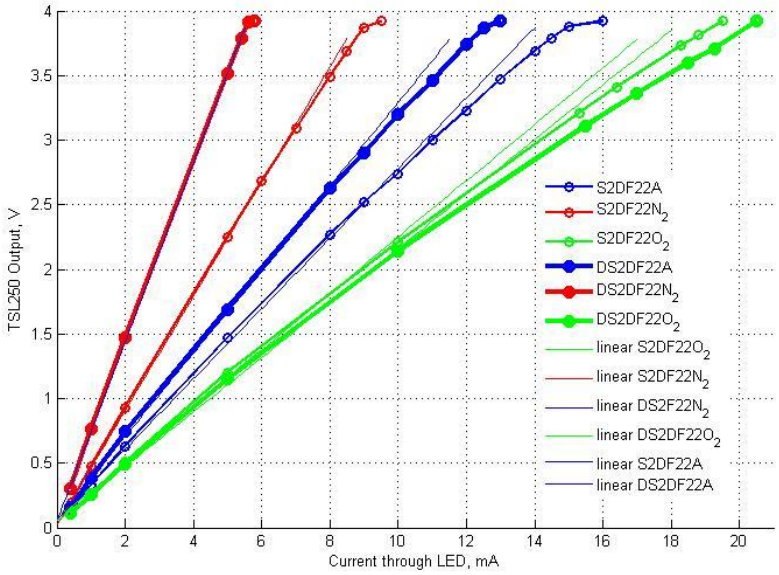

Figure 3.32. Comparison of the performance of oxygen sensors S2DF22 and DS2DF22.

The dependence of the OOS sensitivity in terms of V_0/V_{100} on the current I flowing through the LED is presented in Fig. 3.33, where we demonstrate that employing two RedEye patches, instead of one, can result in increasing the sensor sensitivity from 1.97 to 3.22. Using linear and cubic approximations $V(I)$ of the experimental curves depicted in Fig. 3.32, we also obtained approximating curves $V_0(I)/V_{100}(I)$ of the sensitivity corresponding to these two approximations. From Fig. 3.33, one can notice that the curves obtained using cubic approximations (dashed lines) fit the curves obtained using experimental results (thick solid lines) to a far greater degree than the curves obtained using linear approximations (thin solid lines), especially when the LED current I is less than 2 mA. Nevertheless, we can use the linear approximations $V(I)$ of the experimental curves in case the LED current is greater than 2 mA, as not only the linear approximations curves $V(I)$ themselves fit the experimental curves, but also the approximating curves of the sensitivity $V_0(I)/V_{100}(I)$ fit the curves obtained from experimental data quite satisfactorily. The figure also demonstrates that the operation modes, where the current flowing through the LED is less than 1 mA, are not appropriate because of the quick sensitivity decrease.

The employment of an exciter filter results in decreasing the sensor's background signal corresponding to TSL250 output V_{100} due to depressing the LED's tail. However, at the same time, the exciter filter attenuates excitation light, which results in decreasing the outputs of TSL250 V_0 and V_{100}. The OOS sensitivity V_0/V_{100} benefits from decreasing the value V_{100} and, conversely, suffers from decreasing the value V_0. To choose the oxygen sensor with the best/most precise sensitivity, we conducted experiments with OOSs, employing combinations of one or two RedEye patches S1, S2, and S3, one or two barrier filters F22, and exciter filters F359 or F370. Our experiments were the evidence for the highest sensitivity of sensor DS2DF22. The advantage of sensor DS2DF22 over sensors S2DF22, F359S2DF22, and F370S2DF22 is illustrated with linear approximations of each sensor's sensitivity in Fig. 3.34.

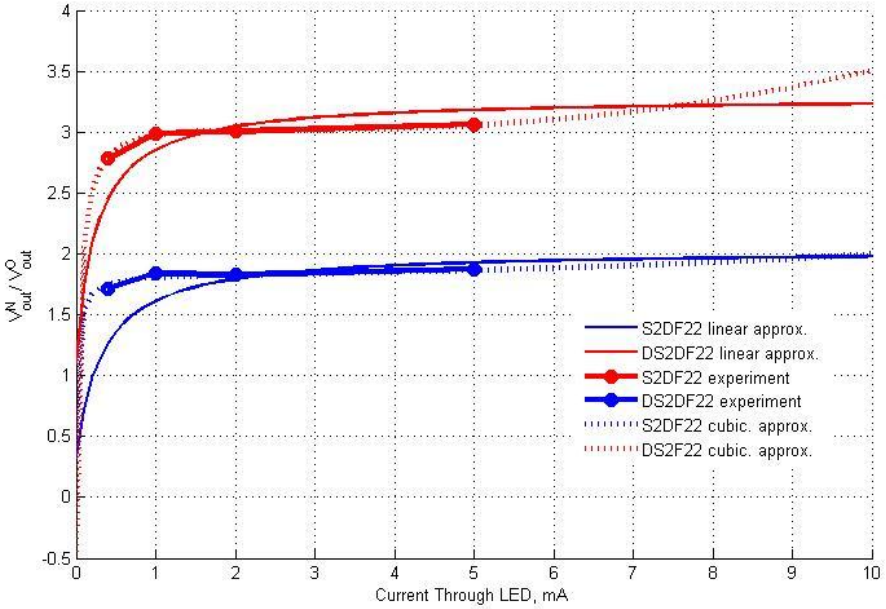

Figure 3.33. Comparison of the sensitivity of oxygen sensors S2DF22 and DS2DF22.

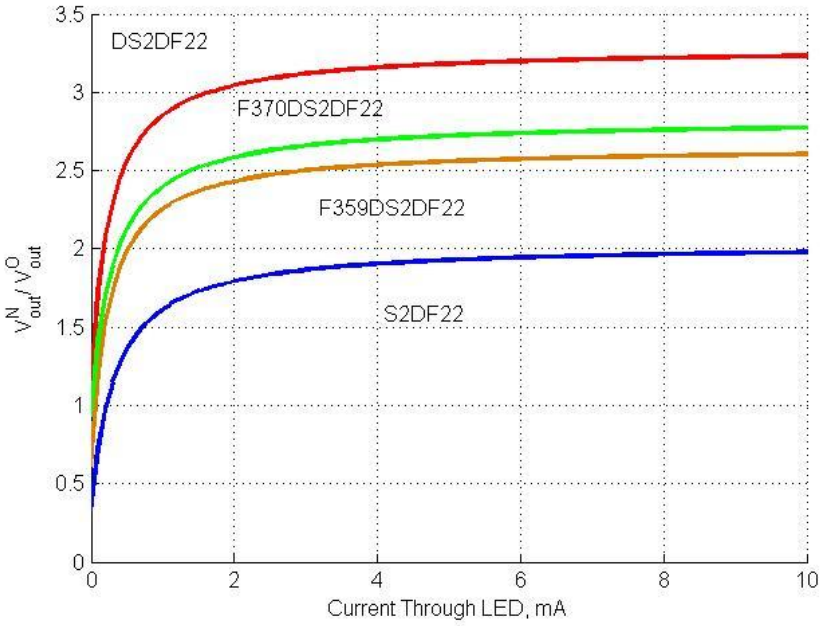

Figure 3.34. The advantage of sensor DS2DF22 over sensors S2DF22, F359S2DF22, and F370S2DF22.

3.6. Testing Temperature Effects on the OOS response

For the purpose of studying the temperature effects on the OOS response, we used a sensor based on a single-sized design configuration. The OOS employed the RedEye as a sensor element, the LED L200CUV405-8D as an illuminator, the TSL250 as a photo-detector, and two

Roscolux Color Filters #22 (F22) as a barrier filter. The schematic of an experimental setup is presented in Fig. 3.35. The 5 V fixed output of the Tektronix Laboratory DC Power Supply PS280 provides the nominal supply voltage for the TSL250 and the temperature sensor TMP35, the latter being used to measure the actual temperature of the gas under test. The LED is connected to a constant-current source circuit powered by the power supply PS280. The photo-detector, the current source, and the temperature sensor are mounted on a PCB located in the OOS casing. The OOS is positioned into the Benchtop Temperature Testing Chamber ESPEC supplied with a Programmable Watlow F4 Controller which allows us to set multiple test points ranging from -30 ^{o}C to 50 ^{o}C as well as measure thecurrent temperature in the testing chamber. The National Instruments USB-6210 Analog to Digital Converter (ADC) connected to a computer is used for processing output signals of the photo-detector, the temperature sensor TMP35, and the temperature sensor of the F4 controller.

The OOS casing is supplied with two hose nozzles. Its input nozzle is connected to a positioned in the test area handcrafted spiral heat exchanger made of a thin and long plastic tube. The output nozzle of the case is connected to a tube that goes out of the testing chamber and is used to release the gas from the case into the atmosphere. In our measurements, we used only three reference points of oxygen: the first point was the 20.9% concentration of the air volume, the second and the third points were 100% and 0% of the volume. To supply these gas concentrations into the OOS casing, the heat exchanger is connected either to an Air Pump E114229 or to one of compressed gas cylinders containing pure oxygen (UN# 1072) or nitrogen (UN# 1066).

Each measurement of oxygen concentration started after 20 minutes have elapsed after F4 controller's command to proceed to the next test point. During this interval, the temperature in the testing chamber was stabilizing, and the gas passing to the OOS case through the heat exchanger was either heating or cooling to the temperature of the test point. The difference between temperature measured by the TMP35 installed in the OOS casing, TMP35 in the hose connected to the OOS output nozzle, and the temperature of the test point, measured by F4 controller did not exceed 0.5^{o}C. Measurement results of the current temperature in the testing chamber, the actual temperature in the OOS casing, and the output of the photo-detector were recorded by the computer using a LabVIEW program. Fig. 3.36 illustrates the temperature dependence of the OOS output in the case of 21.9% oxygen concentration.

The overall temperature effects on the OOS response can be caused by several factors, such as the hysteresis effect, the effect of temperature on the RedEye fluorescence, the LED optical power, and the temperature expansion of the gas under test.

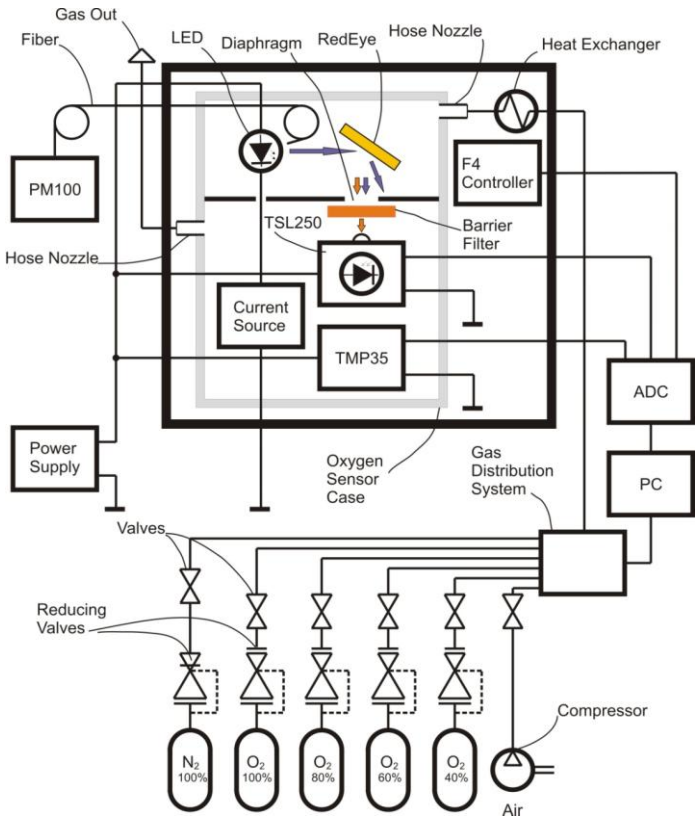

Figure 3.35. Setup for testing the temperature effects.

Hysteresis effect. Our experiments revealed the dependence of emission intensity measurement results not only on the gas temperature, but also on the history of past measurements, i.e. the hysteresis effect. Assuming that the temperature dependence of the RedEye emission is almost not affected by oxygen concentration, we obtain the following linear relationship:

$$I_n = -0.01T + 1.20 \qquad (3.20)$$

where I_n is normalized emission intensity and T is the temperature of the gas in ^{o}C. According to our next assumption, the hysteresis effect occurs not because of the RedEye intrinsic properties but because of the lag in temperature between the gas inside the OOS casing and the casing itself. Keeping in mind that the average difference between the two normalized emission intensities measured at the same temperatures, but with a different history, is 0.058, we can evaluate the temperature lag ΔT, using the relationship (3.12): ΔT=0.058/0.01=0.58^{o}C (See Fig. 3.36). We are able to decrease the temperature lag to 0.2^{o}C by changing the temperature sensor position on the PCB, moving it closer to the RedEye, and by using a thermal paste between the sensor and the PCB.

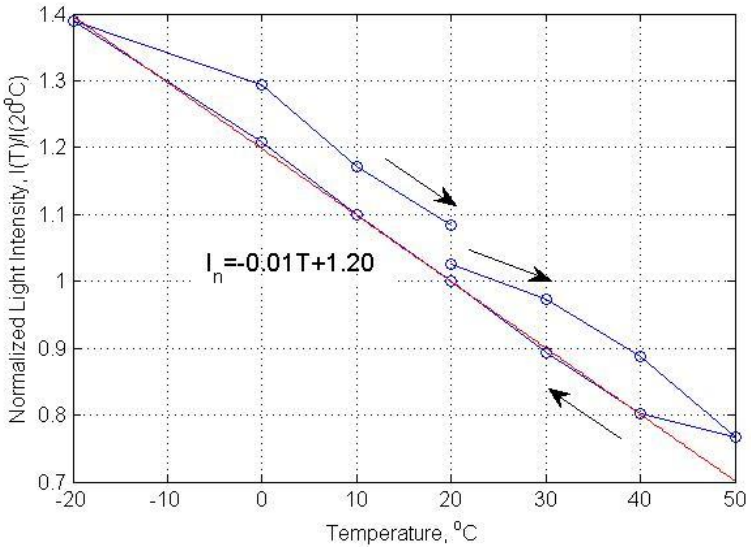

Figure 3.36. The temperature dependence of the OOS output.

Effect of temperature on the LED optical power. The contribution of the LED performance to temperature effects was estimated by examining the LED optical power variations in the temperature range from -20°C to 50°C. The LED and its constant current source based on the LM317 current regulator, which was adjusted to supply the 15 mA current, were positioned in the Testing Chamber. To couple the fiber connected to Thorlabs Digital Optical Power Meter to the LED, we placed the tip of the fiber connector positioned in the Testing Chamber directly onto the LED's emitting surface. The optical power measurements at different test points were conducted at a 20-minute interval. Fig. 3.37 illustrates the temperature dependence of the LED optical power. Linear curve fitting in Fig. 3.37 gives us the following linear relationship:

$$\Phi(T)\Big/_{\Phi(20C)} = -0.001T + 1.011 \qquad (3.21)$$

where $\Phi(T)/\Phi(20^oC)$ is normalized LED optical power, and T is the gas temperature, in °C. The absence of hysteresis testifies to the fact that the Test Chamber does not bear responsibility for the hysteresis we observed in the experiments to test the overall temperature dependence of the OOS output.

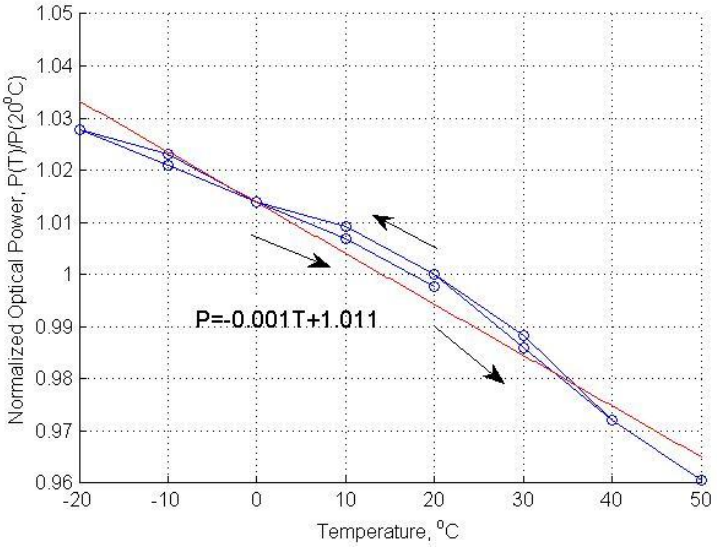

Figure 3.37. The temperature dependence of LED optical power.

According to Eq. (3.21), a 1°C increase in the temperature results in a 0.1% decrease in the normalized LED optical power, which may seem negligible. However, according to Eq. (3.11), this decrease is equivalent to the decrease of the supplied current by 0.001/0.075=0.013 mA; and according to the linear approximations presented in Table 3.3, such a decrease in the current can result in a decrease in the output of the TSL250 by up to 0.009 V (0.013*V), depending on oxygen concentration. From Fig. 3.32, depending on the selected calibration point V_0, the output of the TSL250 can range from 2 to 3.5 V. Thus, due to the dependence of the LED optical power on temperature, a 1°C increase in temperature can result in a 0.45 or even 0.9% (100%*0.009/2) decrease of the TSL250 output. The TSL250 output is proportional to fluorescence emission; therefore, a 1°C increase in the temperature results in a 0.45 or 0.9% decrease of the measured fluorescence intensity. Accordingly, to decrease the influence of the temperature dependence on measurement results, we have to set the highest possible output voltage. Setting the output voltage of the TSL250 at V_0=3.5 V, for OOS DS2DF22, allows us to decrease the influence of the temperature dependence on measurement results to 0.45% per 1°C in an oxygen-free gas. To decrease the OOS power consumption, we need to decrease the operating current by setting it, for instance, at 0.3 mA, in which case, however, the TSL250 output voltage is equal to only 2 V and the influence of the temperature dependence on measurement results increases to 0.9% per 1°C. However, it is not recommended that the operating current be decreased to less than 0.2 mA because it will lead to a sharp decrease in the OOS sensitivity (See Fig. 3.33).

Temperature expansion of the gas under test. A variation in the temperature of the gas under test results in the variation of the gas volume and oxygen concentration. From the ideal gas law equation, we obtain the relationship that shows that absolute oxygen concentration Q_a, normalized by a concentration value Q_{ac}, measured at temperature T_c, decreases when the gas temperature increases:

$$dQ_a/Q_{ac} = -(T_c + 273)/(T + 273)^2\, dT\,. \qquad (3.22)$$

According to Eq. 3.22, a 1°C increase in the temperature from Tc=20°C results in a 0.00341 (0.34%) decrease of the normalized absolute oxygen concentration. Considering that our experiments were conducted in the environment, where relative oxygen concentration $Q_c(T_c)$=20.9% under normal conditions, we can find that a 1°C temperature increase results in a 0.0713% (0.34%*0.209) decrease of relative oxygen concentration. Therefore, the estimated above resolution of our oxygen sensor $\Delta Q_{Q=20.9}=0.0144\%$ (See Eq. 3.10) allows us to register a change in the oxygen concentration caused even by a fraction of a degree temperature change and, as a consequence, the dependence of oxygen concentration on temperature cannot be neglected.

Comparison of temperature effects on the OOS response. The comparison of the overall temperature effect on the OOS response and the contributions of effects caused by the temperature dependence of the LED optical power and temperature expansion of the gas under test allows us to evaluate the effects of temperature on the RedEye fluorescence. To evaluate the contribution of the temperature gas expansion on overall measurement results, we will compare it with the overall resulting temperature dependence on measurement results. First, let us consider the Stern-Volmer Eq. 2.8 in the form:

$$I_0(T_c)/I(T) - 1 = K_{SV}Q(T). \qquad (3.23)$$

In the literature, the parameters of Eq. 2.8 have never been represented as functions of temperature. Evidently, the authors assume that the gas temperature T at the time of measurements is equal to the temperature of the gas T_c at the time of the sensor calibration. If the temperatures T_c and T are not equal, the Stern-Volmer constant needs to be corrected, e.g., by a second order polynomial. From Eq. 3.23, we have

$$dQ(T) = \frac{1}{K_{SV}}\, d\left(I_0(T_c)/I(T)\right). \qquad (3.24)$$

According to our experiments, with constant gas pressure conditions (1 atm), a normalized intensity of fluorescence emission depends on the gas temperature (Eq. 3.20); this dependence can be described by a linear regression:

$$I(T)/I_c(T_c) = aT + b \qquad (3.25)$$

where a=-0.01 and b=1.2 are correlation coefficients. We obtain the regression Eq. 3.25 under the assumption that the temperature dependence of a normalized intensity of fluorescence emission is nearly independent of oxygen concentration and, which was proven by the good fitting to experimental results (See Fig. 3.36).

The overall resulting temperature dependence can be calculated by transforming Eq. 3.24 into

$$dQ = \frac{1}{K_{SV}} d\left(\frac{I_0(T_c)}{I_c(T_c)} \frac{I_c(T_c)}{I(T)}\right). \qquad (3.26)$$

Then, using Eq. 3.24 and Eq. 3.25, we transform Eq. (3.26) into

$$dQ = d(^{1 + K_{SV} Q_c(T_c)}/_{aT + b}) \qquad (3.27)$$

and, finally, after differentiating Eq. (3.27), with respect to *T* we have

$$dQ = -(^{a(1 + K_{SV} Q_c(T_c))}/_{(aT + b)^2}). \qquad (3.28)$$

The contribution of the LED performance to the temperature effects can be evaluated, differentiating Eq. (3.24), with respect to *T*

$$dQ(T) = -\,^{I_0(T_c)}/_{K_{SV} I(T)^2}\, dI(T). \qquad (3.29)$$

Taking into account Eq. (3.26) and the fact that a 1^{o}C increase in the temperature can result in an approximately 0.45-0.9% decrease of *dI(T)/I(T)*, we obtain

$$dQ(T) = {}^{1}/_{K_{SV}(aT + b)}\, {}^{I_0(T_c)}/_{I_c(T_c)}\, {}^{dI(T)}/_{I(T)}. \qquad (3.30)$$

Comparison of factors affecting the measurement results in the case of a 1^{o}C increase in the temperature of an ideal gas under test in the -20^{o}C to 50^{o}C range of temperatures is presented in Fig. 3.38. The green and brown curves represent the effects responsible for the temperature dependence of the LED optical power in the case of the maximum and minimum operating current modes of the OOS. It is obvious from the comparison that the temperature dependence of the LED optical power is responsible for the major contribution to the overall temperature effects on the OOS response. The effects caused by a temperature gas expansion are relatively small, proportional to the temperature, and can be easily taken into account for correcting measurement results. Therefore, we can neglect the contribution of effects caused by the RedEye temperature dependence, i.e., consider the RedEye temperature-independent, and correct measurement results taking into account the temperature gas expansion and stabilize the LED optical power.

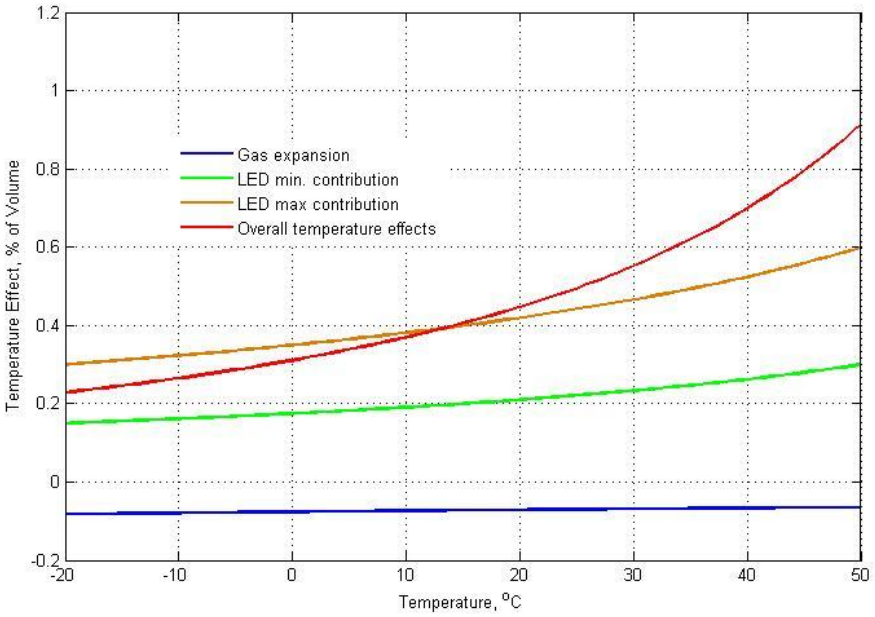

Figure 3.38. Comparison of temperature effects.

3.7. Development of a Gas Distribution System

For a more detailed study of the OOS and its performance evaluation, we designed a gas distribution system which allows us to supply the gas of known oxygen concentration into the test area. The schematic of a possible configuration of the gas distribution system is presented in Fig. 3.39. The system consists of Clippard solenoid valves, handcrafted manifolds, a valve controller designed specifically to control the valves, a mass flow meter AWM2000 supplied with an analog to USB converter, a Rosewill RHUB-310 USB Hub, and an AC/DC 12 V power adaptor. Depending on the design or the number of employed manifolds, our design provides the implementation of various system configurations. To control any of these system configurations, we developed LabView software. The front panel of the software interface is presented in Fig. 3.40. Schematic diagrams of system configurations, which include the listed above elements, can be drawn by the user using any drawing program and saved as JPEG or BMP files in a certain folder. The schematic diagram of a system configuration employed during the previous time is presented by the software on the front panel of the program interface automatically when the system starts, and used as a mnemonic that shows the current state of the system. To start working with a new configuration of the system, the user browses the folder with configuration files, selects the necessary configuration, and the selected diagram is displayed on the front panel. The LED LabVIEW elements are ON when the corresponding valve is open, and are OFF when it is closed. The user can drag the LED elements over each solenoid valve by pressing the left mouse button.

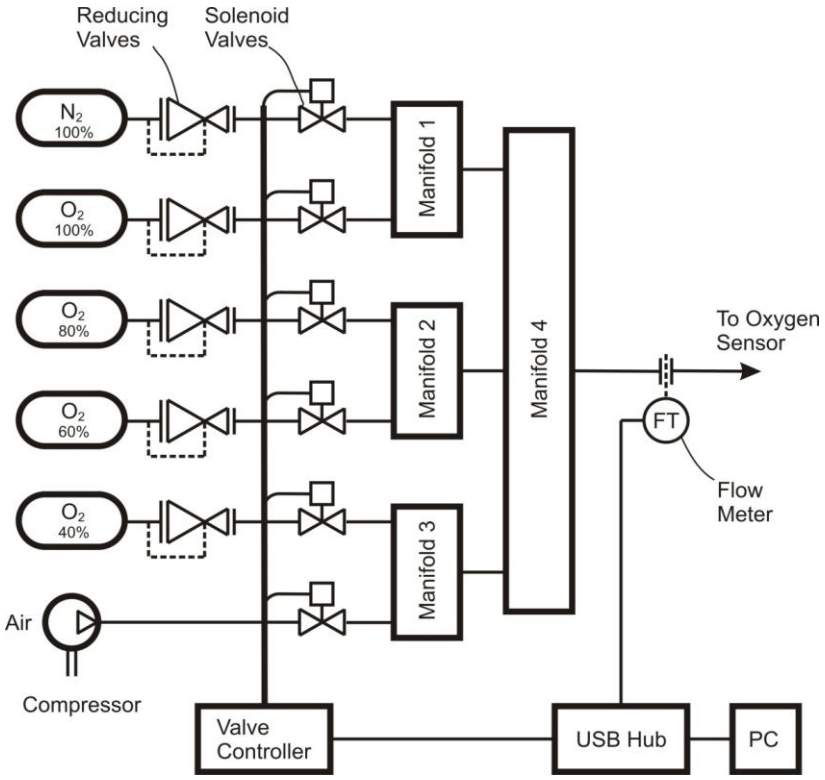

Figure 3.39. Schematic of the gas distribution system.

If the user starts the system from the tab 'Manually,' s/he can turn on and off any valve of the system by pushing the corresponding valve buttons in this tab. If the system needs to start from the tab "Auto," the state of the valves will be controlled by the software, according to one of schedules saved as Excel files into the folder assigned for schedules. A schedule appears as a table with three columns: Actuation Time in sec, Valve Number, and Operation, where 1 means that the valve should be open, starting from the Actuation Time moment, and 0 means that the valve should be closed. The schedule employed the last time is presented by the software on the tab automatically when the user selects tab 'Auto.' To start work with a new schedule, the user browses the folder with schedules and selects the schedule he needs. The system performance was tested for the basic system configuration presented in Fig. 3.41.

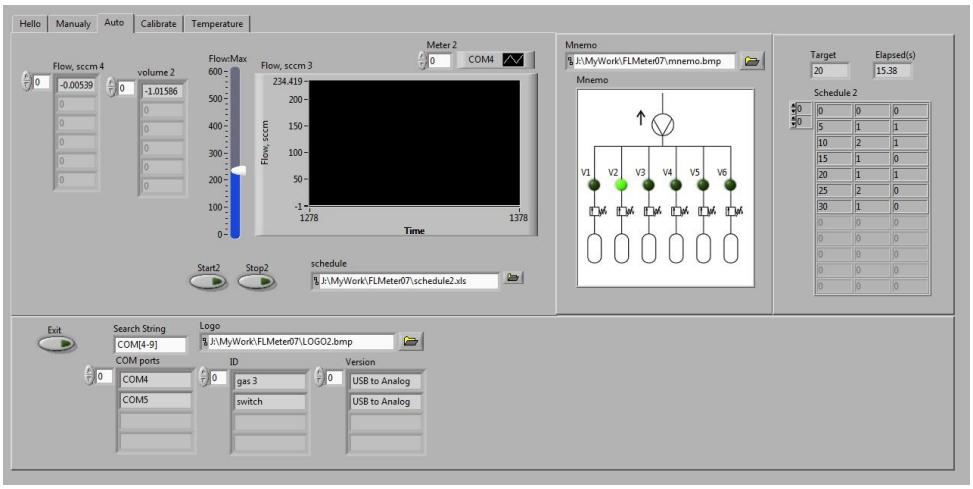

Figure 3.40. The front panel of the Gas Distribution System LabVIEW software.

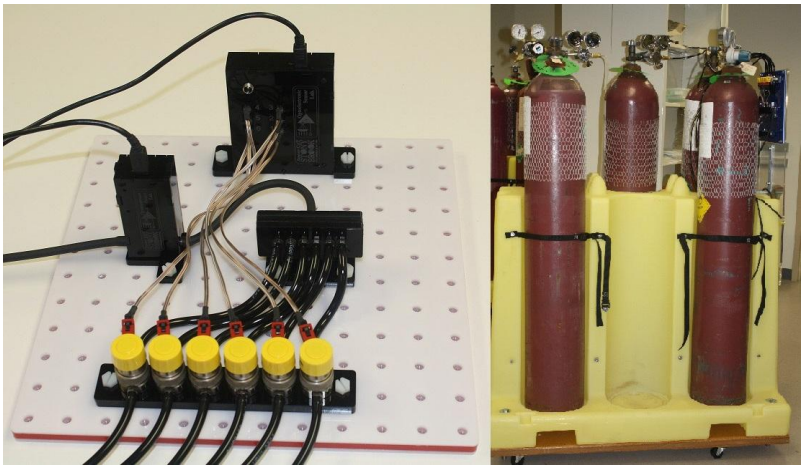

Figure 3.41. A basic configuration of the gas distribution system.

3.8. The OOS Calibration

In order to reduce the dependence of the OOS response on temperature, we propose to modify the Stern-Volmer equation by rewriting it in the form:

$$I(Q_n(T_c),T_c))(aT+b)\Big/_{I(Q(T),T))} - 1 = K_{SV}Q(T) \quad (3.31)$$

and to use at least four calibration points for the OOS calibration. We recommend that the first calibration point CP_1 be obtained by measuring fluorescence intensity in air under normal conditions ($T_1=T_c=20^oC$, $I_1=I_c(T_c)$). The second calibration point CP_2 can be obtained if the air is heated, e.g., up to 50°C ($T_2=50^oC$, $I_2=I(T_2)$). Calibration points CP_1 and CP_2 allow us to find the correlation coefficients *a* and *b* (See Eq. 3.25):

$$a = {(I_1 - I_2)}/{I_1{}^2(T_1 - T_2)} \quad (3.32)$$

$$b = {(I_2 - aI_1{}^2)}/{I_1}. \quad (3.33)$$

Calibration points CP_3 and CP_4 can be obtained according to the traditional calibration procedure by measuring the maximal fluorescence intensity $I_3=I_0$ in an oxygen-free gas (oxygen concentration $Q_3=0\%$) and fluorescence intensity I_4 approaching to 0 in pure oxygen (oxygen concentration $Q_4=100\%$), where the temperatures of both gases T_3 and T_4 should be equal $T_1=T_c=20^oC$, i.e., all calibration points should be obtained at the calibration temperature T_c (See Fig. 3.25). If temperatures T_3 and T_4 differ from T_c, then fluorescence intensity I_3 and I_4 can be corrected using Eq. (3.23):

$$I_3(T_c) = {I_3(T_3)}/{(aT_3 + b)} \quad I_4(T_c) = {I_4(T_4)}/{(aT_4 + b)}. \quad (3.26)$$

Thus, the Stern-Volmer equation Eq. (3.15) is modified to take the form of Eq. (3.31).

As can be seen from the modified Stern-Volmer equation Eq. (3.23), the plot of $I_0(T_c)(aT+b)/I(T)-1$ vs. oxygen concentration $Q(T)$ should give a straight-line relationship with the K_{SV} slope. We can use calibration points CP_3 and CP_4 to find this slope:

$$K_{SV} = {\left({I_3(aT_4 + b)}/{I_4} - (aT_3 + b)\right)}/{\left(Q_4(T_4) - Q_3(T_3)\right)}. \quad (3.27)$$

Apparently, the modified Stern-Volmer equation Eq. 3.23 is transforming to its traditional form where the gas temperature T equals T_c, e.g., if calibration points CP_1, CP_3 and CP_4 are obtained at the same temperature T_c and if $aT_c+b=1$. As a consequence, the traditional Stern-Volmer equation is appropriate to use only for stable temperature conditions, where the temperature of the gas under test is constant and $T_c=(1-b)/a$.

The dependence of the fluorescence response on temperature is illustrated in Fig. 3.42. The experimental fluorescence response we obtained earlier at 20°C (See Fig. 3.24) is marked in Fig. 3.42 with a red curve.

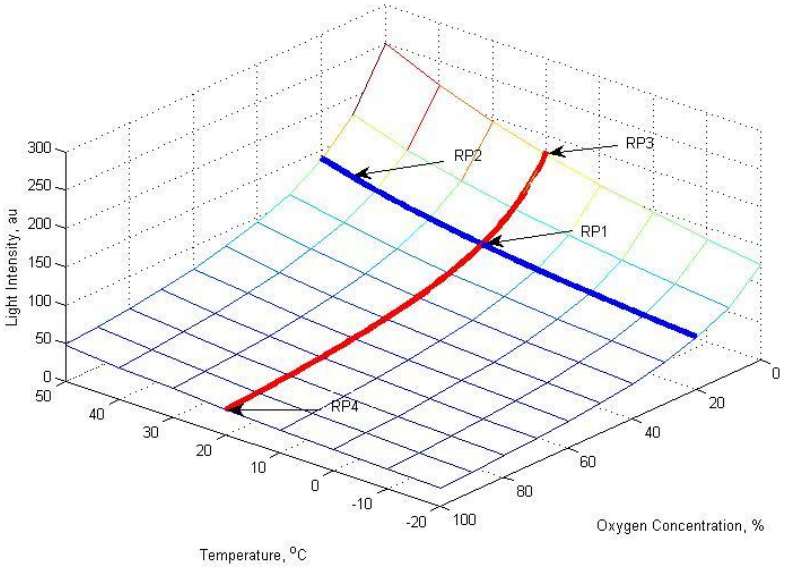

Figure 3.42. Dependence of fluorescence response on temperature.

In Fig. 3.43, we present the OOS calibration plot obtained using the modified Stern-Volmer equation. The experimental plot obtained earlier (See Fig. 3.25) is marked in Fig. 3.43 with a red line. Fig. 3.43 demonstrates that the coefficient K_{SV} obtained using the modified Stern-Volmer equation does not depend on temperature.

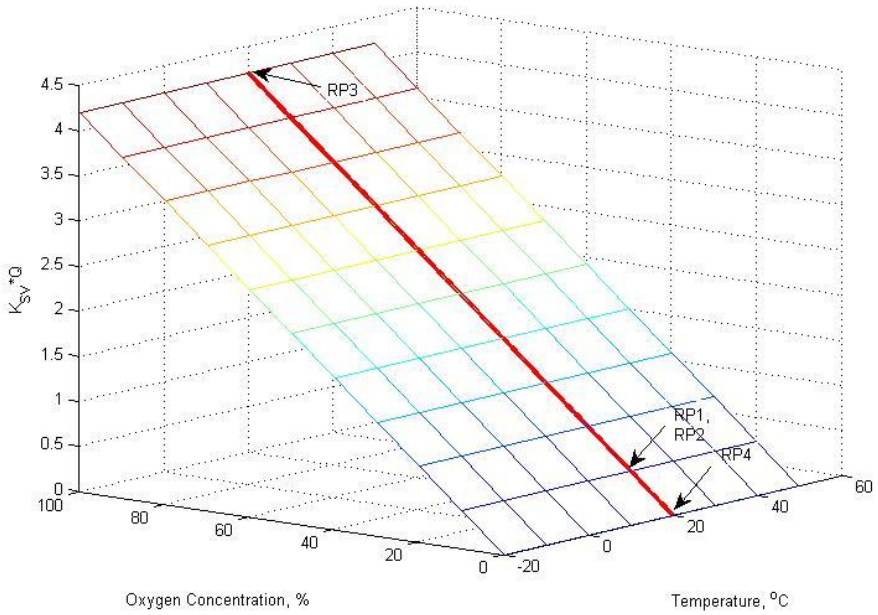

Figure 3.43. Calibration of the OOS.

3.9. Analytical model of the OOS

In my analytical model, a sensor element (SE) is presented in the form of a sandwich structure consisting of m (m=1, 2, …) thin plane-shaped sensing films containing a uniformly immobilized fluorescent material. Below we will distinguish between a "multi-film SE" and a traditional "single-film SE," consisting of only one sensing film (m=1). The left surfaces of the L-thick sensing films are located at $x=(m\text{-}1)\cdot L$; their right surfaces are located at $x=mL$. The surfaces of a sensing film can interact with a gas of a Q oxygen concentration, as a result of which oxygen molecules, due to diffusion, can penetrate into the sensing films. I will refer to the sensing film as a "two-interface sensing film" if both, right and left, surfaces interact with gas. I will refer to the sensing film as a "one-interface sensing film" if only one surface interacts with gas. Because the length of the sensing film is incomparably larger than its thickness, we can assume that the length of the sensing film is infinite and neglect oxygen diffusion near the edges of the film. To simplify my model, we can also neglect the gaps between sensing films because these gaps are supposed to be rather small in order to avoid their influence on the light propagation from one film to another. However, we assume that all surfaces of all films are under similar conditions, i.e., the gaps should be large enough to provide oxygen diffusion to all sensing surfaces. We suppose that each sensing film is divided into $N\text{-}1$ layers of minute thickness dX. N grid points X_i $(i=1, 2, .., N)$ are coordinates of boundaries of the layers which divide the axis x intervals $[(m\text{-}1)L, mL]$ by $N\text{-}1$ intervals, whose length is dX. A schematic illustration of a single-film SE cross section is presented in Fig. 3. 44. In the case of a double-sided optical design configuration of an OOS, its illuminator is located on one side of the SE and its photo-detector is located on the other side. In the case of a single-sided optical design configuration of an OOS, both the illuminator and the photo-detector are located on one side of the SE.

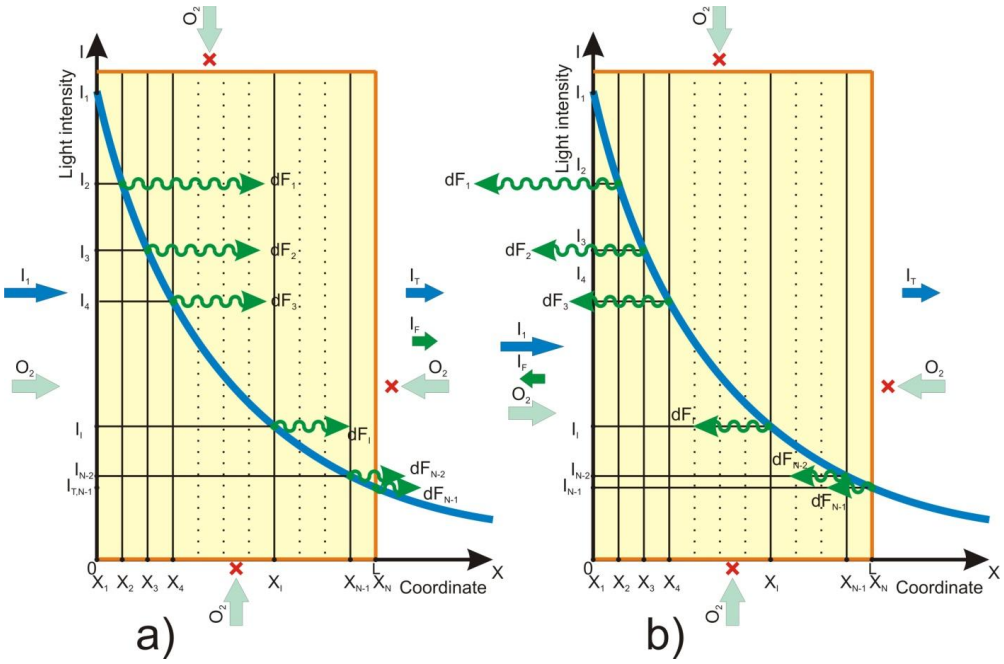

Figure 3.44. Schematic illustration of a single-film SE: a) double-sided optical design configuration; b) single-sided optical design configuration.

The MATLAB model implementation allows us to study the dependence of the SE performance on the thickness L of its sensing films, the number s of the films and their interfaces, the extinction coefficient ε, the diffusion constant D, the oxygen concentration Q in the surrounding gas, and on the employed optical design configuration. To calculate characteristics of a sensing film, we vary its thickness L by incrementing it by 1μm, taking into account oxygen concentration distribution throughout 99 layers.

To better understand the fluorescence sensing mechanism, we first study the response of a single-film SE to the change of excitation light intensity if the intensity remains below the saturation level, and if the SE is oxygen-insensitive, or the oxygen concentration is constant. Second, we study the response of an oxygen-sensitive SE to the change of oxygen concentration at a constant excitation light intensity for the OOS single- and double-sided optical design configurations. Finally, we compare the above-mentioned response of the oxygen-sensitive SE with the response of the SE using a novel optical design configuration developed during our research. For numerical experiments, we use experimental values of parameters obtained with our setup and parameters presented in the specification of the RedEye. We suppose that characteristics of the fluorescent material employed in our SE are similar to the RedEye characteristics. If the sensing film is of the same thickness, in both the SE and the RedEye, then their Stern-Volmer constant K_{SV}=0.042 $\%^{-1}$ and response time t_{65}=1s are the same.

3.9.1. **Response of an oxygen-insensitive SE.** An oxygen-insensitive SE converts the variation ΔI_1 of the excitation light intensity I_1 to the variation ΔI_F of fluorescence emission intensity. Let I_i (i=1, 2, …, N-1) be the intensity of the excitation light striking the layer i of a single-film SE, I_{Ti} the intensity of transmitted light, and I_{T0} the intensity of the light emitted by a light source, then $I_i=I_{Ti-1}$ (i=1, 2, …, N-1), and $I_1=I_{T0}$. According to the Beer-Lambert law (See Eq. 2. 3), light of incident intensity I_i and of wavelength λ_E illuminating the layer i of the SE is attenuated. The transmitted light intensity I_{Ti} can be calculated as

$$I_{Ti} = I_i e^{-2.3\cdot\varepsilon(\lambda_E)\cdot c\cdot dX} = I_1 e^{-2.3\cdot\varepsilon(\lambda_E)\cdot c\cdot X_{i+1}}. \quad (3.28)$$

From Eq. 3.28 and Eq. 2.4, we can calculate the intensity of fluorescence light emitted by the layer i

$$I_{Fi} = kS_f I_{Ti}(1 - e^{-2.3\cdot\varepsilon(\lambda_E)\cdot c\cdot dX}). \quad (3.29)$$

Because, in the case of a double-sided optical design configuration, the optical pass length of the light emitted by the layer i is L-idX, and fluorescence is emitted at another wavelength $\lambda_F>\lambda_E$, the contribution of the layer i to the SE total emission is

$$I_{FTi} = I_{Fi} e^{-2.3\cdot\varepsilon(\lambda_F)\cdot c\cdot(L-i\cdot dX)}. \quad (3.30)$$

In the case of a single-sided optical design configuration, the optical pass length of the light emitted by layer i is

$$I_{FTi} = I_{Fi} e^{-2.3\cdot\varepsilon(\lambda_F)\cdot c\cdot i\cdot dX)}. \quad (3.31)$$

The SE emission light intensity I_F is calculated as the sum of contributions I_{FTi} of all N-1 layers:

$$I_F = \sum_{i=1}^{N-1} I_{FTi}. \qquad (3.32)$$

From Equations 3.28-3.32, fluorescence emission intensity I_F is proportional to the product $I_1 k S_f$; hence, we can consider the normalized value $I_F/I_1 k S_f$ of the SE light intensity emission, excluding the dependence of our results on characteristics of a particular setup (See Fig. 3.45). Selecting a baseline value, from the range given in the literature, of molar absorption coefficients $\varepsilon(\lambda_E)$, $\varepsilon(\lambda_F)$ and concentration c, for a Ruthenium-based SE employed in our OOS, presents a difficulty as values of these parameters for different SEs based on Ruthenium immobilized in sol-gel matrix, which were reported in different papers, can vary in a wide range. However, we can calculate the product $c \cdot \varepsilon(\lambda)$, using Eq. 1.2 and experimental measurement data of absorbance $A(\lambda)$ and thickness L of the SE:

$$\varepsilon(\lambda) \cdot c = {}^{A(\lambda)}/_{L}. \qquad (3.33)$$

Fig. 3.45 demonstrates that each combination of molar absorption coefficients $\varepsilon(\lambda_E)$, $\varepsilon(\lambda_F)$ determines the value of the SE optimal thickness L_{opt}, i.e. such thickness value that provides a maximal fluorescence response. The higher values of molar absorption coefficients are, the higher the SE dynamic range is, and the smaller the value of L_{opt} is. If the SE is thinner than L_{opt}, then its fluorescence response is always greater than the fluorescence response of SEs, whose thickness is the same and molar absorption coefficients are smaller. If the SE is thicker than L_{opt}, then its fluorescence response becomes smaller than the fluorescence response of SEs of a similar thickness and with smaller molar absorption coefficients.

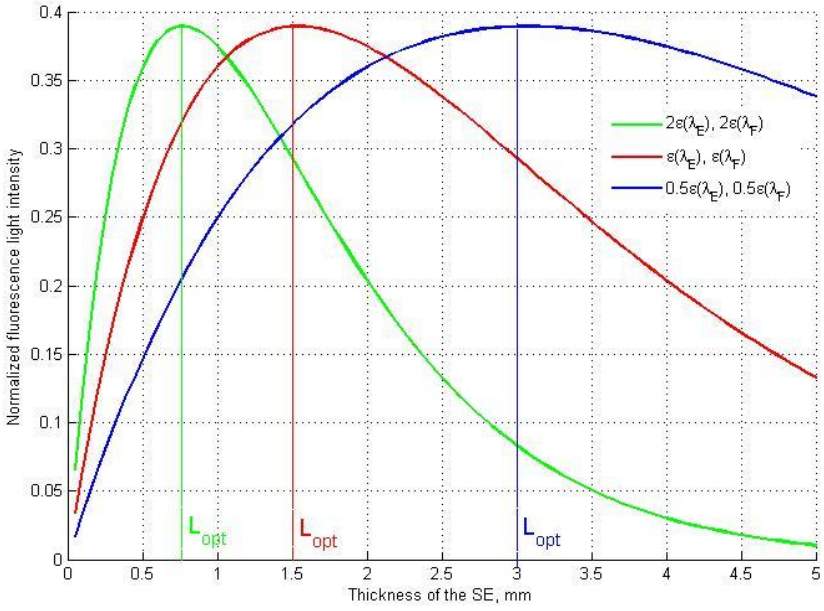

Figure 3.45. Optimal thickness of an oxygen-insensitive SE.

The SE sensitivity S can be defined as the ratio of the incremental output ΔI_F to the incremental input ΔI_1:

$$S = {dI_F}/{dI_1}. \qquad (3.34)$$

From Eq. 3.34 and 2.1, the SE sensitivity is a constant which is proportional to the product kF and does not depend on the excitation light intensity value. The graphs in Fig. 3.45 give us an idea of the SE sensitivity dependence on the SE thickness and values of molar absorption coefficients. An increase in the SE thickness results in its sensitivity increase if the SE thickness is less than L_{opt}, and in its sensitivity decrease if the thickness is greater than L_{opt}.

3.9.2. Response of an oxygen-sensitive SE. According to the Model conditions, m sensing films of the SE are initially at a uniform oxygen concentration Q_0=0 ($0 \le x \le mL$, m=1, 2, …). At moment $t=0$, the concentration of the gas surrounding the films has a step-like increase and is maintained at concentration Q_S=100%. In two-interface sensing films at moment $t=0$, the left-side concentration Q_L ($x=(m\text{-}1)\cdot L$) and the right-side ($x=m\cdot L$) concentration Q_R equal 100%; in one-interface sensing films at moment $t=0$, the left-side concentration Q_L equals 100%, and the right-side concentration Q_R does not change and equals Q_0. At any time $t>0$, the concentration distribution $Q_X(t)$ within the SE can be determined by the diffusion equation (Eq. 2.10).

Let Q_i^n be the oxygen concentration in layer i (i=1, 2, …, mN-1) at moment $t=t^n=n\cdot\tau$, where τ is of an integration time step, n is the step number, I_{Qi}^n is fluorescence intensity in the presence of oxygen in layer i at moment t, and I_{Fi} is fluorescence intensity in layer i in the absence of oxygen (Eq. 3.20). The intensity fluorescence light emitted by layer i in the presence of oxygen can be calculated using the Stern-Volmer equation (Eq. 2.8):

$$I_{Qi}^n = {I_{Fi}}/{(1 + K_{SV} Q_i^n)}. \qquad (3.35)$$

From Eq. (3.30) and Eq. (3.31), we can calculate the contribution of the layer i to the SE total emission I_{QTi}^n for a double-sided optical design configuration:

$$I_{QFi}^n = I_{Qi}^n e^{-2.3\cdot\varepsilon(\lambda_F)\cdot c\cdot(mL - i\cdot dX)} \qquad (3.36)$$

The contribution of layer i to the SE total emission I_{QTi}^n for a single-sided optical design configuration can be calculated from Eq. (3.30) and Eq. (3.32):

$$I_{QFi}^n = I_{Qi}^n e^{-2.3\cdot\varepsilon(\lambda_F)\cdot c\cdot i\cdot dX} \qquad (3.37)$$

and the contribution of all layers to the SE total emission intensity I_{QF}^n in the presence of oxygen:

$$I_{QF}^n = \sum_{i=1}^{N-1} I_{QFi.}^n \qquad (3.38)$$

According to Eq. (3.8,) an oxygen-sensitive SE sensitivity can be evaluated as

$$S = \frac{I_F}{I_{QF}^n} \qquad (3.39)$$

where I_F is fluorescence intensity in the absence of oxygen, calculated using Eq. 3.32, and n is the number of integration steps. The OOS response R is defined as

$$R^n = \frac{1}{K_{SV}}\left(\frac{I_F}{I_{QF}^n} - 1\right). \qquad (3.40)$$

We use the finite difference scheme [101] for a numerical solution of the diffusion equation, to calculate the distribution of oxygen concentration Q_i^n in one sensing film (i=1, 2, …, N-1), assuming that the oxygen concentration distribution in other sensing films is similar ($Q_{i+mL}^n = Q_i^n$). After replacing the time and spatial derivatives in Eq. 2.11 by a first order forward difference and by a symmetric difference, we obtain a system of linear algebraic equations:

$$\frac{(Q_i^{n+1} - Q_i^n)}{\tau} = D \cdot \frac{(Q_{i+1}^{n+1} - 2Q_i^{n+1} + Q_{i-1}^n)}{\tau^2} \qquad (3.41)$$

where $Q_i^0 = Q_0$, $i=2, \ldots, N-1$; and $Q_1^n = Q_L$, $n>0$; $Q_N^n = Q_R$, $n>0$.
The system of equations (3.41) can be transformed into the system:

$$A_i Q_{i+1}^{n+1} - B_i Q_i^{n+1} + C_i Q_{i-1}^{n+1} = F_i \qquad (3.42)$$

where $A_i = C_i = D/\tau^2$, $Bi = 2D/\tau^2$, and $Fi = -Q_i^n/\tau$.

Assuming the existence of such sets of coefficients as α_i and β_i ($1 \le i \le N-1$) which provide

$$Q_i^{n+1} = \alpha_i Q_{i+1}^{n+1} + \beta_i \qquad (3.43)$$

System 3.42 can be transformed to

$$A_i Q_{i+1}^{n+1} - B_i Q_i^{n+1} + C_i \alpha_{i-1} Q_i^{n+1} + C_i \beta_i = F_i \quad (3.44)$$

which gives

$$Q_i^{n+1} = \frac{A_i}{(B_i - C_i \alpha_{i-1})} Q_{i+1}^{n+1} + \frac{(C_i \beta_{i-1} - F_i)}{(B_i - C_i \alpha_{i-1})} . \qquad (3.45)$$

The system of equations (Eq. 3.45) is equal to the system equations (Eq. 3.43) if, for all $i=2,3,\ldots,N-1$

$$\alpha_i = \frac{A_i}{(B_i - C_i \alpha_{i-1})}, \ \beta_i = \frac{(C_i \beta_{i-1} - F_i)}{(B_i - C_i \alpha_{i-1})}. \qquad (3.46)$$

Values $\alpha_1 = 0$ and $\beta_1 = Q_L$ that are needed to calculate all α_i and β_i, using Eq. 3.46, are obtained from left-side boundary conditions. Using Eq. 3.45, we calculate Q_{N-1}^{n+1}, $Q_{N-2}^{n+1}, \ldots, Q_2^{n+1}$ taking into account the right-side boundary condition $Q_1^{n+1} = Q_R$.

To calculate a new oxygen distribution before the time is incremented ($t^n = n \cdot \tau$), we modify the right-side boundary condition as follows: $Q_R = Q_R + Q_{N-1}^{n-1} - Q_{N-2}^{n-1}$. The calculations continue until the incremented time equals the finite time.

Figure 3.46 shows the calculated oxygen concentration distribution along a 10 μm single-film SE for different time periods.

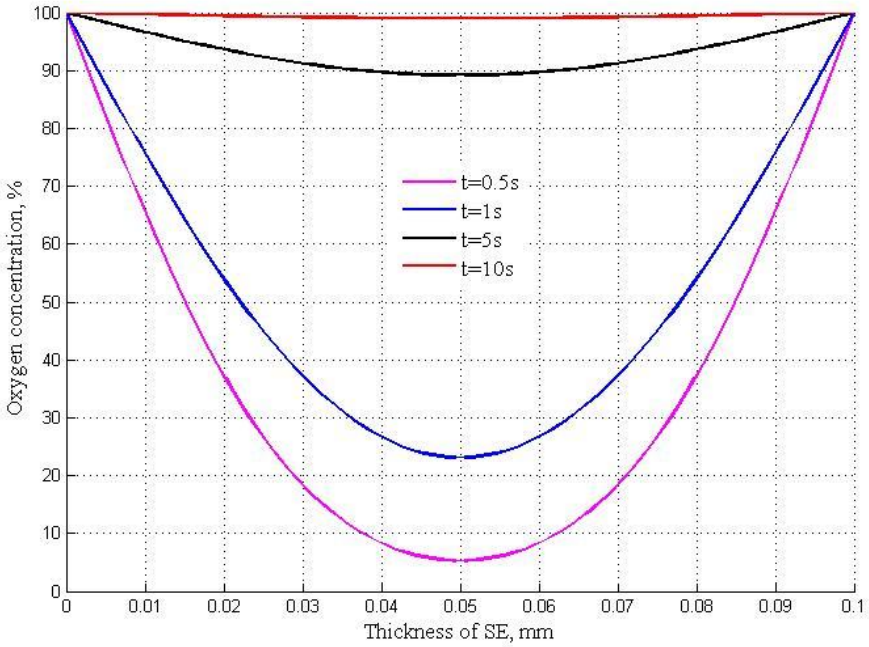

Figure 3.46. Oxygen concentration distribution along the 10 μm two-interface sensing film for different time periods.

Determination of a diffusion coefficient. The selection of a baseline value of the diffusion coefficient *D* for the SE employed in our OOS, from the range of values of diffusion coefficients for Ruthenium-based SE given in the literature, is hindered by the absence of all required information. However, we can determine the value of the diffusion coefficient using known values of the SE thickness *L* and its response time t_{65}. Fig. 3.47 demonstrates the process of estimating a diffusion coefficient *D*, using our analytical model. Fig. 3.47 illustrates the input signal as a step of oxygen concentration from 0 to 100%. It is our assumption that the thickness of the SE under test is 10 μm, its response time t_{65}=1s, and the predicted value 0.5*D* of the diffusion coefficient is taken from the range mentioned above. If the plot of SE response calculated using Eq. 3.40 intersects the vertical line $x=t_{65}$ at a step response level lower than 65%, then the diffusion coefficient value increase by twice (from 0.5*D* to *D* and then up to 2*D*). If the plot of SE response intersects the line $x=t_{65}$ at a step response level higher than 65%, then the diffusion coefficient value should be selected out of the values located between the last two selected values, e.g. 1.4*D*. Such iterations should continue until the plot of the calculated SE response intersects the line $x=t_{65}$ at exactly 65% level of the step response. The last selected value is considered the SE diffusion coefficient.

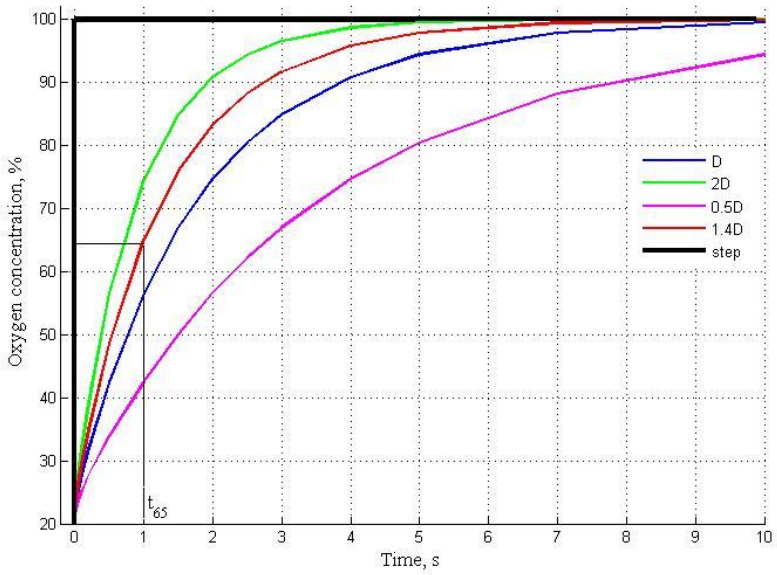

Figure 3.47. Calculated step response for the 10μm two-interface sensing film.

Optimal thickness of the SE. Numerical experiments carried out with different parameters of the oxygen-sensitive SE reveal the existence of the optimal thickness L_{opt} of the employed sensing film. Unlike the dependence of the optimal thickness L_{opt} on molar absorption coefficients which we observed studying oxygen-insensitive SEs (See Fig. 3.45), the optimal thickness L_{opt} of the oxygen-sensitive film depends not only on molar absorption coefficients, but also on oxygen concentration. The dependence of normalized fluorescence light intensity on the thickness of the double-interface film employed in the OOS, based on double-sided optical configuration, is presented in Fig. 3.48. The figure demonstrates that the film optimal thickness L_{opt} increases with an oxygen concentration increase, and decreases with an oxygen concentration decrease.

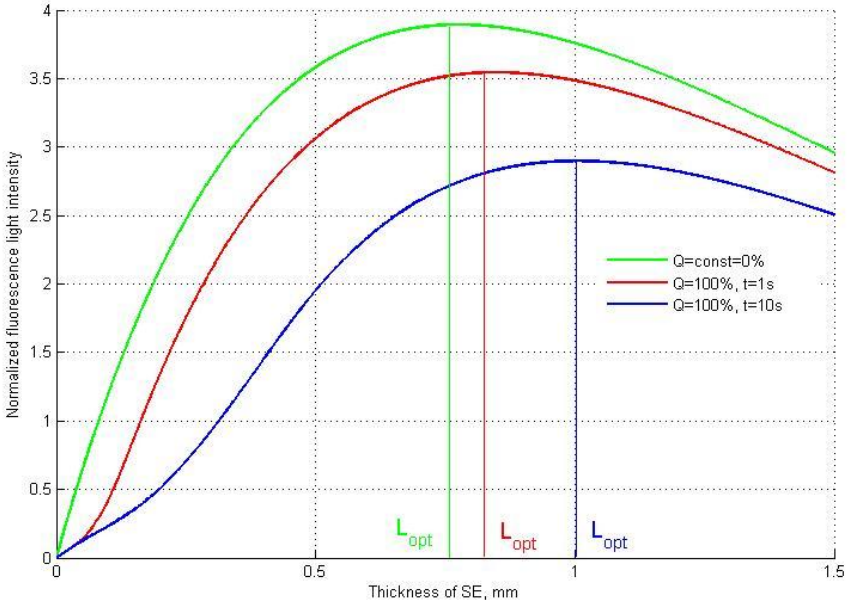

Figure 3.48. Optimal thickness of a two-interface sensing film.

Fig. 3.49 demonstrates that the OOS single-sided optical design configuration provides a higher fluorescence signal, as compared to the double-sided design configuration. This advantage of the single-sided optical design configuration is observed when the film thickness is around L_{opt}. Depending on molar absorption coefficients and oxygen concentration, the film optimal thickness L_{opt} varies from 0.5 to 1 mm. Even in the case of oxygen concentration equaling 0%, L_{opt} exceeds the thickness of sensing films employed in oxygen-sensitive SEs, which is commonly in the range of 1-100 μm. To excite a fluorescent material immobilized in such thick sensing films, excitation light of rather high intensity is required. However, the high-power excitation light can lead to photo-bleaching and fluorescence emission saturation. Our analytical model does not consider these two phenomena and can be applied only to investigate properties of thin oxygen-sensitive films ordinarily used in SEs.

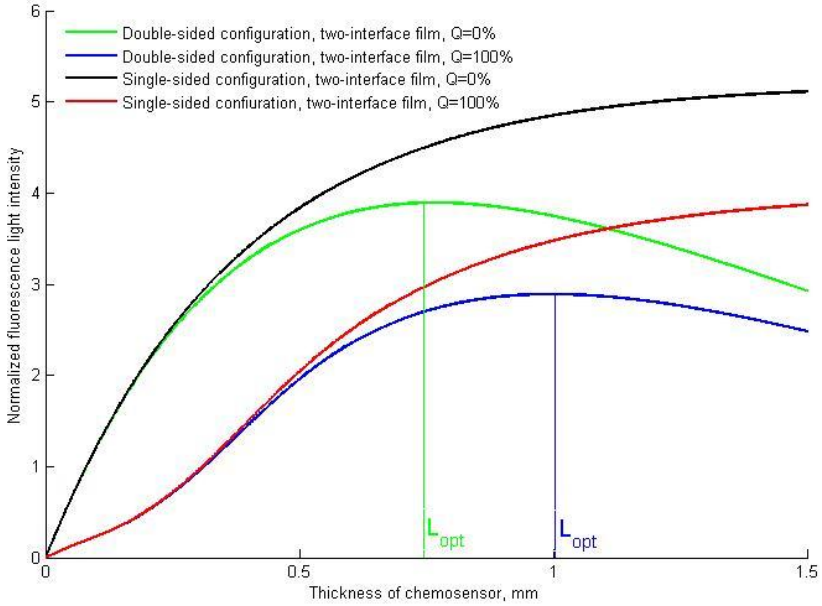

Figure 3.49. Comparison of the double- and single-sided OOS configurations.

Response of a single-film SE. Graphs of the dependence of the calculated single-film SE response on the film thickness are presented in Fig. 3.50. Response R^n is calculated according to Eq. 3.38, where the integration time t^n equals the expose times – 1 s and 2 s. Fig. 3.50 demonstrates that an increase in the sensing film thickness leads to a decrease in the SE response value and an increase in the SE response time t_{65}. For example, an increase in the thickness of a one-interface sensing film from 43 to 61 μm decreases the SE response value from 65% to 45%, or increases its response time t_{65} from 1 s to 2 s. These graphs also allow us to determine the value of the sensing film thickness $L=L_R$ which can provide a particular response level R in the response time $t_R=t^n$. For example, an intersection of the response level R=65% and the graph of the SE response which is calculated for the integration time set at t^n=1 s allows us to determine the thickness of a sensing film which provides the t_{65}=1s response time. To provide the same response time for both one-interface and the two-interface sensing films, the one-interface sensing film should be thinner. As an example, to provide the response time t_{65}=1 s, the thickness of a two-interface and a one-interface sensing film should be L_{65}=73 μm and L_{65}=43 μm, respectively.

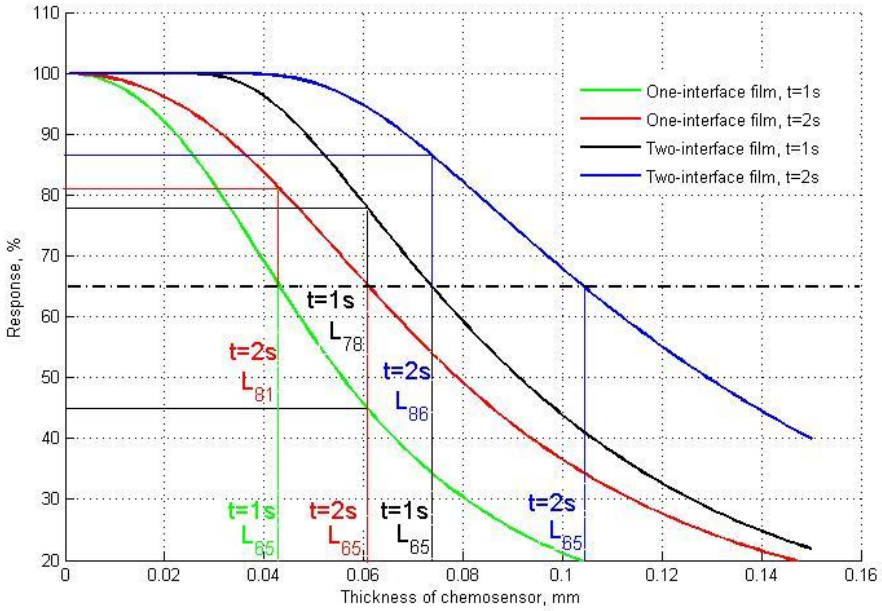

Figure 3.50. Calculated dependence of the single-film SE response on the thickness of its sensing film and integration time.

***Sensitivity of a single-film SE*.** The calculated dependence of the SE sensitivity on the thickness of its sensing film, at a constant integration time t^n, is presented in Fig. 3.51. From this figure, the sensitivity of a one-interface film SE increases monotonically as the film's thickness film decreases. The sensitivity of a two-interface film SE increases monotonically until as the thickness of the film decreases and reaches the value of L_{max}. The further decrease in the thickness of a two-interface film beyond L_{max} does not lead to an increase in the SE sensitivity. The value L_{max} decreases if the integration time decreases. For instance, if the integration time decreases to 3 s, 2 s, and 1s, then L_{max} takes on values 45, 37, and 26 μm, respectively. L_{max} thickness is the maximum thickness of a sensing film which provides conditions under which response time t_{100} equals expose time t^n.

From Fig. 3.51, the calculated SE sensitivity can be increased, independently of the sensing film thickness and the number of interfaces, if the measurement exposure time is prolonged. If different SEs consisting of sensing films of different thickness provide the same response value, i.e., films of different thickness marked in the figure as L_{65} provide response R=65%, then the sensitivity of these SEs may be equal too, due to different response times of these SEs. For example, SEs containing one- and two-interface sensing films, whose thickness is 43, 61, 73, and 105 μm, which are capable of providing 65% response (See Fig. 3.50), have the same sensitivity of 3.7; response time t_{65} of these SEs is different and equals 1 s, 2 s, 1 s, and 2 s, respectively. If SEs consist of sensing films of equal thickness and have the same response time, but provide different responses, then their sensitivity is different. For example, SEs containing 61 μm sensing films and providing different responses 65% and 77%, at the response time t_{65}=1 s, have different sensitivities – 2.8 and 4.2, respectively, because their sensing films have a different number of interfaces.

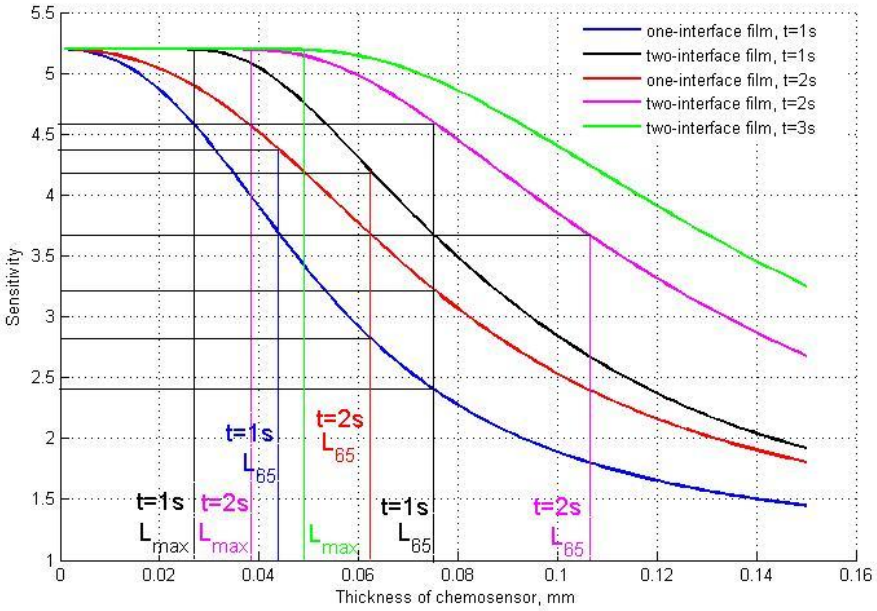

Figure 3.51. Calculated dependence of the SE sensitivity on the thickness of its sensing film and integration time.

Multi-film SEs. Fig. 3.52 demonstrates the advantage of a multi-film SE as compared to a single-film SE. If the number of interfaces and the thickness of sensitive films in a multi-film SE and a single-film SE are equal, then, in terms of oxygen concentration, these SEs have equal sensitivity and provide the same response because these parameters are determined by the thickness of these films and do not depend on the number of sensitive films the SE contains. However, in terms of the intensity of fluorescence signals, the response of a sandwich-structured SE increases when the number of sensitive films in the sandwich structure increases. Due to the increased signal intensity, the signal-to-noise ratio of the OOS, employing a multi-film SE, is higher. If a multi-film SE consists of thinner sensitive films than the film employed in a single-film SE, then the multi-film SE sensitivity is higher because it is determined by the thinner sensitive films. Thus, if two OOSs have similar optical design configurations and their SEs are of equal thickness, then these OOSs provide equal intensity of the fluorescence signal; however, the OOS with the multi-film SE is more sensitive than the OOS with the single-film SE because each sensitive film of the former are thinner than a single film.

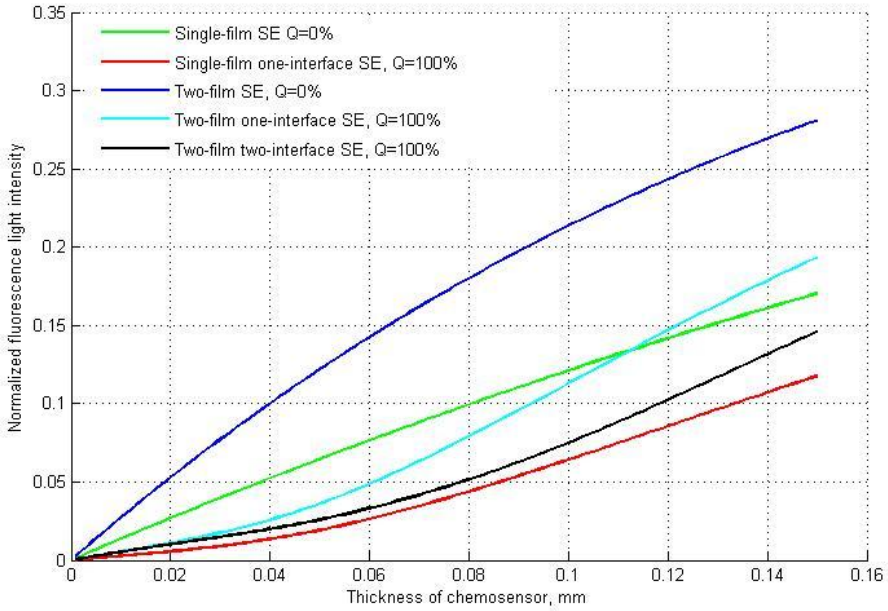

Figure 3.52. Dependence of fluorescence signals on the number and thickness of sensing films.

Advantages of two-interface SEs. On the whole, an increase in the thickness of a sensing film of a single-film SE results in the SE sensitivity decrease. The only exception to this rule is observed for the two-interface sensing film which is thinner than L_{max}, which allows us to obtain a higher fluorescence signal by increasing the sensing film thickness until this increase starts decreasing the SE sensitivity. For example, Fig. 3.51 demonstrates that a two-interface single-film SE provides a constant 5.2 sensitivity and a $t_{100} \leq 1$ s response time whereas its sensitive film thickness varies from 0 to L_{max}=26 μm. Fig. 3.53 shows that, due to an increase in the sensing film thickness up to 26 μm, a normalized fluorescence signal can be increased to I_{max}=0.1. If an SE provides a $t_{100} \leq$ 3 s response time and a constant 5.2 sensitivity, then the sensing film thickness can be increased to L_{max}=37 μm, thus increasing the normalized fluorescence signal to 0.16.

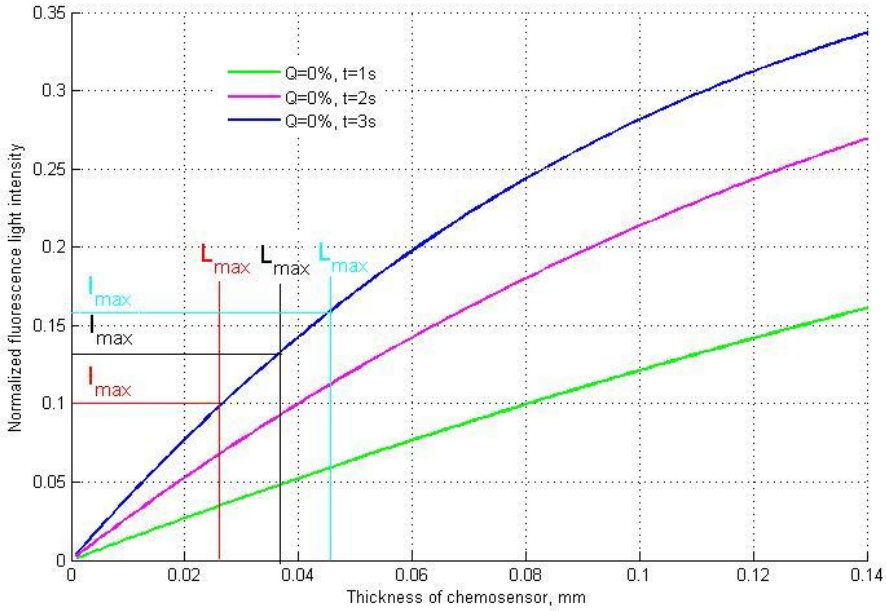

Figure 3.53. Advantages of the two-interface sensing film.

3.9.3. Novel optical design configuration of the OOS. Analyzing the results obtained during experiments with my analytical model, I came to the conclusion that an SE sensitivity can be increased not only by decreasing the thickness of employed oxygen sensing films, but also by using a novel optical design configuration. Fig. 3.54 demonstrates a novel optical design configuration, where a single-film SE cross section is illustrated schematically. According to this configuration, the light falling on the SE is perpendicular to the direction of oxygen diffusion, i.e. it spreads parallel to the film surface. The photo-detector is located either orthogonally to one or both of the sensing film surfaces, or in parallel with the film surface, across from edges, so that excitation light is directed toward the photo-detector. In conventional optical design configurations shown in Fig. 3.44, light is perpendicular to the surface of its sensing film, i.e. in the direction of diffusion.

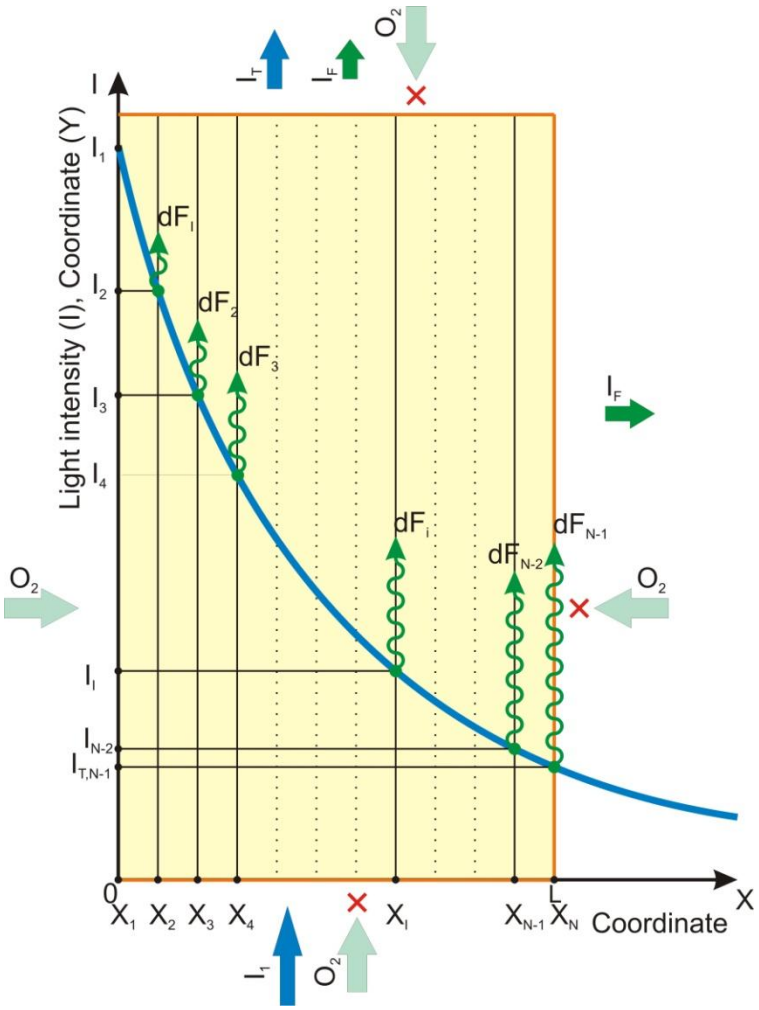

Figure 3.54. Schematic illustration of a single-film SE: a novel optical design configuration.

The length of the sensing film used in the OOS as a sensing element, where a novel design configuration is employed, cannot be considered infinite because, with an increase of the length, the intensity of the excitation light propagating along the film is decreasing, which results in the decrease of fluorescence emission. Due to this, the film length cannot exceed its thickness to a great extent. As the film thickness is considerable, we cannot neglect oxygen diffusion near the edges of the sensing film, and have to take into account different shapes of sensing film, in which case we will no longer be dealing with a film, but a sensing element of a different shape. The work on the model of a sphere-shaped SE is in progress. Below, I will consider a simplified model, where an SE is presented as an (*H*-long by *L*-thick) plane sensing film, in which I neglect oxygen diffusion near the edges of the film. As mentioned above, a film may have one or two interfaces. I focused my study only on a two-interface sensing film, assuming that results of a one-interface sensing film will not be principally different.

Let us assume that the left surface of the sensing film is located at x=0, and the right at x=L, with one end of the film located at y=0 and the other at y=H. The sensing film is divided into *N-1* layers of minute *dX* thickness. Oxygen concentration distribution Q_i^n in the sensing film is calculated, using Eq. 3.41-Eq. 3.46. To calculate the intensity of light directed perpendicular to

these layers, we also suppose that the sensing film is divided into *N-1* layers of minute *dY* thickness. The intensity of fluorescence light emitted by a layer I_{FTi} is calculated, using Eq. 3.30, in case the illuminator and the photo-detector are located on the opposite sides of the film. If the illuminator and the photo-detector are located on the same side, Eq. 3.31 is used. The film emission light intensity I_F is calculated as the sum of contributions I_{FTi} of all *N-1* layers, using Eq. 3.32. To study the intensity of fluorescence light emitted in the presence of oxygen, a film is divided into (*N-1*) x (*N-1*) cells, formed by these intercrossing layers. If *i* is the number of the layer, whose thickness is *dX*, and *j* is the number of the layer, whose thickness is *dY*, then, in the presence of oxygen, the intensity of fluorescence light emitted by a cell located in both of these layers can be calculated, using the Stern-Volmer equation:

$$I_{Qij}^{n} = {I_{Fj}}\Big/{(1 + K_{SV} Q_i^n).} \qquad (3.47)$$

If the photo-detector is located near the film edge, the contribution of cells located in layer *j* is calculated, using Eq. 3.36, where *dX* and *i* are replaced with *dY* with *j*, respectively. If the photo-detector is located on the side of the film, the contribution of cells located in layer *i* is calculated, using Eq. 3.37. The intensity $I_{QF}{}^{n}$ of fluorescence light, emitted by the film in the presence of oxygen, is calculated as a sum of cell contributions:

$$I_{QF}^{n} = \sum_{j=1}^{N-1} \sum_{i=1}^{N-1} I_{Qij}^{n} \qquad (3.48)$$

A single-film SE's sensitivity and response can be calculated, using Eq. 3.39 and Eq. 3.40, respectively.

Fig. 3.55 illustrates the SE sensitivity dependence on the film's thickness and length, if the photo-detector is located on the opposite side of the film end, across from the illuminator. The comparison of graphs presented in Figures 3.51 and 3.55 demonstrates that the sensitivity of existing conventional OOSs can be increased, if the novel optical design configuration is used, by merely increasing the sensing film's length; however, the response of the OOS is 5-10 times lower than that of the OOS which employs a conventional single- or double-sided optical design configuration. If the photo-detector is located on any side of the film, then the OOS sensitivity increases, but to a less degree than in the above-described case, and the response remains the same. (See Fig. 3.56).

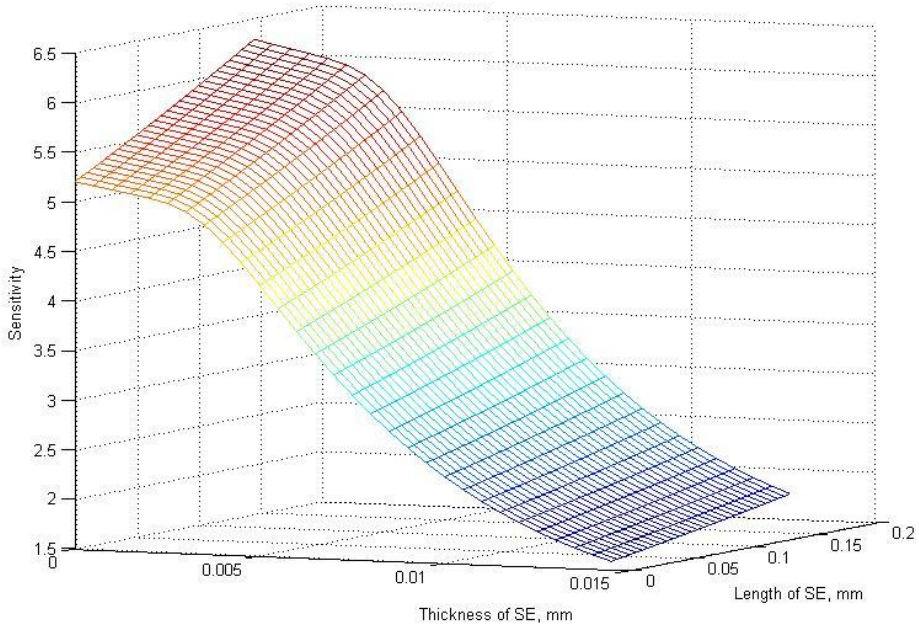

Figure 3.55. Calculated dependence of the SE sensitivity on its sensing film's thickness and length for the photo-detector located at the edges of the sensing film.

A novel optical design configuration may increase both SE sensitivity and response if techniques, based on the excitation of oxygen sensing materials by the evanescent field of the guided excitation light, are used. If two planar oxygen sensing films are located close to each other, then, due to the total internal reflection of the excitation light propagating between them, an evanescent field, inducing additional fluorescence emission, appears. In Fig. 3.56, our novel optical design configuration is compared with its analogs, which comprise a waveguide providing the excitation of an oxygen sensing layer. As the evanescent field is capable of exciting fluorophores residing within the immediate distance (100-200 nm) from the surface of an oxygen sensing layer, the sensing layer employed in the known optical design configurations is rather thin and, hence, the layer edges cannot be used to couple excitation light into and fluorescence light out of the layer. In contrast to analogs, in our novel optical design configuration, the layer, which in our case is an oxygen sensing film, is thicker so that the edges could be used to excite fluorescence. And, secondly, the usage of multiple films allows us to increase SE response.

As any new design configuration, our novel optical design configuration opens up an opportunity to generate multiple embodiments of new SEs. According to one of these embodiments presented in Fig. 3.57, an SE can comprise two or more SEs, located one after another; one of which is shown in Fig. 3.56c. The sensing film edges of the first SE are facing the waveguides of the second SE, to decrease the attenuation of the fluorescence signal emitted by the first SE. The waveguides of the first SE are facing the edges of the second SE, to increase the effectiveness of the excitation light power. By using an increased number of SEs, we thus increase the total SE length and, consequently, its sensitivity.

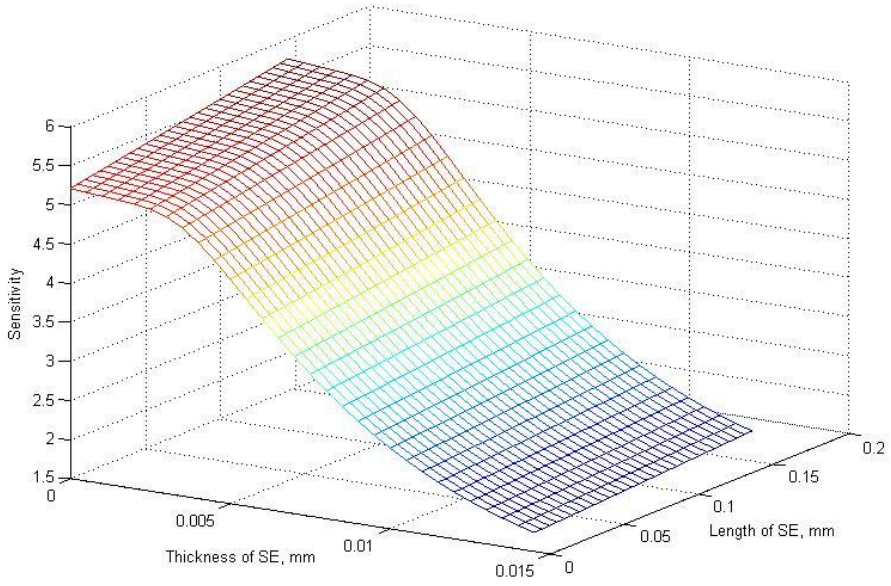

Figure 3.56. Calculated dependence of the SE sensitivity on its sensing film's thickness and length for the photo-detector located at the side of the sensing film.

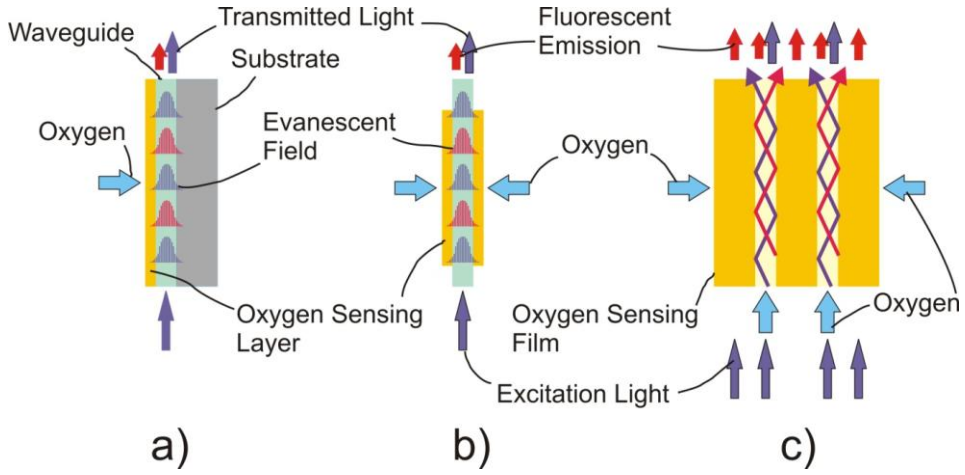

Figure 3.57. Comparison of the novel optical design configuration with its analogs: a) Design configuration of a planar sensor; b) Design configuration of a fiber-optic sensor; c) Novel optical design configuration.

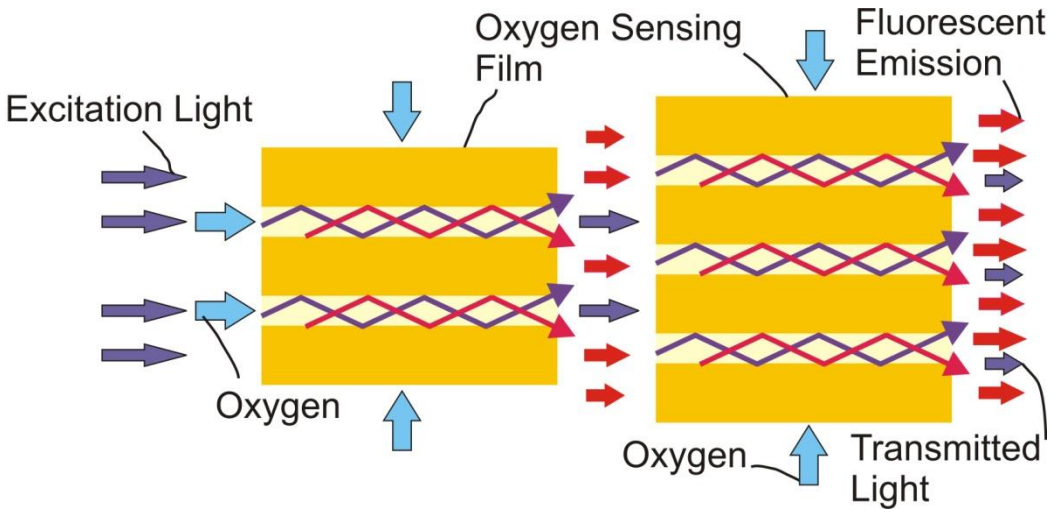

Figure 3.58. Embodiment of the SE.

3.10. Results and Discussion

I have presented a functional prototype of a non-fiber optic OOS, which is based on fluorescence quenching, and which benefits from the robustness of a non-fiber optic design configuration and the simplicity of a double-sided optical configuration. The intensity-based measuring technique provides a possibility to minimize the number of electronic components in the OOS and helps avoid using sophisticated and expensive instruments. Notwithstanding the fact that the OOS employs a low-cost and a small-size photo-detector, illuminator, and filters and operates without employing any lens or lens system, the parameters of the OOS, based on this prototype, can be well-suited for monitoring oxygen concentration in a wide circle of applications.

According to my analytical model of an OOS, which is based on fluorescence quenching, a single-sided optical design configuration provides a higher intensity of fluorescence signal, as compared to a double-sided optical design configuration in case the sensing film, employed in the OOS, is rather thick. In order to provide an appropriate OOS response time, sensing films should be rather thin. If the sensing film's thickness is less than 0.1 mm, then both design configurations provide equal intensity of fluorescence signal. As mentioned before, one of disadvantages of a double-sided configuration is a necessity protect the photo-detector from a higher level of stray excitation light, using a precise barrier filter, which can result in the increase of an OOS size and cost. This disadvantage has been overcome by using two inexpensive thin-film Roscolux Color Filters as the barrier filter. This, and the configuration simplicity, justified our selection of a double-sided optical design configuration.

I detected experimentally that our OOS sensitivity could increase by using a sandwich structure of our sensor element, consisting of two RedEye patches, although, our analytical study demonstrated that such structure, if it consists of similar sensing films, could merely lead to a higher dynamic range, without an increase of OOS sensitivity. According to my analytical model, an increase of OOS sensitivity can be achieved if, at least, one sensing film in the sandwich structure is thinner than the sensor element, where a single film is used, and if the exposure time in measurements, where differently structured sensor elements are used, is equal. As OOS sensitivity increased even in the case of employing different RedEye patches, the

difference in the thickness of the patches was not the reason for increased sensitivity observed in our experiments. Another assumption why OOS sensitivity increased was an increase in the exposure time during experiments. By using two RedEye patches, we increased the dynamic range in our fluorescence measurements, due to which we were able to observe the changes in the photo-detector output signal during its stabilization for a longer period of time, as compared to the measurements, where one RedEye patch was used and fluorescence signal was weaker. As a result, the sandwich structure containing two RedEye patches allowed us to prolong exposure time, owing to which OOS sensitivity increased.

The examination of temperature effects on the OOS response showed that we can neglect the contribution of sensor element temperature dependence to overall temperature effects, i.e., the RedEye patch employed in our OOS is nearly independent of temperature. The major contribution to the overall temperature effects on the OOS response is the temperature dependence of LED optical power, which can be effortlessly calculated and taken into account to correct measurement results. OOS sensitivity does not depend on the wide-range operating current passing through the LED; however, it sharply decreases when the current falls below 0.2 mA. Although a decrease in the operating current allowed us to reduce OOS power consumption, it led to increased temperature effects on measurement results. Our future work toward improving the OOS prototype should include LED optical power stabilization and correction of measurement results.

The modification of the Stern-Volmer equation by using the data obtained from measurements in two additional calibration points allows us to determine oxygen concentration at different temperatures without a correction of the Stern-Volmer constant.

Chapter 4

Development of a Fluorimeter for Detecting Upconverting Fluorescent Materials

4.1. Prior Art

A fluirometer is a device used to measure fluorescence parameters: emission light intensity and emission excitation wavelengths. Typically, a fluorimeter, whose schematic diagram is shown in Fig. 4.1, includes a light source producing excitation light, an excitation and emission wavelength selectors, a sample compartment, a photo-detector of emitted fluorescence, and signal processing instrumentation [1, 21,[4] 102, 103]. Depending on the photo-detector's spectral response, the fluorimeter may also include a barrier filter, to block the stray excitation light that can get into the photo-detector.

[4] The endnotes are to be found on pp. 108-116.

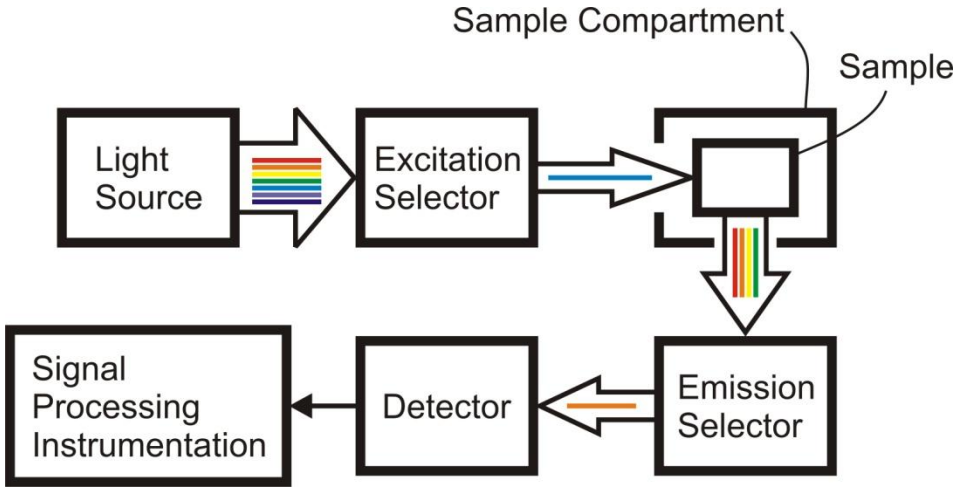

Figure 4.1. Schematic diagram of a fluorimeter.

The light source, which is typically a xenon lamp, produces excitation light of a broad spectrum, ranging from 200 to 900 nm. The output power of xenon lamps used in general-purpose fluorimeters is 150-175W. The excitation wavelength selector transmits light in a narrow band, centered about a specified excitation wavelength. The transmitted light passes into the sample, positioned in the sample compartment, causing fluorescence emission of fluorophores within the sample. Depending on the optical configuration of the fluorimeter, the emitted light is collected at 45^{o} or 90^{o}, with respect to the excitation axis, after which it enters the emission selector. The emission selector transmits to the photo-detector, which is typically a PMT, a narrow band of this light centered about the specified emission wavelength. The PMT output is amplified and processed by signal processing instrumentation, to create voltage proportional to the intensity of the light transmitted by the emission selector. The measured fluorescence intensity is represented as a function of excitation and emission wavelengths, called a fluorescence spectrum.

Currently, researchers have at their disposal two basic types of fluorimeters, the filter fluorimeter and the spectrofluorometer. While the filter fluorimeter uses optical filters to select the wavelength of incident light, the spectrofluorometer uses a monochromator grating [1]. As a result of light dispersion caused by the grating, a smaller amount of light passes to the detector, as compared to the light that passes a filter. Thus, out of the two, the filter fluorimeter provides more sensitive measurements. Filter fluorimeters are easier to handle and are less expensive than spectrofluorometers; however, spectrofluorometers are more versatile than their counterparts. In addition, filter fluorimeters are more effective while performing sensitive quantitative and qualitative measurements, detecting, and studying the behavior of substances with known molecules.

For analyzing uncomplicated fluorescent molecules, a conventional single-emission or single-excitation 2D spectrum can be sufficient. As regards to complex multi-component samples, mixtures, as well as microenvironments, 3-D spectra are preferred. Due to the fact that each single fluorescent component's spectrum is subject to interferences from other fluorescent components' emission;, the spectrum of a sample consisting of several components suffers from several overlaps. More detailed information can be obtained by scanning both excitation and emission wavelengths, to acquire a 3D spectrum [12-16]. Major limitations of most commercial

fluorimeters include their slow-speed mechanical wavelength selectors, as well as their high cost. As a result, spectrum acquisition is a time-consuming process due to the necessity to perform mechanical scanning across the excitation and emission wavelength ranges. The insufficient scanning speed is unacceptable if the spectral wavelength range needs to be increased and the wavelength increment needs to be decreased, especially in case of dealing with a multidimensional spectrum. Among the disadvantages of mechanical scanning systems is limited wavelength reproducibility, resulting from insufficient precision of the moving parts of the scanning mechanism. Additionally, different elements of EEM, produced as a result of slow scanning, are measured at different points in time and represent different samples, if this sample's characteristics change during the data acquisition period [13]. The high cost is still another drawback of commercial fluorimeters that makes them unaffordable for many laboratories.

Researchers of the Optoelectronic Sensor Laboratory at Stony Brook University have designed a versatile, robust, and inexpensive filter fluorimeter that employs a broadband light source, as well as linear interference filters used as excitation and emission wavelength selectors. The positioning of both filters is regulated by two computer-controlled linear step motors [11]. Along with the advantages obtained as a result of the implementation of linear interference filters, instead of monochromators which are typically used as excitation and emission wavelengths selectors, the designed fluorimeter has the same major limitation originating from a need for a slow mechanical scan through excitation and emission wavelengths. Therefore, 3D spectrum acquisition, using this type of fluorimeter, is time-consuming.

To conduct measurements which require a high-excitation power source, capable of illuminating a rather small-sized sample, or part of a sample, and producing rather short excitation light pulses, or propagating excitation light over large distances, may require the use of a laser light source, e.g. an inexpensive laser diode (LD). However, due to the narrow bandwidth of fixed-wavelength lasers, these lazers can be used as a light source in such fluorimeters which are capable of measuring only a 2D emission spectrum obtained by exciting a sample by a fixed wavelength. U.S. Patent 5,049,738 [104] describes an EEM fluorimeter employing a tunable laser, used simultaneously as a light source and an excitation-wavelength selector (See Fig. 4.1). The wavelength switching time of tunable lasers is less than 1 ms, and can be as small as a few nanoseconds. The fluorescence emission selected by a monochromator is detected by a single-channel PMT. The use of tunable lasers in fluorimeters makes them less complex by excluding the element used for excitation-wavelength selection. Unfortunately, tunable lasers are still rather expensive. The decrease in the EEM acquisition time provided by this fluorimeter is still limited by the need for a slow mechanical scan across emission wavelengths by the monochromator.

One of the known solutions to avoid the mechanical scan across emission wavelengths is using a charge-coupled device (CCD), a diode array detector, a multi-channel PMT, or any other multi-channel detector coupled with a dispersive element, which is capable of working simultaneously as two elements of the schematic presented in Fig. 4.1: the emission-wavelength selector and the detector. Fluorimeters with multi-channel detectors are capable of obtaining the entire emission spectrum in a single measurement. An example of such a solution is disclosed in paper [105], where a portable fluorimeter employs an LED as a light source and a CCD as an emission-wavelength selector and a detector. However, such fluorimeter does not comprise an excitation-wavelengths selector, and is capable of measuring only 2D emission spectra.

A fluorimeter for a single-measurement EEM acquisition allows researchers to reduce the time required for scanning 3D spectra as well as reduce the number of errors caused by photo-bleaching and limited wavelength reproducibility. A fluorimeter, capable of obtaining an EMM in a single measurement, consists of a short-arc lamp, producing broad and intense excitation light within the range of 250-600 nm, and two spectrographs. One of the spectrographs is used to create spatially separated emission spots in a uniform sample. These fluorescent spots are projected onto the entrance of the other spectrograph equipped with a CCD camera [13]. The entire EEM spectrum can be recovered from 2D data obtained from a CCD camera, using one of deconvolution algorithms, e.g., the Parallel Factor Analysis [106, 107]. The recovery of the spectrum without distortions is possible if immaculate imaging optics is used to provide spatial separation. One of the disadvantages of single-measurement EEM fluorimeters is the necessity to comply with stringent requirements for imaging optics, the noncompliance with which may cause spectral distortions. Another disadvantage is the necessity for conducting numerous calculations to extract EEM from a 2D dataset, using a deconvolution algorithm for calculating pure excitation, emission and concentration profiles.

Rapid development of nanotechnology led to the synthesis of high-quality rare-earth-doped upconverting (UC) nanoparticles which have a relatively narrow-bandwidth emission and exceptional photostability as compared to those in traditional fluorescence materials. Alongside the existing remarkable characteristics of UC nanoparticles, new, no less extraordinary, properties have been reported over the past decade. For instance, in the paper [17] on the control of the two-color emission in upconverting $NaYF_4:Er^{3+},Yb^{3+}$ nanoparticles, the authors state that if the mentioned particles are excited by light at 980 nm, with the power densities around 8 W/cm^2, and on condition that the excitation frequency is increased from 10 Hz to 100 kHz, the ratio of green to red in the emission is decreasing from ~1.4 to 0.28. In the paper [18] on the dependence of fluorescence intensity in $NaYF_4,Yb^{3+},Er^{3+}$ nanoparticles on the excitation power, it was reported that above the following power densities – 4800 W/cm^2 for purple fluorescence, 5700 W/cm^2 for green, and 7100 W/cm^2 for red, the UC emission intensity begins a reversal, i.e., fluorescence intensity is decreasing when power density is increasing. If these characteristics are not taken into account, the ratio of the intensities of measured colors will be different, depending on the power density or modulation frequency of excitation light, which leads to the incomparability of results presented in the literature. Such results can vary even if the experiments were conducted using the same setup as it may be challenging to determine the exact power density of the laser beam traveling through the optical system of an instrument and the matrix with encapsulated UC nanoparticles at the moment it reaches these nanoparticles [108].

Researchers dealing with UC material applications require dedicated fluorimeters with specific properties. Specifically, the spectral range of these fluorimeters, as compared to that in fluorimeters designed for traditional fluorescent materials, must be expanded so that it would include the near-infrared (NIR) region, the excitation light source must provide a higher power density, and the detector must provide superior sensitivity and a marginal noise level. Because the fluorescence efficiency of some UC materials is rather low due to the multi-photon absorption mechanism of UC fluorescence, the preferred light source will be a laser as it provides a coherent excitation beam that can easily be focused on a small area compared to broad-band lamps commonly used in commercial fluorimeters. However, as it was mensioned below, fixed-wavelength lasers are not suitable for fluorimeters whereas tunable lasers producing a rather wide NIR range wavelengths are expensive. While selecting a photo-detector, a PMT

will be favored over silicon-based diodes, such as a photodiode or a CCD, due to such outstanding characteristics of the PMT as an extremely high gain, a low signal-to-noise ratio, and a low response towards NIR excitation. The main limitation to commercial fluorimeters, employing a single-channel PMT, is the need of mechanical scanning across the excitation and emission wavelength ranges using appropriate wavelength selectors resulting in extending the spectrum acquisition time. The time for performing mechanical scans to acquire a 3D spectrum becomes unacceptably great as compared to that necessary to acquire a conventional 2D single-emission or single-excitation spectrum, let alone a 4D or even a 5D spectrum, when additional dimensions, such as excitation light power density and modulation frequency, should be processed. The task of reducing the time to obtain a spectrum can be solved by acquiring a spectrum in a single measurement.

In this chapter, I present a functional prototype of a novel fluorimeter employing a set of individually controlled LD as excitation sources. The fluorimeter's design enables a rapid scan of excitation wavelengths by switching LDs one by one and, thus, excitation wavelength selection is performed electronically. Due to low cost of LDs the designed fluorimeter has advantage over fluorimeters employed tunable lasers. The properties and performance of our prototype were demonstrated while authenticating objects marked with UC security markers. We also propose, by introducing basis EEMs and basis markers, an enhancement of the method for authenticating objects, which is based on the analysis of EEMs representing security markers. The given research is a continuation of our work on the development of the robust and compact EEM-fluorimeter described in our earlier paper [11]. I also present a conceptual design of a multidimensional fluorimeter which is based on our prototype and allows researchers to acquire a 3D spectrum in a single measurement. The multidimensional fluorimeter allows researchers to scan not only excitation and emission wavelengths, but also excitation light power density and modulation frequency, that is why, we called it a "hyper-fluorimeter". Spectra acquired using the hyper-fluorimeter by scanning power density of excitation light will allow us to facilitate the comparison of measurements of fluorescence of UC nanoparticles presented by different researchers.

4.2. Instrumentation

To measure UC fluorescence, commercial fluorimeters have to employ NIR lasers. While some of these fluorimeters are rather expensive because they are supplied with NIR tunable lasers, most of them still need to be supplied with a fixed wavelength laser, to adapted them to NIR excitation [109]. The key feature of our setup is the employment of a set of inexpensive laser diodes (LDs) each of which can be controlled individually. The sample can be illuminated by all the LDs simultaneously, or by a certain group of LDs, in which case, the switch can be done rapidly. The illuminating power, if necessary, can also be changed. The schematic of our experimental setup and the fluorimeter prototype used for the authentication of objects marked with UC tags are presented in Fig. 4.2 and 4.3, respectively.

Our fluorimeter prototype employs six QLT QPhotonics LDs supplied with collimator packages positioned with the help of six ball sockets and controlled by individual drivers. The ball socket joints allow the user to direct all laser beams at one spot on the surface of the object under test. Two additional LDs can be employed and positioned in extra two sockets. The spot illuminated by the collimated laser beam can be changed in size from 2 to 1 mm, using collimating lenses of the LDs packages. The operational wavelengths of the LDs are 911, 933, 948, 969, 975, and 1019 nm; the nominal optical output power is 100 mW; and the bandwidths

vary from 0.36 nm to 2.21 nm. To ensure the quality of the NIR excitation beams, a filter module with cut-on filters (Kodak Wratten Gelatin Filters No. 87) located along the laser beams is used. The filter's cut-on wavelength is 750 nm; its transmission coefficient is around 82%. In the initial prototype of our fluorimeter, the emission light wavelength's selection is provided by 7 band-pass filters from Edmund Optics VIS Filter Kit. The filters are installed in the Edmund Optics Motorized Filter Wheel IFW. The filters are centered at 400, 450, 500, 550, 600, 650, and 700 nm (±10 nm).

The conventional front-side (45/0) measuring geometry is used for arranging the laser diodes 2 and the photon counting head 13 used as a detector. The 45-degree angle of incidence has been selected in order to minimize the excitation wavelength interference by reducing the fraction of the excitation light reflected from the surface of the illuminated object 1 and by it deflecting it from the collecting lens 6. However, different measurement geometries can be more appropriate, depending on the fluorimeter application. The holder of the C-Mount tube used to connect the collecting lens and the filter wheel effortlessly, the holder of objects under test, which are standard slide frames containing marked paper sheets, and the ball sockets used to position laser beam spots on the object surface are printed in one piece by a 3D printer.

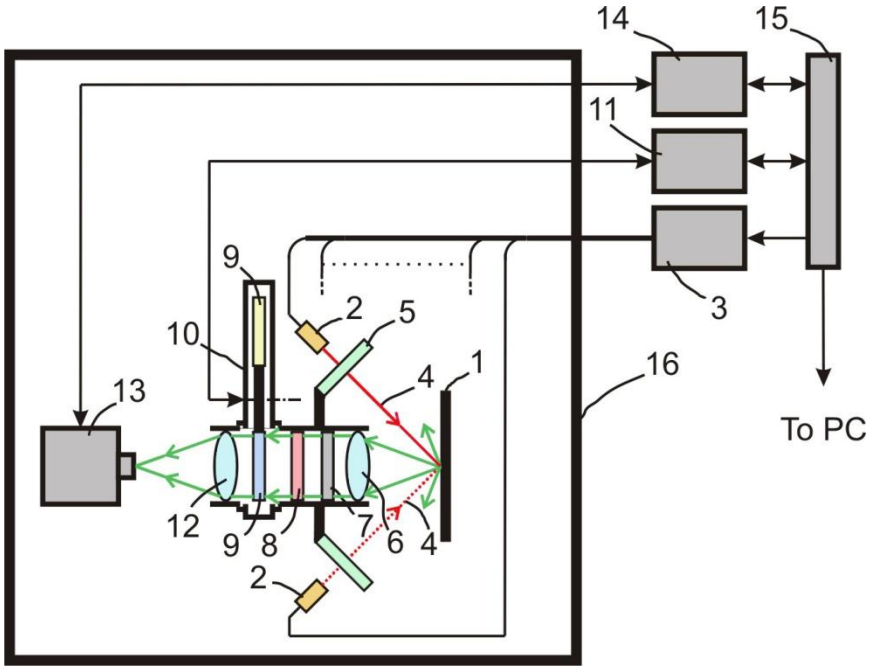

Figure 4.2. Schematic of an experimental setup: (1) Object with security marking. (2) Laser diodes. (3) Laser controller. (4) Laser beams. (5) Module with visibly opaque filters. (6). Lens collecting fluorescence light. (7) Neutral density filter. (8) Barrier cut-off filter. (9) Band-pass filters. (10) Filter wheel. (11) Filter wheel controller. (12) Focusing lens. (13) Photon counting head. (14) Photon counter. (15) USB Hub. (16) The dark chamber.

Band-pass filters, selected using the filter wheel 10, pass 20 nm bands of wavelengths selected from the collected light. As a rule, UC fluorescence intensity is not strong; therefore, the intensity of the excitation stray light that is reflected from the object 1 and that passed the band-pass filter 9 cannot be fully suppressed and remains as high as that of UC fluorescence. To permit only the selected emission wavelengths to pass toward the detector 13, we use a barrier

filter 8 installed before the filter wheel 10 with band-pass filters 9. The focusing lens 12 directs the filtered light into the window of the Hamamatsu photon counting head H17155 used as a detector 13 connected to a custom-designed photon counter 14 [110]. In the case of a high-signal intensity is being measured, we use a neutral density filter 7, to prevent the counter's overflow.

The counter 14, Motorized Filter Wheel controller 11, and laser controller 3 are connected to a PC through a USB Hub 15. Our LabVIEW software was used to provide, according to our test plans assigned through the User menu, the commutation of LDs, the selection of filters and exposition time. The dark chamber 16 allows us to conduct experiments under ambient-light conditions.

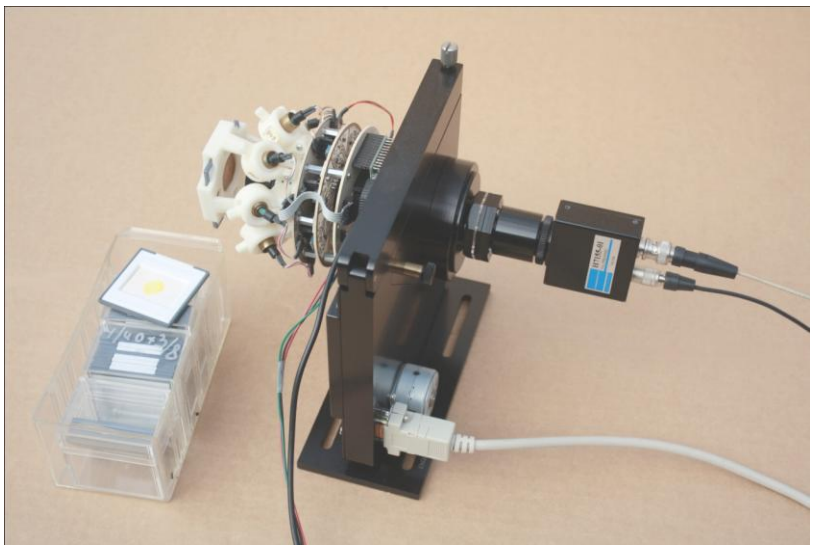

Figure 4.3. Fluorimeter prototype used for the authentication of objects marked with UC tags.

4.3. Method

The authentication of objects marked with fluorescent dyes is based on the analysis of an EEM [11]. Further, if our detection equipment is capable of identifying at least one peak of the SM spectrum, we will call a fluorescent dye a security marker (SM), and a mixture or a combination of SMs used to mark protected objects – a tag. A unique combination of 3D spectrum peaks in a tag applied to a protected genuine object serves as the object's ID. The authenticity of an object is validated by comparing the EEM representing the 3D spectrum of the tag applied to the object with the EEM representing a certain sample tag from the catalogue created while conducting preliminary experiments.

Acquiring spectra and designing an EEM. According to the EEM method, the data of scanned excitation and emission wavelengths are combined into the m x n size EEMs. A matrix row i $(i=1, 2, \ldots, m)$ represents an emission spectrum measured at a fixed excitation wavelength y_i. The number of matrix columns n is equal to the number of measurement points that are necessary to obtain an emission spectrum. A matrix column j $(j=1, 2, \ldots, n)$ represents an excitation spectrum measured at a fixed emission wavelength x_j. If in an EEM, we can find any nine adjacent elements where the middle element's fluorescence intensity value is greater than the values of its eight neighbors each, then we will define this middle element as a peak. Thus,

between two elements which define two peaks, there exists at least one other element, whose intensity value is less than the values of the elements defining these peaks.

Let us suppose that a 3D cone-shaped fluorescence spectrum (with excitation and emission wavelength increments of 1 nm) of a mixture of three UC SMs is obtained using a fluorimeter. Fluorescence light intensity was registered by a detector capable of measuring minimal detectable fluorescence intensity I_{min} (See Fig. 4.4). Having obtained emission spectra, we are able to combine the measurement results into a fairly large (108 x 300) EEM (not shown in the figure). Values of certain EEM's elements define peaks whose wavelengths can be considered sufficiently reliable because they are obtained with small increments. Henceforth, we will call these peaks "original peaks." However, since a rather substantial number of measurements are required to obtain the (108 x 300) EEM, the process of spectrum acquisition is time-consuming. The spectrum acquisition time can be reduced by increasing the wavelength increments, in which case we will analyze a smaller size EEM. Values of certain elements of a smaller-size EEM, similarly to the case with the larger-size matrix, also define peaks. However, these peak wavelengths may not always coincide with original peak wavelengths, i.e., the values of a smaller-size EEM define locations of certain original peaks in a distorted way. In order to distinguish original peaks from peaks defined by smaller size EEMs we will call the latter "peak images".

Fig. 4.4 demonstrates a 6 x 7 EMM, which we will further call matrix *A*, which represents the spectrum of the above-mentioned mixture of three SMs. The EEM elements $A_{yi,xj}$ are represented in Fig. 4.4 as small white circles in the nodes of the grid, with the horizontal lines corresponding to excitation wavelengths, and the vertical lines corresponding to emission wavelengths. White circles with black dots inside indicate the positions of peak images. The positions of original peaks are shown as large dots. The shape of any peak is defined by fluorescence intensity values of the elements of the EEM representing a spectrum. The shape of original peaks shown by thick solid lines is defined by the 108 x 300 EMM elements, which are not represented in the picture, while the shape of the peak images shown as thick dashed lines is defined by the elements of matrix *A*. The figure demonstrates that not only the shapes of peak images can differ from the shapes of their original peaks, but also the images' peak wavelengths can differ from the peak wavelengths of the original peaks. Because every identified peak image corresponds to only one original peak, this peak image can be used for object authentication in the same manner as the original peak.

The left original peak in Fig. 4.4 has no peak image, cannot be identified by analyzing matrix A, and cannot be used as a SM. The matrix elements $A_{975,450}$ and $A_{969,450}$ related to the unidentified peak image are located outside the circle contour representing the minimal detectable fluorescence intensity's level I_{min} and, i.e., these elements are considered to equal zero. To identify this peak image and use SM_1, the wavelength increment or the minimal detectable fluorescence intensity I_{min} of the detector should be decreased.

The middle peak representing the spectrum of SM_2 can be identified because the matrix element $A_{975,500}$ equals I_{min}, i.e. its fluorescence intensity can be measured by a detector. If several neighboring EEM elements relate to the same peak image and are located inside the circle counter of level I_{min}, the peak image's shape becomes more complex. For example, the right peak's image representing the spectrum of SM_3 and defined by two elements – $A_{948,650}$ and $A_{933,650}$ – obtains an additional plane shown as thin dashed lines in Fig. 4.4.

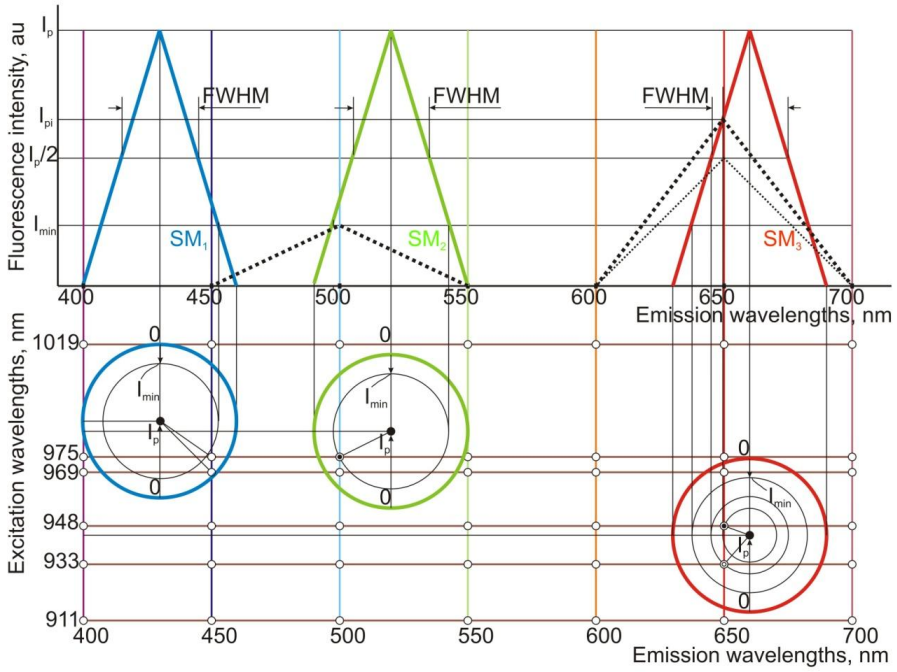

Figure 4.4. A grid representation of an EEM: Peak images defined by an EEM can be used to identify their original peaks.

As a rule, the intensity of the peak image I_{pi} is lower than the intensity of the original peak I_p. Assuming that the spectral bandwidth of laser diodes and band-pass filters is negligibly small as compared to full width at half-maximum (FWHM), the intensity of a peak's image could be estimated by the equation:

$$I_{pi} = I_p \cdot \left(1 - {}^{r}/_{FWHM}\right) \qquad (4.1)$$

where r is the distance between the original peak (x_p, y_p) and its image (x_{pi}, y_{pi}), in nm, x_p and y_p are peak wavelengths of the original peak which are defined by a large-size EEM, and x_{pi}, aand y_{pi} are peak wavelengths of the original peak's image which are defined by a small-size EEM *A*. The intensity I_{pi} increases with the decrease of the distance r, i.e., when x_{pi}, and y_{pi} are selected closer to x_p and y_p .

To characterize a peak or a peak image defined by an EEM, we can use the four parameters: emission peak wavelength x_p, (x_{pi},), excitation peak wavelength y_p (y_{pi}), FWHM, and peak intensity $I_{p,}$ (I_{pi}). A spectrum peak can be defined if the fluorimeter's detector is rather sensitive, the marker's fluorescence intensity is sufficient (i.e. the marker's fluorescent material has a sufficiently high quantum yield and is taken in appropriate concentration), and the ratio of wavelength increments to FWHM is relatively small. To estimate the appropriate values of wavelength increments, we can use the simple inequality:

$$S_x^2 + S_y^2 \le 4 \cdot FWHM^2 \cdot \left(1 - {}^{I_{min}}/_{I_p}\right)^2 \qquad (4.2)$$

where S_x and S_y (in nm) are wavelength increments in the detection and excitation arms of the fluorimeter, respectively; I_p is the peak intensity defined by the larger EEM, measured in arbitrary units (au); and I_{min} is the minimal value of fluorescence intensity the detector is capable of measuring with a certain confidence level, in au. FWHM is defined using the larger EEM, in nm.

We can obtain more accurate estimations by taking into account laser diodes' spectral bandwidths BW_L and pass-band filters' bandwidths BW_F, and modify all of the above mathematical expressions. For instance, the modification of Eq. (4.2) allows us to increase the estimated values of maximally allowable wavelength increments S_x and S_y:

$$(S_x - BW_F)^2 + (S_y - BW_L)^2 \leq 4 \cdot FWHM^2 \cdot (1 - {I_{min}}/{I_p})^2 \quad (4.3)$$

EEM Digitizing. Verification of an object's authenticity can involve the comparison of multiple EEMs, which is tedious, especially if the verification is required in case of mass production. Moreover, due to fluorescent intensity measurements' variance caused by instrumental noise and measurement errors, the comparison of EEMs representing even the same combination of SMs may present a difficulty. Therefore, in order to simplify our comparison, we will consider only peak wavelengths of the compared spectra because they not change with fluorescent intensity measurement variance, and will ignore the information about peak shapes, i.e. we will be comparing only the elements of EEMs defining peaks and will ignore all other elements. This can be achieved by "digitizing" our EEMs through finding EEM elements representing peaks and setting them at 1, while all other EEM elements will be set at zero. Any two 3D spectra are considered to be identical if digitized EEMs representing these spectra are equal. In case digitized EEMs are compared manually, these EEMs can be represented as grids with shaded areas adjoining the elements defining peaks (See Fig. 4.4). The comparison of the location and configuration of the shaded areas on the grids representing these EEMs will be sufficient for comparing EEMs.

Basis SMs. The spectrum of an UC SM generally has several peaks, some of which may coincide with certain peaks in another UC SM's spectrum. In spite of such coincidence, we can distinguish these spectra, and thus use these two SMs for an object's protection. However, if we use a set of several tags, the overlapping of their peaks may result in authentication errors. Authentication errors caused by such overlapping of peaks can be avoided if we create tags using SMs selected from a set of SMs, which we will further call "basis SMs". Taking into account that each SM is represented by an EEM which can be considered as a vector with components defined by the EEM's elements, we can define a set of basis SMs using the same approach that we use defining a set of basis vectors: not a single SM or a combination of SMs from the set of basis SMs can be represented by the same digitized EEM. The maximal number N of unique IDs, or the number of tags in the catalog created from m basis SMs is:

$$N = \sum_i^m C(m,i) = 2^m - 1, \quad (4.4)$$

where $C(m,i)$ is the number of combinations of basis markers taken i at a time.

We will demonstrate this approach in Fig. 4.5, using our running example. Let us suppose that not a single marker or a single combination of markers from the set of SM_1, SM_2, and SM_3 can be represented by the same digitized EEM, i.e. this is a set of three basis SMs. We will assume

that these SMs have only one peak each and, consequently, each SM can be represented by one basis vector **SM** whose magnitude equals the peak intensity. We can represent these vectors only by their magnitude if they coincide with the coordinate axes *x, y, z*. At a certain concentration of markers, e.g. c_{i0} (*i=1, 2,* and *3*), peak intensity reaches 1, in which case vectors $c_{i0}\mathbf{SM_i}$ will become basis unitary vectors. In practice, the c_{ij} (*i*=const, *j=0, 1*, …) concentration of basis SMs used to create a tag can vary; therefore, vectors $c_{ij}\mathbf{SM_i}$ (*i*=const) are different, and vector $\mathbf{Tag_j}$ representing the EEM of such a tag changes according to the equation:

$$\overrightarrow{\boldsymbol{Tag_j}} = \sum_i^{\mathrm{m}} \boldsymbol{c_{ij}}\,\overrightarrow{\boldsymbol{SM_i}} \qquad (4.5)$$

Due to various concentrations of markers employed in tags, and due to fluorescence intensity measurement errors, the verification of an object's authenticity by comparing EEMs representing even the same combination of SMs may present a difficulty. In Fig. 4.5, vector $\mathbf{Tag_1}$ (shown in blue in the color version) represents the EEM of a certain tag, and the components of the vector $c_{11}\mathbf{SM_1}$, $c_{12}\mathbf{SM_2}$, and $c_{13}\mathbf{SM_3}$ represent employed in this tag markers SM_1, SM_2, and SM_3, taken at concentrations c_{11}, c_{12}, and c_{13}, respectively. Vector $\mathbf{Tag_2}$ (shown in pink in the color version) represents the EEM of another tag; and its components $c_{21}\mathbf{SM_1}$, $c_{22}\mathbf{SM_2}$, and $c_{23}\mathbf{SM_3}$, represent the same SMs taken at different concentrations c_{21}, c_{22}, and c_{23}, respectively. Vector $\mathbf{Tag_2}$ is not equal to vector $\mathbf{Tag_1}$ because their components are different from which we conclude that these vectors represent different EEMs, notwithstanding the fact that these two contain the same SMs. Additional information processing is needed to come to the conclusion that these EEMs represent the same set of SMs and, thus, the tags can be considered similar. Different EEMs representing the same combination of the employed in a tag SMs, after these EEMs are digitized, become identical, and can be represented by the same vector **DTag**:

$$\overrightarrow{DTag} = \sum_i^n sign(c_{ij}\overrightarrow{SM_i}) \qquad (4.6)$$

where *sign* is a function defined as follows: *sign(x)=0* if *x=0* and *sign(x)=1* if *x>0*. Because vectors $sign(c_{ij}\mathrm{SM_i})$ are either basis unitary vectors $c_{0i}\mathrm{SM_i}$ or zero vectors, the number of variations of vector DTag is limited and can be calculated using Eq. (4.4). All concentration variations of the three basis SMs (*n=3*) can provide only *N=7* unique IDs (DTag=$c_{01}\mathrm{SM_1}$, $c_{02}\mathrm{SM_2}$, $c_{03}\mathrm{SM_3}$, $c_{01}\mathrm{SM_1}+c_{02}\mathrm{SM_2}$, $c_{01}\mathrm{SM_1}+c_{03}\mathrm{SM_3}$, $c_{02}\mathrm{SM_2}+c_{03}\mathrm{SM_3}$, and $c_{01}\mathrm{SM_1}+c_{02}\mathrm{SM_2}+c_{03}\mathrm{SM_3}$).

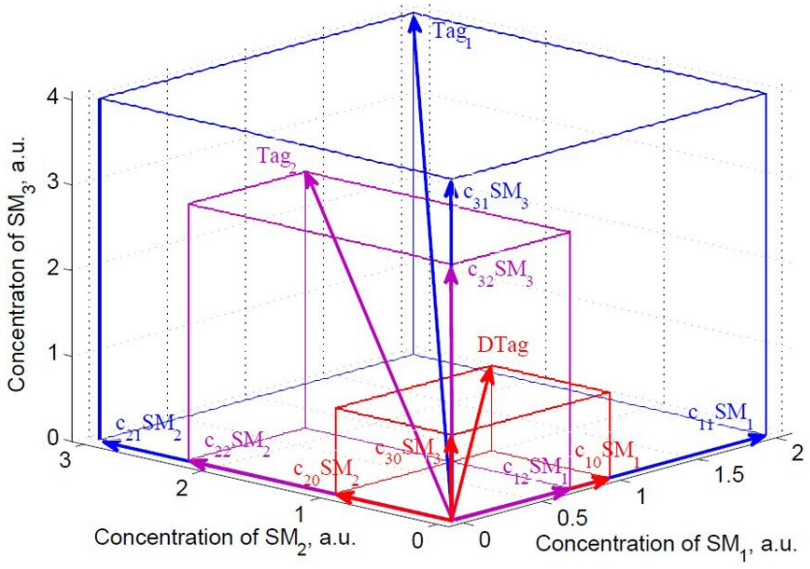

Figure 4.5. Vector representation of tags consisting of three basis SMs.

Basis EEM. As we mentioned above, a decrease in the size of an EEM allows us to reduce the number of measurements while scanning 3D spectra, thus reducing the time needed for an object's authentication. However, the size of an EEM can be decreased more effectively by decreasing the number of wavelength increments, rather than by increasing these increments' values. If the number of different excitation peak wavelengths of all SMs from a set of basis SMs is *m*, and the number of different emission peak wavelengths is *n*, then we can reduce an EEM's size to its minimal value *m x n*. We will call an *m x n* EEM with rows representing different excitation peak wavelengths and columns representing different emission peak wavelengths of SMs from a set of basis SMs a 'basis EEM.' Each EMM from the catalog of tags using basis SMs can be converted into a basis EMM. The basis EEM representing a set of two basis SMs – SM_2 and SM_3 from our example – is shown in Fig. 4.6.

Only two lasers and two filters can be employed for scanning the selected basis SMs, in which case, instead of the 6 x 7 matrix *A* obtained during preliminary experiments and presented in Fig. 4.4, we obtain a basis 2 x 2 EMM, which will further be called matrix *B*.

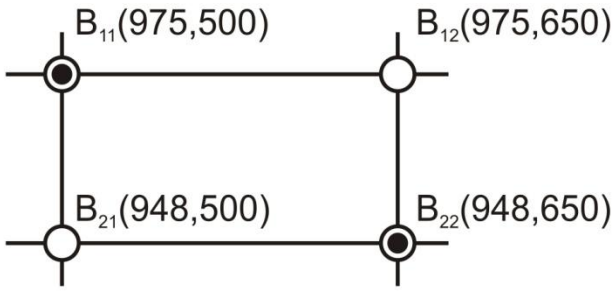

Figure 4.6. A grid representation of matrix *B*.

The reduced size of a basis matrix results in loss of information concerning peaks' shape, which further prevents us from identifying certain peaks by comparing values of neighboring elements of this matrix, because in a basis EEM, elements representing any two peaks may

neighbor each other, or between these two elements there may exist another element of the EEM with a greater value than that of one of these peaks. Although certain peaks cannot be discovered while analyzing a basic EEM there is a simple method allowing us to detect which basis EEM element represents a peak: we can compare relative values of basis EEM elements with the relative values of corresponding elements of the EEM from the catalog. If the relative value of a certain element representing a peak of a catalog matrix is approximately equal to the value of the corresponding element of the basis EEM, then this corresponding element, i.e. the element with the same excitation and emission peak wavelengths, represents a peak. To formalize the process of comparing elements of a basis EEM and the corresponding elements of the EEM from the catalog, we can use fuzzy rule interpolation techniques [111].

A manual comparison of location and configuration of shaded areas on the grid representations of these digitized basis EEMs may result in errors, as these areas can overlap each other. Those errors can be avoided if we use a table representation of basis EEMs. In the table representation of a digitized basis EEM, the cells are shaded if they are located in the same rows and columns as their corresponding EEM elements equaling 1; otherwise, they remain unshaded. A table representation of the digitized basis matrix *B* used instead of its grid representation (See Fig. 4.4) is presented in Fig. 4.7. To conclude, any two 3D spectra represented by digitized basis EEMs are considered to be identical if their table representations coincide.

Emission wavelength, nm		500	650
Excitation wavelength, nm	975		
	948		

Figure 4.7. A table representation of digitized matrix *B*.

4.4. Results and Discussion

In our experiments, we used a private company's proprietary SMs consisting of unknown UC materials in the form of 20-80 μm particles mixed with a solidifying gel. We applied thin layers of the gel on paper sheets assuming that after the gel solidified, all particles would be in one plane because the layer thickness would be in order of 100 μm. Using a microscope, we observed that the mixtures were highly heterogeneous: in certain particle assemblages, the average distance between neighboring particles was about 200 μm, and the average distance between neighboring assemblages almost equaled 1 mm.

While acquiring spectra of the SMs or of their mixtures during preliminary experiments, three measurements have been taken of each data point. The 95% confidence interval as a percentage of mean peak intensity values was 2-5% for strong peak images, and 10-12% for weak peak images. Having analyzed statistically all our measurement results and having rejected questionable data, we transferred all obtained EEMs to the database created in MatLab. The graphical user interface of the MatLab program allows the user to select from the database any two EEMs, to observe and compare any two spectra's three-dimensional and contour. The program identified all peak images and marked them with small white circles on the contour plots (See Fig. 4.8). While analyzing spectra, the user has access to all MatLab functions and tools aimed at solving various data analysis tasks. During our preliminary experiments, 3D

spectra, along with their contour plots and digitized EEMs, of various tags have been acquired and collected into a catalog of SMs. A sample page from this album is presented in Fig. 4.9.

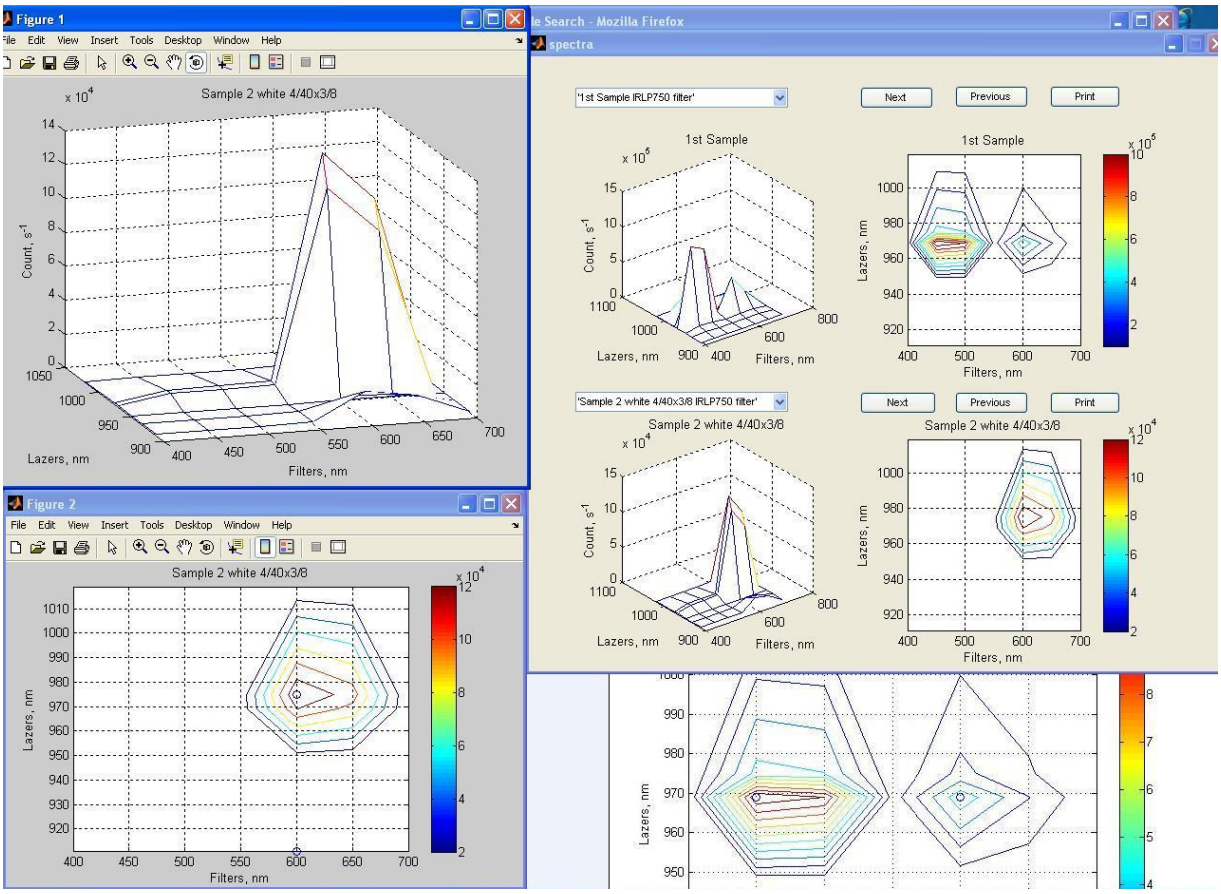

Figure 4.8. Graphical user interface.

During our thorough analysis of the obtained 3D spectra, we have observed some inconsistencies in our measurement results, one of which, the alteration of spectra caused by changing the excitation power density. A similar effect has been mentioned in paper [18]. Yet, this alteration does not compromise the use of UC SMs because it affects measurement results only in case the power density changes by 10% or more. Conversely, we can benefit from this effect and increase a system security by expanding the number of unique IDs due to the excitation of these markers with light of different power densities. We easily eliminated this alteration by setting the optical output power of all LDs at 50 mW each, by adjusting their operating current.

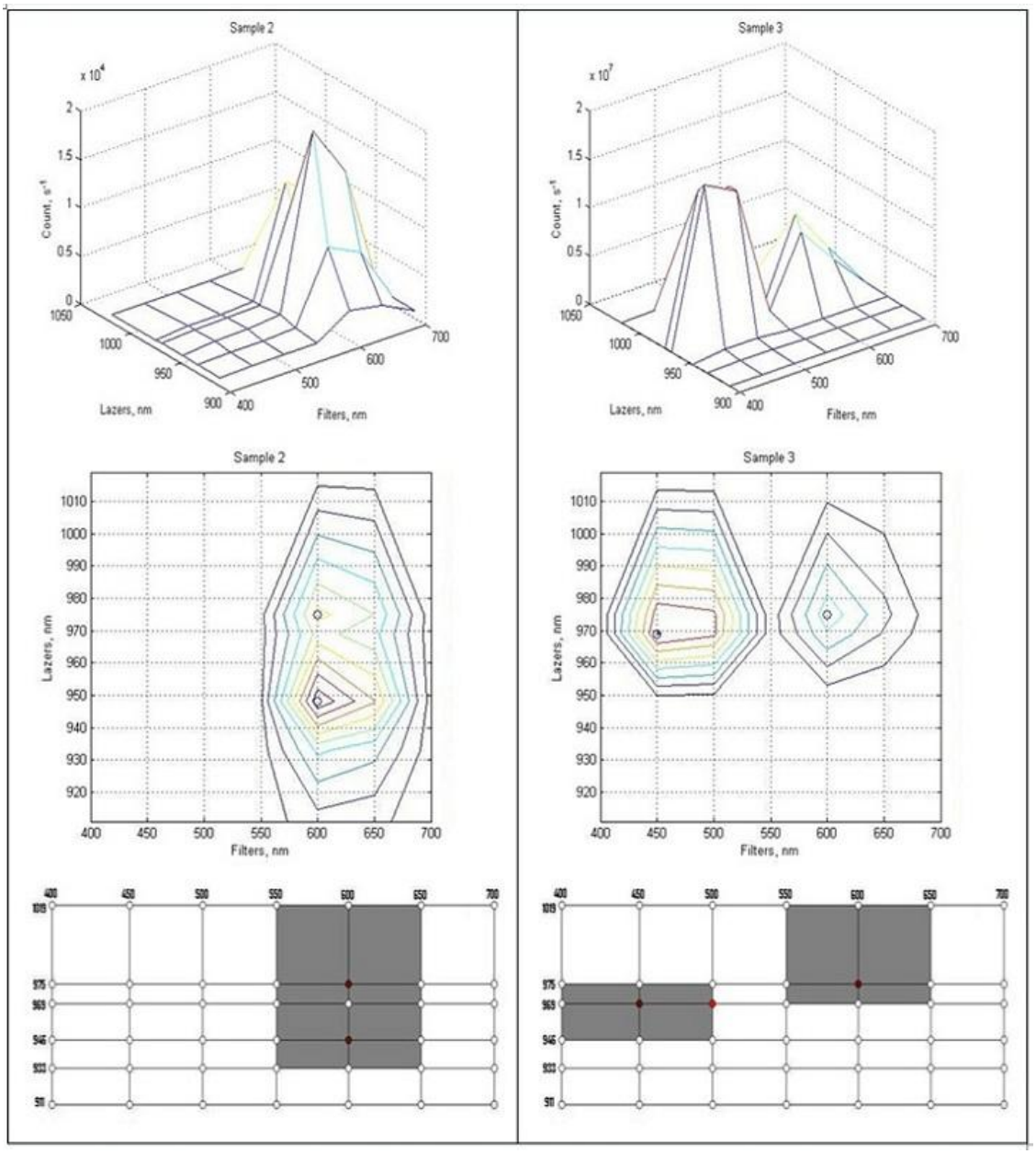

Figure 4.9. Sample page from our SM Catalog.

The use of a heterogeneous mixture of UC SMs employed in a tag and a well-focused laser beam for its excitation could be the reason for another alteration. A certain kind of particles in this tag may be illuminated when the spot of a laser beam is in one position, and not illuminated when it is in another, which may lead to an unexpected spatial alteration of the spectra. In our experiments, we overcame this problem by merely using less-focused laser beams for illuminating heterogeneous mixtures of UC SMs.

After a thorough analysis of the obtained during preliminary experiments 3D spectra, spectra with unexpected alterations have been excluded from the catalog. Three SMs have been selected as basic SMs, providing us with seven tags for further experiments, to examine the feasibility of an object's authentication using these SMs. We compared digitalized EEMs obtained while

scanning these tags and the corresponding EEMs collected in the catalog. All these tags have been identified correctly, thereby validating our assumption.

As we were dealing with unknown proprietary UC SMs, and as our fluorimeter has not been designed to work with this particular set of basis markers, we did not take the excitation and emission peak wavelengths of these SMs and the peaks' FWHMs into consideration, while selecting operational wavelengths of the LDs and central wavelengths of the band-pass filters. Therefore, distances *r* between original peaks and their images could be rather large which will lead to the decrease of the intensity I_{pi} of peak images (See Eq. 4.1). Taking into account the fact that emission wavelength increments of our fluorimeter are constant (S_x=50 nm), and assuming that we are dealing with fluorescent semiconductor nanocrystals characterized by very narrow emission spectra (typically, FWHM=30 nm), and that our detector's accuracy of fluorescence intensity measurements is not lower than 1%, using inequality (3) we come to the conclusion that excitation wavelength increments should be $Sy \leq 44 + BW_L$ or $Sy \leq 45$ nm, for peaks of these nanocrystals to be registered. If the excitation wavelength changes from 975 nm to 1019 nm, our fluorimeter's wavelength increment will equal 44 nm, in which case the intensity of peak images of some narrow peaks (FWHM~30 nm) located between 975 nm and 1019 nm could be around the minimal value I_{min}. As a result, certain peaks can only be identified when the signal-to-noise ratio of measurements is decreased by increasing the counter's integration time up to 10 s. If the values of operational wavelengths of LDs do not substantially differ from the values of excitation peak wavelengths of SMs, the SM's fluorescence emission is sufficiently strong to be viewed even with a "naked eye" and, hence, the SM's peaks can be registered by a PMT operating at a sub-second integration time, or using any conventional photodetector.

The fluorometry of UC materials is a multidimensional technique requiring a substantial amount of time for the acquisition of spectra, depending on the spectral dimension. Researchers need appropriate solutions to obtain 2D and 3D spectra in a single measurement, as well as spectra of higher order, which are particularly important for obtaining comparable real-time spectral information, in an acceptable amount of time. A prototype of a novel fluorimeter developed in our laboratory can lay the foundation for designing devices capable of measuring multidimensional spectra [112]. One of the specific features of the fluorimeter is the ability to individually control a set of LDs used as excitation light sources. This feature opens up opportunities for investigating the unique fluorescence dependency of UC materials on excitation light power density and excitation frequency, which can result in changing the color of emission with the change of these parameters. A modification of this prototype, employing LD excitation techniques, will allow us to obtain an entire 2D excitation spectrum in a single measurement, without substantially affecting the fluorimeter's price. Another modification employing a multianode PMT assembled with filters or dichroic mirrors makes it feasible to obtain a 3D spectrum in a single measurement.

The performance of the prototype has been demonstrated while authenticating an object, using tags composed of UC SMs. Such advantages as high excitation power density provided by the focused laser beams and high-sensitivity detection provided by a PMT enable the user to employ our fluorimeter for work with low-fluorescence-efficiency UC materials present in low concentrations. However, less-focused laser beams are required to avoid authentication errors observed as a spatial alteration of a spectrum in case tags include heterogeneous mixtures of SMs taken in low concentrations.

To decrease the time of spectral acquisition, I proposed a method for authenticating objects, based on the analysis of EEMs representing fluorescent tags where I introduced the notion of a

'basis' SM. Only a basis SM can be employed in tags, to avoid authentication errors when SM spectra have several peaks, and when some peaks of different SMs coincide. I also introduced the notion of 'digitized' and 'basis' EEMs, to improve the speed of information processing, while the EEM representing a tag applied to the protected object is compared with a certain EEM from the catalog.

4.5. Conceptual design of hyper-fluorimeter

An excitation light modulation technique developed by researchers in our university enables detection of fluorescence induced by the radiation of every individual LD when a sample is irradiated by several LDs simultaneously [113]. This technique can be used while modifying our fluorimeter due to the individual control of LDs. Simultaneous illumination and detection of the fluorescence induced by the radiation of all LDs will allow us to obtain an entire excitation spectrum in a single measurement, in which case only a few measurements equaling the number of points sufficient to represent an emission spectrum will be needed for obtaining a 3D spectrum with the modified fluorimeter.

Furthermore, the employing an excitation light modulation technique will allow the modified fluorimeter to operate under the ambient light. For fluorescent materials with long decay times and modulation frequencies of excitation light in the kHz range, not only LDs, but also low-cost LEDs can be used. However, materials with nanosecond decay times require modulation frequencies in the MHz range, which can be achieved only by using LDs. Thus, the modified fluorimeter must employ LDs not only to provide a sufficient power density of excitation light in order to work with UC materials that have very low fluorescence efficiency, but also to provide modulation frequencies of excitation in the MHz range in order to work with materials with nanosecond decay time.

A modification of our fluorimeter involving one of the appropriate laser excitation techniques will not affect the fluorimeter price substantially. Yet another potential modification may involve the use of a multianode PMT assembled with filters or dichroic mirrors. Its implementation may result in such advantages that its price increase will make it well worthwhile. Instead of a slow spinning filter wheel and a relatively inexpensive photon counting head, we will use an 8-channel PMT module with dichroic mirrors, e.g., H11453 [114], to obtain the entire emission spectrum under excitation by one LD or a 3D spectrum under excitation by all employed LDs, in a single measurement. A schematic of the experimental setup for modified fluorimeter's prototype, where a laser controller is used both for adjusting the LD operating current and switching modulation frequencies between LDs, is shown in Fig. 4.10.

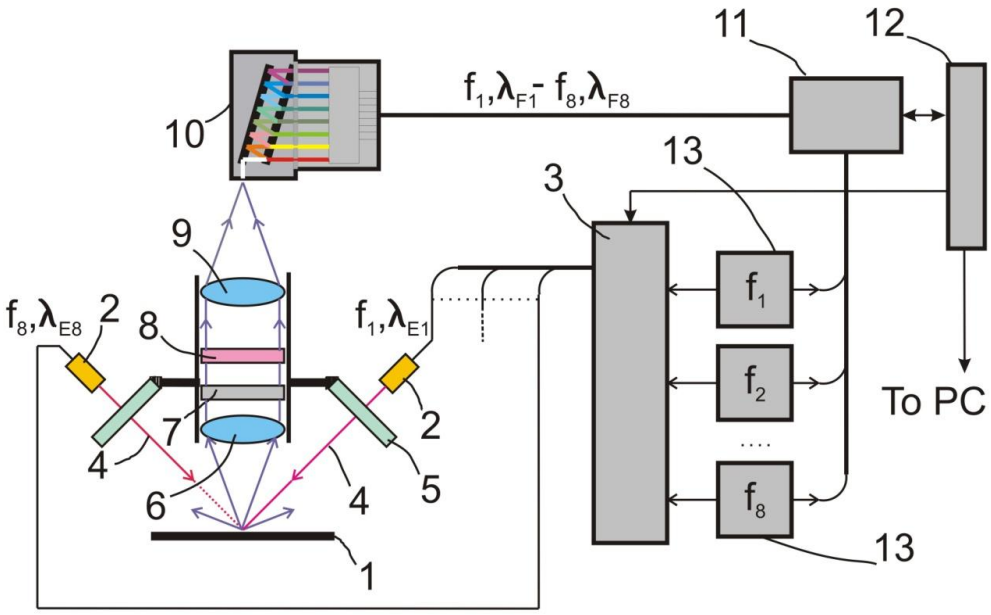

Figure 4.10. Experimental setup schematic: (1) Sample with UC material. (2) Laser diodes. (3) Laser controller. (4) Laser beams. (5) Module with visibly opaque filters. (6) Lens collecting fluorescence light. (7) Neutral density filter. (8) Emission cut-off filter. (9) Focusing lens. (10) Multichannel PMT module. (11) Electronics used for discriminating emission induced by an individual LD. (12) USB Hub. (13) Generators.

The software installed on the computer (PC) sends commands to controller 3 through hub 12, to control data acquisition. Depending on software commands, controller 3 selects one number or several numbers of LDs *i* (*i*=1, 2, …, 8) to illuminate a sample 1 with the excitation light of wavelength λ_{Ei}, sets output optical power for each LD 2,, , and commutates them between generators 13 used to modulate light radiating by LDs at different characteristic frequencies f_i. The information about the current commutation is shared with electronics 11 used for discriminating the emission induced by an individual LD.

To turn an LD off, its optical power is set at zero, and to turn it on, its optical power is set at some predetermined value. For scanning excitation power density, the optical power of an LD is changed from one predetermined value to another. An LD's emission can be modulated by a particular generator or by several generators by connecting them to the LD one after one, to scan excitation frequency. Spectra acquired by scanning the power density of excitation light will allow researchers to facilitate the comparison of fluorescence measurements of UC nanoparticles presented by different laboratories.

A 3D spectrum can be acquired in a single measurement if all LDs are turned on and simultaneously illuminate a sample by modulated beams. In Fig. 4.10, beams of 8 LDs illuminating a sample with wavelength λ_{Ei} (*i*=1, 2, …, 8) are modulated by different characteristic frequencies f_i. The emission, with wavelengths of λ_{Fi}, excited by light with wavelengths of λ_{Ei} is modulated with the same frequencies of f_i. The output signals of every channel of the PMT module 10 corresponds to a particular emission wavelength λ_{Fi} and comprises different fluorescence signals with frequencies f_i corresponding to input signals which represent the exciting light with different wavelengths λ_{Ei} which are modulated by frequencies f_i. Electronics 11 discriminates between these emission signals by using modulation frequencies as

markers and generates 8 x 8 EEM. Due to the ability of our fluorimeter to scan not only excitation and emission wavelengths, but also the power density and modulation frequency of exciting light, thus increasing dimensions of a matrix normally engaged in representing conventional spectra while measuring and processing measurement results, we call such a fluorimeter a "hyper-fluorimeter." Several emission and excitation sample spectra, obtained while scanning excitation light power density, are presented in Fig. 4.11. The sample includes some hypothetical UC fluorescent nanoparticles that have fluorescence properties similar to the properties of the nanoparticles described in paper [18].

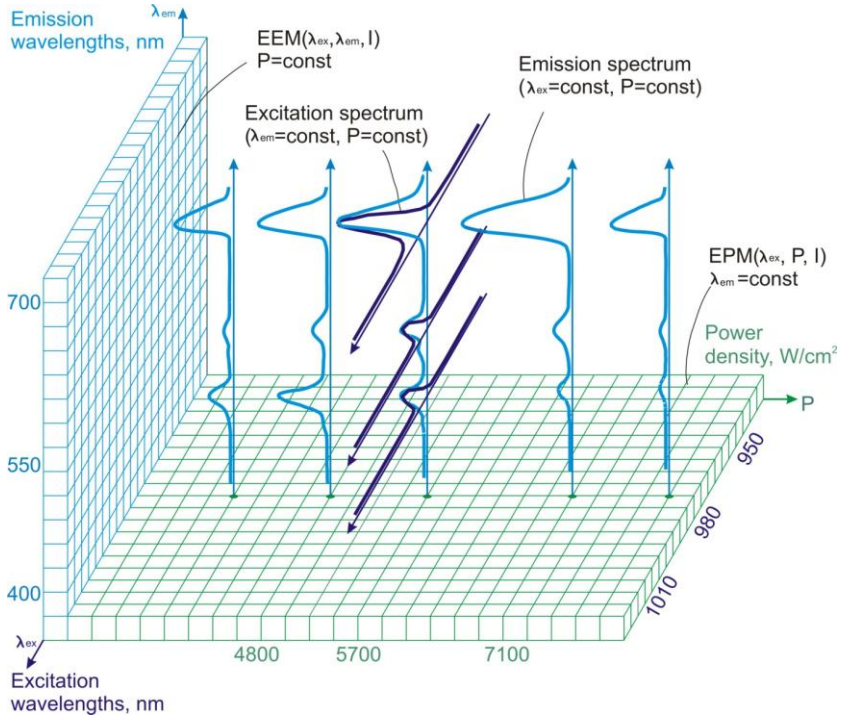

Figure 4.11. Spectra, obtained while scanning excitation light power density, of a sample containing hypothetical UC fluorescent nanoparticles.

Chapter 5

Conclusion

In this dissertation, I presented a prototype of an OOS based on fluorescence quenching, a novel optical design configuration for fluorescence sensors, an analytical model of the OOS, a prototype of a novel fluorimeter, a method based on EEM analysis for authenticating objects marked with fluorescent markers, and a conceptual design of a multidimensional fluorimeter, a "hyper-fluorimeter".

The presented OOS prototype is a simple, low-cost, small-size, robust device which operates without employing any lens or lens system, and can be well-suited for monitoring oxygen concentration in a wide circle of applications. I also developed an analytical model of the OOS, which help me introduce a novel optical design configuration to improve the sensitivity of fluorescence sensors, which can lay the foundation for designing multiple chemical sensors, based on fluorescence quenching. The suggested prototype of a novel fluorimeter can lay the foundation for designing devices capable of measuring multidimensional spectra. One of the specific features of the fluorimeter is the possibility to individually control a set of LDs used as excitation light sources. This feature opens up opportunities for investigating the unique fluorescence dependency of fluorescent materials on excitation light power density and frequency. The fluorimeter performance was demonstrated while authenticating objects marked with fluorescent markers. To avoid authentication errors and decrease processing time, I suggested a method based on EEM analysis. The mentioned fluorimeter prototype provided the basis for our conceptual design of hyper-fluorimeter, which is capable of scanning not only excitation and emission wavelengths, but also excitation light power density and frequency modulation.

Having shown a number of possible directions of how optical sensors can be improved, I hope that this dissertation will be useful to researchers and practitioners who work in the field of optoelectronics.

References

1. Lakowicz, J.R., *Principles of Fluorescence Spectroscopy*. 2010: Springer.

2. Demchenko, A.P., *Introduction to fluorescence sensing*. 2008: Springer Science & Business Media.

3. Huang, B., M. Bates, and X. Zhuang, *Super resolution fluorescence microscopy.* Annual review of biochemistry, 2009. **78**: p. 993.

4. Castrellon-Uribe, J., *Optical Fiber Sensors: An Overview*. 2012: InTech.

5. McDonagh, C., C.S. Burke, and B.D. MacCraith, *Optical chemical sensors.* Chemical reviews, 2008. **108**(2): p. 400-422.

6. Ahuja, D. and D. Parande, *Optical sensors and their applications.* Journal of Scientific Research and Reviews, 2012. **1(5)**: p. 060 - 068.

7. Gauglitz, G., *Direct optical sensors: principles and selected applications.* Analytical and bioanalytical chemistry, 2005. **381**(1): p. 141-155.

8. Wolfbeis, O.S., *Fiber-optic chemical sensors and biosensors.* Analytical Chemistry, 2008. **80**(12): p. 4269-4283.

9. Wang, X.-d. and O.S. Wolfbeis, *Optical methods for sensing and imaging oxygen: materials, spectroscopies and applications.* Chemical Society Reviews, 2014. **43**(10): p. 3666-3761.

10. Yu, F.T.S. and S. Yin, *Fiber optic sensors*. Optical engineering. 2002, New York: Marcel Dekker. x, 494 p.

11. Gouzman, M., et al., *Excitation-emission fluorimeter based on linear interference filters.* Applied optics, 2004. **43**(15): p. 3066-3072.

12. Conmy, R.N., P.G. Coble, and C.E. Del Castillo, *Calibration and performance of a new in situ multi-channel fluorometer for measurement of colored dissolved organic matter in the ocean.* Continental shelf research, 2004. **24**(3): p. 431-442.

13. Muroski, A.R., K.S. Booksh, and M. Myrick, *Single-measurement excitation/emission matrix spectrofluorometer for determination of hydrocarbons in ocean water. 1. Instrumentation and background correction.* Analytical Chemistry, 1996. **68**(20): p. 3534-3538.

14. Xiao, X., et al., *Characterization of coal oil using three-dimensional excitation and emission matrix fluorescence spectroscopy.* Chinese Optics Letters, 2009. **7**(1): p. 85-87.

15. Grigoryan, K. and H. Shilajyan, *Influence of Dimethylsulfoxide on the Fluorescence Behavior of Human Serum Albumin Studied by Excitation–Emission Matrix Fluorescence Spectroscopy Method.* Proceedings of the YSU, Chemistry and Biology Sciences, 2013(1): p. 50-53.

16. Li, B., et al., *Fluorescence Excitation–Emission Matrix (EEM) Spectroscopy for Rapid Identification and Quality Evaluation of Cell Culture Media Components.* Applied spectroscopy, 2011. **65**(11): p. 1240-1249.

17. Gainer, C.F., et al., *Control of green and red upconversion in NaYF4: Yb 3+, Er 3+ nanoparticles by excitation modulation.* Journal of materials chemistry, 2011. **21**(46): p. 18530-18533.

18. Li, A. and Q. Lü, *Power-dependent upconversion luminescence intensity in NaYF4, Yb3+, Er3+ nanoparticles.* EPL (Europhysics Letters), 2011. **96**(1): p. 18001.

19. Lakhtakia, P.K.C.a.A., *The Future of Optoelectronics Technology.* Asian Journal of Physics, 2008. **17**(2): p. 181-183.

20. Valeur, B. and M.N. Berberan-Santos, *Molecular fluorescence: principles and applications*. 2012: John Wiley & Sons.

21. PerkinElmer, I., *An Introduction to Fluorescence Spectroscopy. User Assistance*. 2000: Printed in the United Kingdom.

22. D. Ventazas, N.P., *Peak Searching Algorithms and Applications*, in *The IASTED International Conference on Signal and Image Processing and Applications ~ SIPA 2011*. 2011: Crete, Greece.

23. Bruno, T.J. and P.D. Svoronos, *CRC handbook of fundamental spectroscopic correlation charts*. 2005: CRC Press.

24. van den Engh, G. and C. Farmer, *Photo-bleaching and photon saturation in flow cytometry*. Cytometry, 1992. **13**(7): p. 669-677.

25. Grist, S.M., L. Chrostowski, and K.C. Cheung, *Optical oxygen sensors for applications in microfluidic cell culture.* Sensors, 2010. **10**(10): p. 9286-9316.

26. McDonagh, C., et al., *Characterisation of porosity and sensor response times of sol–gel-derived thin films for oxygen sensor applications.* Journal of Non-Crystalline Solids, 2002. **306**(2): p. 138-148.

27. Colvin, A.E., et al., *A novel solid-state oxygen sensor.* Johns Hopkins APL Technical Digest, 1996. **17**(4): p. 377-385.

28. Committee on new sensor technologies: Materials and Applications, C.o.E.a.T.S., National Research Council, *Expanding the Vision of Sensor Materials*. 1995: National Academy Press.

29. Morris, A.S., *Measurement and instrumentation principles*. 2001: Butterworth-Heinemann.

30. Bochenkov, V. and G. Sergeev, *Sensitivity, selectivity, and stability of gas-sensitive metal-oxide nanostructures.* Metal Oxide Nanostructures and Their Applications, 2010. **3**: p. 31-52.

31. Chu, C.-S., Y.-L. Lo, and T.-W. Sung, *Review on recent developments of fluorescent oxygen and carbon dioxide optical fiber sensors.* Photonic Sensors, 2011. **1**(3): p. 234-250.

32. Ramamoorthy, R., P. Dutta, and S. Akbar, *Oxygen sensors: materials, methods, designs and applications.* Journal of materials science, 2003. **38**(21): p. 4271-4282.

33. Langridge, D.S. *On Line Measurement of Oxygen: Review and New Developments*. in *ISA 55th Analysis Division Symposium*. 2010. New Orleans, LA: International Society of Automation.

34. Cummings, B., et al., *Laser-based absorption spectroscopy as a technique for rapid in-line analysis of respired gas concentrations of O2 and CO2.* Journal of Applied Physiology, 2011. **111**(1): p. 303-307.

35. Lobnik, A., *Absorption-based sensors*. 2006: Springer.

36. Kinder, W., *An interference refractometer for gases and liquids.* Optik, 1966. **24**: p. 323-334.

37. Higgins, C., et al., *Novel hybrid optical sensor materials for in-breath O 2 analysis.* Analyst, 2008. **133**(2): p. 241-247.

38. Austin, E. and J.P. Dakin. *Recent measurements with Ru2+ oxygen sensors using doped sapphire crystals both as a calibration aid and an integral temperature sensor*. in *Environmental and Industrial Sensing*. 2001. International Society for Optics and Photonics.

39. Kellner, K., et al., *Determination of oxygen gradients in engineered tissue using a fluorescent sensor.* Biotechnology and bioengineering, 2002. **80**(1): p. 73-83.

40. Austin, E. and J.P. Dakin. *Optoelectronic systems for addressing Ru oxygen sensors: their design optimization and calibration process*. in *Environmental and Industrial Sensing*. 2002. International Society for Optics and Photonics.

41. Borisov, S.M., R. Seifner, and I. Klimant, *A novel planar optical sensor for simultaneous monitoring of oxygen, carbon dioxide, pH and temperature.* Analytical and bioanalytical chemistry, 2011. **400**(8): p. 2463-2474.

42. Quaranta, M., S.M. Borisov, and I. Klimant, *Indicators for optical oxygen sensors.* Bioanalytical reviews, 2012. **4**(2-4): p. 115-157.

43. Mills, A., *Optical oxygen sensors.* Platinum Metals Review, 1997. **41**: p. 115-126.

44. Panahi, A., *Fiber Optic Oxygen sensor using Fluorescence Quenching for aircraft inerting fuel tank applications.* Photonics in the Transportation Industry: Auto to Aerospace II, 2009. **7314**: p. 9.

45. Chodavarapu, V.P., et al. *CMOS integrated optical sensor using phase detection*. in *Sensors, 2003. Proceedings of IEEE*. 2003. IEEE.

46. Trettnak, W., et al., *Optical oxygen sensor instrumentation based on the detection of luminescence lifetime.* Advances in Space Research, 1998. **22**(10): p. 1465-1474.

47. Chu, C.-S. and S.-W. Chu, *Portable optical oxygen sensor based on time-resolved fluorescence.* Applied optics, 2014. **53**(32): p. 7657-7663.

48. Orellana, G., *Fluorescence-based sensors*, in *Optical Chemical Sensors*. 2006, Springer. p. 99-116.

49. Demas, J.N., B. DeGraff, and P.B. Coleman, *Peer Reviewed: Oxygen Sensors Based on Luminescence Quenching.* Analytical Chemistry, 1999. **71**(23): p. 793A-800A.

50. Morris, K.J., et al., *Luminescence lifetime standards for the nanosecond to microsecond range and oxygen quenching of ruthenium (II) complexes.* Analytical chemistry, 2007. **79**(24): p. 9310-9314.

51. Chuang, H. and M.A. Arnold, *Linear calibration function for optical oxygen sensors based on quenching of ruthenium fluorescence.* Analytica chimica acta, 1998. **368**(1): p. 83-89.

52. Stokes, M. and G. Somero, *An optical oxygen sensor and reaction vessel for high-pressure applications.* Limnology and oceanography, 1999. **44**: p. 189-195.

53. Burke, C.S., et al., *Development of an integrated optic oxygen sensor using a novel, generic platform.* Analyst, 2005. **130**(1): p. 41-45.

54. Chang-Yen, D.A., A. Badardeen, and B.K. Gale, *Spin-assembled nanofilms for gaseous oxygen sensing.* Sensors and Actuators B: Chemical, 2007. **120**(2): p. 426-433.

55. Mills, A., et al., *Luminescent gold compounds in optical oxygen sensors.* Gold Bulletin, 1998. **31**(2): p. 68-70.

56. Chen, R., et al., *A cylindrical-core fiber-optic oxygen sensor based on fluorescence quenching of a platinum complex immobilized in a polymer matrix.* Sensors Journal, IEEE, 2012. **12**(1): p. 71-75.

57. Rigo, M.V., R. Olsson, and P. Geissinger, *Crossed-Optical-Fiber Oxygen Sensors with Intensity and Temperature Referencing for Use in High-Spatial-Resolution Sensor Arrays.* Sensors & Transducers (1726-5479), 2010. **112**(2).

58. Baker, G.L., R.N. Ghosh, and D. Osborn III, *Fiber Optical Micro-detectors for Oxygen Sensing in Power Plants*. 2004, Michigan State University (United States).

59. Chu, C.-S., *Optical oxygen sensing properties of Ru (II) complex and porous silica nanoparticles embedded in solgel matrix.* Applied Optics, 2011. **50**(25): p. E145-E151.

60. Badocco, D., A. Mondin, and P. Pastore, *Signal drift of oxygen optical sensors. Part I: Rationalization of the drift nature and its experimental check with a light intensity detection based sensor.* Sensors and Actuators B: Chemical, 2013. **181**: p. 943-948.

61. Badocco, D., A. Mondin, and P. Pastore, *Signal drift of oxygen optical sensors. Part II:"Smart" drift correction algorithm and its experimental check with a light intensity detection based sensor.* Sensors and Actuators B: Chemical, 2013. **181**: p. 949-954.

62. Basabe-Desmonts, L., D.N. Reinhoudt, and M. Crego-Calama, *Design of fluorescent materials for chemical sensing.* Chemical Society Reviews, 2007. **36**(6): p. 993-1017.

63. Wolfbeis, O.S., *Chemical sensing using indicator dyes.* 1997.

64. Sato, H., K. Tamura, and A. Yamagishi, *Luminescent Oxygen Gas Sensors Based on Nanometer-Thick Hybrid Films of Iridium Complexes and Clay Minerals.* Chemosensors, 2014. **2**(1): p. 41-55.

65. Cavage, W.M., *Measuring Oxygen Concentration in a Fuel Tank Ullage*, in *US Air Force T&E Days 2009*. 2009.

66. Jorge, P., et al., *Optical fiber probes for fluorescence based oxygen sensing.* Sensors and Actuators B: Chemical, 2004. **103**(1): p. 290-299.

67. Lowry, M., et al., *Molecular fluorescence, phosphorescence, and chemiluminescence spectrometry.* Analytical chemistry, 2008. **80**(12): p. 4551-4574.

68. Basu, B.J. and K. Rajam, *Comparison of the oxygen sensor performance of some pyrene derivatives in silicone polymer matrix.* Sensors and Actuators B: Chemical, 2004. **99**(2): p. 459-467.

69. Tang, Y., et al., *Sol-gel-derived sensor materials that yield linear calibration plots, high sensitivity, and long-term stability.* Analytical chemistry, 2003. **75**(10): p. 2407-2413.

70. Pieper, S.B., et al., *Phosphorescence characteristics of ruthenium complex as an optical transducer for biosensors.* Applied Physics Letters, 2008. **92**(8): p. 081915-081915-3.

71. Bacon, J. and J. Demas, *Determination of oxygen concentrations by luminescence quenching of a polymer-immobilized transition-metal complex.* Analytical Chemistry, 1987. **59**(23): p. 2780-2785.

72. McDonagh, C., B. MacCraith, and A. McEvoy, *Tailoring of sol-gel films for optical sensing of oxygen in gas and aqueous phase.* Analytical chemistry, 1998. **70**(1): p. 45-50.

73. Chan, M., et al., *Fiber optic oxygen sensor based on phosphorescence quenching of erythrosin B trapped in silica-gel glasses.* Analytica chimica acta, 2000. **408**(1): p. 33-37.

74. Basu, B.J., *Optical oxygen sensing based on luminescence quenching of platinum porphyrin dyes doped in ormosil coatings.* Sensors and Actuators B: Chemical, 2007. **123**(1): p. 568-577.

75. Baleizao, C., et al., *Dual fluorescence sensor for trace oxygen and temperature with unmatched range and sensitivity.* Analytical chemistry, 2008. **80**(16): p. 6449-6457.

76. Fujiwara, Y. and Y. Amao, *An oxygen sensor based on the fluorescence quenching of pyrene chemisorbed layer onto alumina plates.* Sensors and Actuators B: Chemical, 2003. **89**(1): p. 187-191.

77. Mills, A. and A. Lepre, *Controlling the response characteristics of luminescent porphyrin plastic film sensors for oxygen.* Analytical Chemistry, 1997. **69**(22): p. 4653-4659.

78. Badocco, D., et al., *Dependence of calibration sensitivity of a polysulfone/Ru (II)-Tris (4, 7-diphenyl-1, 10-phenanthroline)-based oxygen optical sensor on its structural parameters.* Analytica chimica acta, 2008. **627**(2): p. 239-246.

79. Wang, X., et al., *Electrospun nanofibrous membranes for highly sensitive optical sensors.* Nano Letters, 2002. **2**(11): p. 1273-1275.

80. Eaton, K. and P. Douglas, *Effect of humidity on the response characteristics of luminescent PtOEP thin film optical oxygen sensors.* Sensors and Actuators B: Chemical, 2002. **82**(1): p. 94-104.

81. Chuang, H. and M.A. Arnold, *Radioluminescent sources for optical chemical sensors.* Pure and applied chemistry, 1999. **71**(5): p. 803-810.

82. Andreas Nolte, L.H., and Michael W. Davidson. *Fundumentals of Illumination Sources for Optical Microscopy*. Education in Microscopy and Digital Imaging 2012; Available from: http://zeiss-campus.magnet.fsu.edu/articles/lightsources/lightsourcefundamentals.html.

83. Craith, B., et al., *LED-based fibre optic oxygen sensor using sol-gel coating.* Electronics Letters, 1994. **30**(11): p. 888-889.

84. Pérez, M.A., O. González, and J.R. Arias, *Optical Fiber Sensors for Chemical and Biological Measurements.* Current Developments in Optical Fiber Technology, 2013.

85. Dybko, A., *Fundamentals of optoelectronics*, in *Optical Chemical Sensors*. 2006, Springer. p. 47-58.

86. Datasheet, *TSL230R−LF, TSL230AR−LF, TSL230BR−LF Programmable light-to-frequency converters*. TAOS. 2006.

87. Datasheet, *SL250, TSL251, TSL252 Light-to-Voltage Optical Sensors*. Texas Instruments. 1995.

88. Datasheet, *TSL235 Light-to-Frequency Converter*. Texas Instruments. 1994.

89. Datasheet, *USB2000* Ocean Optics. Vol. 170-00000-000-05-201102.

90. Gholamzadeh, B. and H. Nabovati, *Fiber optic sensors.* World Academy of Science, Engineering and Technology, 2008. **42**(3): p. 335-340.

91. Udd, E., *An overview of fiber-optic sensors.* review of scientific instruments, 1995. **66**(8): p. 4015-4030.

92. Fidanboylu, K. and H. Efendioglu. *Fiber optic sensors and their applications*. in *Proceedings of 5th International Advanced Technologies Symposium (IATS'09)*. 2009.

93. Méndez, A. and A. Csipkes, *Overview of fiber optic sensors for NDT applications*, in *Nondestructive Testing of Materials and Structures*. 2013, Springer. p. 179-184.

94. Culshaw, B. and A. Kersey, *Fiber-optic sensing: A historical perspective.* Journal of lightwave technology, 2008. **26**(9): p. 1064-1078.

95. Culshaw, B., *Fiber optics in sensing and measurement.* Selected Topics in Quantum Electronics, IEEE Journal of, 2000. **6**(6): p. 1014-1021.

96. Udd, E. and W.B. Spillman Jr, *Fiber optic sensors: an introduction for engineers and scientists*. 2011: John Wiley & Sons.

97. Rivera, L., et al., *Simple dip-probe fluorescence setup sensor for in situ environmental determinations.* Sensors and Actuators B: Chemical, 2009. **137**(2): p. 420-425.

98. Homola, J., *Sensors based on spectroscopy of guided waves*, in *Optical Chemical Sensors*. 2006, Springer. p. 179-192.

99. Products. *RedEye Oxygen Sensing Patches*. 2015; Available from: http://oceanoptics.com/product/redeye-oxygen-sensing-patches/.

100. Datasheet, *LD CN5M Version 1.0*. OSLON SX. 2012.

101. Causon, D. and C. Mingham, *Introductory Finite Difference Methods for PDEs*. 2010: Bookboon.

102. Warner, I.M., G. Patonay, and M.P. Thomas, *Multidimensional luminescence measurements.* Analytical Chemistry, 1985. **57**(3): p. 463A-483A.

103. Designs, T., *Technical note: An introduction to*

fluorescence measurements. **998-0050 Revision A**.

104. Gergely, J.S. and R.K. McLimans, *Laser-enhanced oil correlation system*. 1991, Google Patents.

105. Rodríguez-Cáceres, M.I., et al., *Determination of Mercuric Ion in Water Samples with a LED Exciting and CCD Based Portable Spectrofluorimeter.* American Journal of Analytical Chemistry, 2011. **2**(05): p. 605.

106. Guo, W., et al., *Characterization of dissolved organic matter in urban sewage using excitation emission matrix fluorescence spectroscopy and parallel factor analysis.* Journal of Environmental Sciences, 2010. **22**(11): p. 1728-1734.

107. Hur, J. and J. Cho, *Prediction of BOD, COD, and total nitrogen concentrations in a typical urban river using a fluorescence excitation-emission matrix with PARAFAC and UV absorption indices.* Sensors, 2012. **12**(1): p. 972-986.

108. Riuttamäki, T. and T. Soukka, *Upconverting Phosphor Labels for Bioanalytical Assays*, in *Advances in Chemical Bioanalysis*. 2013, Springer. p. 155-205.

109. Achatz, D.E., R. Ali, and O.S. Wolfbeis, *Luminescent chemical sensing, biosensing, and screening using upconverting nanoparticles*, in *Luminescence applied in sensor science*. 2011, Springer. p. 29-50.

110. Kuzminskiy, V.A., *Optoelectronic Fiber Based Fluorescence Detection Sensor Systems*. 2007, Stony Brook University.

111. Akimoto, M., et al., *Using Fuzzy Reasoning to Support a System of Diagnosis of Skin Disease.* Bioimages, 2009(17): p. 9-18.

112. Borodin Anatoliy, G.M., *Hyper-Fluorimeter, US Patent Application* 2014, State University of New York at Stony Brook USA.

113. Gorfinkel, V. and S. Luryi, *Method and apparatus for identifying fluorophores*. 1998, Google Patents.

114. Hamamatsu, *Linear Array Maltianode PMT Module with Filters H11453/11455/H11457*, in *Catalog Photonic Devices. Electron Tube Devices and Applied Products*. 2013.